Review Article

Maryam Khodadadi, Najmeh Nozhat*, and Hadiseh Nasari

A comprehensive review on hybrid plasmonic waveguides: Structures, applications, challenges, and future perspectives

https://doi.org/10.1515/ntrev-2024-0137
received June 14, 2024; accepted December 26, 2024

Abstract: This article offers an in-depth overview of hybrid plasmonic waveguides (HPWs), a burgeoning area poised to transform optical communication, data processing, biosensing, and nanophotonics. HPWs address the inherent trade-off between propagation loss and confinement by merging dielectric and plasmonic waveguide advantages, enabling nanoscale light confinement beyond the diffraction limit. The review begins with a foundational look at plasmonics, covering the theoretical underpinnings and history of HPWs, followed by a detailed analysis of various HPW structures like dielectric-loaded, metal–dielectric–metal, and metal–insulator–metal waveguides. It examines their unique benefits, fabrication complexities, and limitations, offering a comprehensive perspective on their performance. The article also surveys the significant applications of HPWs and their impact on different fields, and discusses the fabrication, measurement challenges, and material constraints. Highlighting areas needing further exploration, the conclusion points toward future advancements aimed at expanding HPW applications. This review aims to ignite further innovation in the promising area of plasmonics.

Keywords: effective mode area, hybrid plasmonic waveguide, loss-confinement, nanoscale, propagation length

1 Introduction

Nanophotonics, a sunrise industry of the twenty-first century, has opened new pathways for efficient light manipulation at subwavelength scales [1–4]. While surface plasmon polaritons (SPPs) offer unique opportunities for optical field confinement beyond the diffraction limit, enabling the downscaling of photonic-integrated circuits (PICs) [5–7], they also present a notable challenge. The unavoidable trade-off between light confinement and plasmonic loss has become a significant obstacle to nanoscale photonics integration [8,9]. Plasmonic waveguides, fundamental components of many advanced PICs, have been developed in various configurations including metal–insulator–metal (MIM) [10], insulator–metal–insulator (IMI) [11], metal slot [12], dielectric-loaded metal [13,14], channel and nanohole in metal [15,16], and metal ridge and wedge [17,18]. Each configuration has its own set of advantages and disadvantages depending on the specific application [19], and these have been explored in efforts to address the plasmonic loss-confinement challenge. However, despite efforts to mitigate dissipative metallic loss, the light confinement in these plasmonic waveguides remains at levels comparable to conventional dielectric waveguides [20]. This suggests that further research and development are needed to fully exploit the potential of plasmonic waveguides in nanophotonics.

Various strategies have been proposed to overcome obstacles that impede the advancement of nanoscale plasmonic devices for extreme light manipulation, such as the use of gain mediums [21], cryogenic cooling [22], and thin metal films [23]. Nonetheless, these methods are less feasible for mainstream applications in guided-wave plasmonic platforms due to the complexities associated with each. For instance, the integration process of the gain medium with plasmonic devices on PICs is particularly intricate [24], and devices based on the cryogenic cooling technique are costly and difficult to control [25]. Furthermore, the small mode size of long-range SPPs in thin metal films complicates matters further [23].

*** Corresponding author: Najmeh Nozhat,** Department of Electrical Engineering, Shiraz University of Technology, Shiraz, 7155713876, Iran, e-mail: nozhat@sutech.ac.ir
Maryam Khodadadi: Department of Electrical Engineering, Shiraz University of Technology, Shiraz, 7155713876, Iran
Hadiseh Nasari: Photonics Initiative, Advanced Science Research Center, City University of New York, New York, 10031, United States of America

These challenges raise several pertinent questions: Is there a way to control, or even reduce, the high propagation loss of guided-wave plasmonic modes? How can we navigate the inevitable loss-confinement trade-off at the subwavelength scale in PICs? Future research and advancements in the field of plasmonics must aim to address these critical queries.

Hybrid plasmonic waveguides (HPWs) represent a promising approach for achieving the necessary balance between loss and confinement, outperforming both dielectric and plasmonic waveguides in this regard [19,26–28]. Comprising a low-index layer sandwiched between a metal cap and a high-index layer [26–29], HPWs manage to confine the excited transverse magnetic (TM)-guided mode within the low-index layer. This unique configuration enables them to overcome the fundamental constraints posed by conventional guided wave plasmonic platforms and semiconductors [30]. As an alternative to purely plasmonic and dielectric waveguides, HPWs offer several advantages. These include a large mode size within the nanometer-scale low-index layer [30], an ultra-long SPP propagation length [29], and the capacity for effective light manipulation beyond the diffraction limit [31]. Furthermore, considering the rapidly progressing optical technologies, there is an increasing demand for enhancing the capacity of dense PICs. This could be achieved by utilizing small footprint and energy-efficient structures based on HPWs, which offer ultra-low propagation loss and robust optical confinement [32]. In this context, the development of low-cost fabrication technologies is essential for producing HPWs at deep-subwavelength scales, a step that could revolutionize modern hybrid nanophotonic devices [33].

The primary objective of this comprehensive review is to provide an in-depth examination of HPWs, a promising avenue in the domain of nanophotonics and PICs. We aim to illuminate the unique structural characteristics of various types of HPWs, their potential applications, inherent advantages, and existing limitations. A key focus will be on evaluating the existing strategies and advancements made in addressing the loss-confinement trade-off at the nanoscale in PICs. Furthermore, we endeavor to highlight the critical challenges encountered in the experimental phase, ranging from fabrication complexities to issues associated with maintaining structural integrity and managing material limitations. Finally, this review aims to speculate on the future perspectives in this field, anticipating future advancements that could overcome current challenges and expand the potential applications of HPWs. This review intends to stimulate further research and innovation in the domain of HPWs, thereby driving the field of nanophotonics to new heights.

This review is structured as follows: Section 2 commences with an in-depth exploration of the design principles underlying conventional HPWs, including their theoretical foundations and the method of operation. Section 3 elucidates various methodologies used to analyze HPWs, distinguishing the unique strengths and limitations of different configurations of both conventional and modified HPWs. This section addresses the critical challenges in their fabrication and experimental validation, as well as any material constraints.

In Section 4, we delve into the diverse applications of HPWs, highlighting their roles in fields such as optical communication, data processing, biosensing, and nanophotonics. This section also offers a comparative analysis of the effectiveness of HPWs in these applications against other waveguiding solutions. The review culminates in Section 5, where we conclude with a comprehensive summary of the insights gained, identify gaps in current research, and propose future research directions. This section also emphasizes the potential impacts of these future directions on the field of HPWs and broader nanophotonics. Section 6 concludes this article.

2 Principle and background of HPWs

The concept of HPW arises from an attempt to merge the benefits of conventional plasmonic and dielectric waveguides, namely, the extensive propagation length of modes in dielectric waveguides and the intense optical confinement of plasmonic modes. To illustrate the impact of this combination on the confinement of light within the low-index dielectric layer, the normalized power density is depicted in Figure 1. As shown in Figure 1(a), the surface plasmon (SP) mode can be supported at the interface of a metal and a low-index dielectric structure. Concurrently, the guided dielectric wave can propagate through a high-index slab surrounded by a low-index layer. By bringing these two waveguides into proximity, the hybrid TM mode power can be tightly confined within the low-index layer. Moreover, Figure 1(b) reveals that the mode size of the HPW is smaller than that of a plasmonic waveguide with equivalent loss, suggesting the HPW as a promising alternative [19]. However, it should be noted that the metal layer, a critical component of every HPW, inherently incurs loss. The boundaries of this metal layer confine the electromagnetic fields of SPs within the lateral cross section, a characteristic that must be managed in HPW design and application [34].

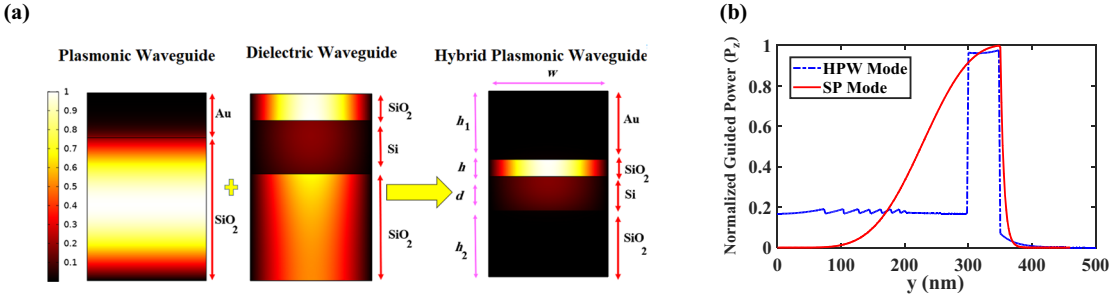

Figure 1: (a) Normalized power density in plasmonic, dielectric, and hybrid plasmonic waveguides. (b) Comparison of guided power density profile of the SP and hybrid modes for the same propagation loss.

The emergence and subsequent application demands for HPWs have necessitated an expansion and tunability of their operational spectral range from infrared (IR) to ultraviolet (UV) [35–37]. Although noble metals like gold (Au) and silver (Ag) are among the most commonly employed plasmonic materials, their inherent properties present considerable challenges when aiming for strong plasmonic resonances in the UV range. Specifically, the plasmon tunability of gold and silver occurs at wavelengths exceeding 550 and 350 nm, respectively [38]. While silver supports SP resonances down to 350 nm, its plasmonic performance deteriorates significantly due to rapid oxidation [1,39]. As a result, alternatives such as aluminum (Al), copper (Cu), and titanium-nitride (TiN) have been identified as more cost-effective and practical options for HPWs [38]. Aluminum, for instance, not only exhibits robust plasmonic resonances from visible to UV frequencies but is also deemed promising due to its compatibility with standard complementary metal-oxide semiconductor (CMOS) techniques [1,40]. Conversely, Cu can offer an SPP propagation length similar to that of noble metals at the wavelength of 1,550 nm. However, the challenge of Cu oxidation during the deposition process restricts its practical use by CMOS foundries [41]. The utility of TiN is largely dependent on the fabrication process and the substrate material used [42]. As such, it fails to meet the requirements for improved light confinement and long-range SPP propagation in HPWs. Consequently, Cu and TiN have not been widely utilized in HPW designs. In an example of the innovative use of these materials, Zhu *et al.* have proposed an athermal hybrid plasmonic ring resonator based on a Cu–TiO_2–Si HPW. This design aimed to increase the quality factor of the pure cell and reduce thermal sensitivity by 50% compared to a Cu–SiO_2–Si device, demonstrating compatibility with CMOS methods [43].

The pathway to CMOS-compatible PICs could be facilitated if the low-index and high-index dielectric layers of HPWs are constructed from materials that are compatible with the CMOS process [30,38,40]. Silicon emerges as an advantageous choice for this purpose; however, a considerable portion of HPW demonstrations rely on bulk crystalline silicon or polysilicon-on-insulator [44–49]. This reliance complicates the integration of silicon-on-insulator (SOI)-based HPWs into preexisting CMOS circuitry [40]. To circumvent this issue, the utilization of amorphous silicon (a-Si) is suggested [50].

The investigation of the hybrid TM mode supported by HPWs can be undertaken *via* different approaches. These include orthogonal or nonorthogonal coupled mode theory (CMT), as well as the exact solution of Maxwell's equations obtained by discerning the dispersion relation [19,51]. While conventional CMT can provide an approximate physical understanding, it may not yield valid results due to the strong coupling between the guided modes of plasmonic and dielectric waveguides [51]. The nonorthogonal CMT approach, conversely, is inapplicable due to the strong coupling within the high-index layer of the dielectric waveguide [52,53]. As such, the hybrid guided mode cannot be precisely analyzed using CMT. Therefore, a reliable method to glean the characteristics of guided modes in HPWs is through the dispersion relation, which can be computed by expanding Maxwell's equations for each layer of the conventional HPW, as depicted schematically in Figure 2(a), and applying the appropriate boundary conditions. This approach yields the propagation constant of the HPW, providing accurate insights into the confinement and propagation of the TM mode within the low-index dielectric layer [19,54].

By considering the complex propagation constant $\left(\gamma = \frac{2\pi n_{\text{eff}}}{\lambda_0} = \frac{2\pi(n'_{\text{eff}} + jn''_{\text{eff}})}{\lambda_0}\right)$ along the z direction, the magnetic fields of each layer can be written as follows [19,26,51]:

$$\boldsymbol{H}_{L,H}(y,z,t) = \hat{x}[H_{L,H}\cos(k_{L,H}y) + H'_{L,H}\sin(k_{L,H}y)]e^{-\gamma z+j\omega t}, \quad (1)$$

$$\boldsymbol{H}_m(y,z,t) = \hat{x}H_m e^{-k_m(y-(h_L+h_H))}e^{-\gamma z+j\omega t}, \quad (2)$$

$$\boldsymbol{H}_s(y,z,t) = \hat{x}H_s e^{k_s y}e^{-\gamma z+j\omega t}, \quad (3)$$

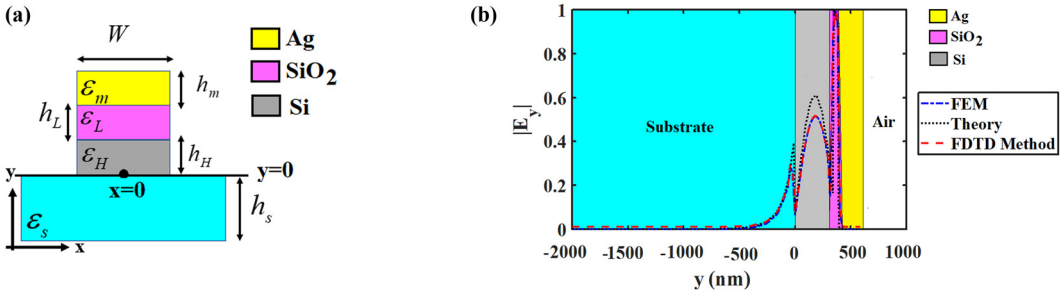

Figure 2: (a) Schematic view of the conventional HPW. (b) Normalized y-component of electric field ($|E_y|$) distribution at the cross section of the conventional HPW along the y direction when x = 0. h_s = 2,000 nm, h_m = 200 nm, h_L = 45 nm, h_H = 340 nm, W = 340 nm, ε_m = –129.17 + j3.284, ε_L = 2.08, ε_H = 11.94 at 1,550 nm.

where $k_{L,H} = \sqrt{\varepsilon_{L,H}k_0^2 - \gamma^2}$ is the transverse wave number in the low-index and high-index layers and $k_{m,s} = \sqrt{\gamma^2 - \varepsilon_{m,s}k_0^2}$ is the attenuation coefficient in the metal and substrate. n_{eff} is the effective refractive index, k_0 is the free space wave number, and λ_0 is the free space wavelength. Also, H and H' are constant amplitudes that are obtained from boundary conditions.

By applying boundary conditions and some straightforward algebra, the dispersion relation of the conventional HPW can be obtained as follows [26]:

$$\frac{k_L}{\varepsilon_L}a_{11} + \frac{k_m}{\varepsilon_m}a_{22} - a_{21} + \frac{k_m k_L}{\varepsilon_m \varepsilon_L}a_{12} = 0, \tag{4}$$

where

$$\begin{pmatrix} a_{11} & a_{12} \\ a_{21} & a_{22} \end{pmatrix} = \begin{pmatrix} \cos(k_L h_L) & -\frac{\varepsilon_L}{k_L}\sin(k_L h_L) \\ \frac{k_L}{\varepsilon_L}\sin(k_L h_L) & \cos(k_L h_L) \end{pmatrix} \times \begin{pmatrix} \cos(k_H h_H) & -\frac{\varepsilon_H}{k_H}\sin(k_H h_H) \\ \frac{k_H}{\varepsilon_H}\sin(k_H h_H) & \cos(k_H h_H) \end{pmatrix}. \tag{5}$$

Figure 2(b) shows a comparison between the computed results using two different numerical approaches, *i.e.*, finite element method (FEM) and finite-difference time-domain (FDTD) method and also theoretical technique based on solving equation (4) utilizing the genetic algorithm.

In the design of HPWs using FEM, several considerations are essential for achieving accurate and efficient simulations. FEM is particularly advantageous for handling complex geometries and intricate material interfaces, which are characteristic of HPW structures. Meshing and geometry discretization are critical components, as FEM versatility enables a high degree of precision in defining mesh elements that adapt to complex interfaces. For HPWs, meshing needs to be extremely fine at metal–dielectric boundaries where field intensities and gradients reach their highest values. Specifically, the mesh elements should be smallest in areas where the plasmonic field is expected to be tightly confined, such as at metal corners or in thin dielectric layers sandwiched between metal and waveguiding layers. This fine meshing ensures that field interactions within these regions are accurately captured, albeit at the cost of increased computational resources. Another significant advantage of FEM is its capability to precisely define material properties and implement complex boundary conditions, which becomes particularly important in nonlinear HPW designs. In these cases, FEM can be configured to include nonlinear material parameters, such as Kerr-type nonlinearities, if relevant to the design. Incorporating these nonlinearities within the FEM framework introduces additional computational complexity, often resulting in greater memory usage and increased computation time. However, this trade-off is often necessary to capture the nonlinear interactions accurately within the waveguide. Finally, managing boundary conditions in FEM simulations for HPWs is crucial, as these structures are typically open, and unwanted reflections at the simulation boundary must be minimized. To achieve this, perfectly matched layers (PMLs) or scattering boundary conditions are generally applied to prevent artificial reflections. Due to FEM matrix-solving nature, its precision in frequency-domain analysis is often superior to other methods. However, the computational expense can be significant, particularly for three-dimensional designs, as matrix-solving approach demands substantial memory and processing power, especially when accounting for fine meshing and boundary condition complexity.

In parallel, in designing HPWs with the FDTD method, certain critical considerations must be addressed to ensure accurate simulation results. FDTD operates on a time-stepping basis, requiring a uniform or near-uniform grid across the simulation space. While this setup is straightforward, it presents challenges for complex HPW structures, as the

uniform grid lacks the adaptability needed to capture fine structural details accurately. To maintain high precision, especially at metal–dielectric interfaces where plasmonic modes are concentrated, an extremely fine grid is necessary. However, this refinement leads to tighter restrictions on the simulation time step, as dictated by the Courant stability condition, which in turn increases the overall computational cost. Thus, while higher grid resolution enhances accuracy, it also demands significantly more computational resources. FDTD is particularly advantageous when simulating time-dependent or nonlinear dynamics, as its time-domain approach makes it well suited for capturing transient phenomena. This is beneficial for HPW designs that involve time-dependent effects, such as Kerr-type nonlinearities or saturable absorbers, as FDTD can directly incorporate these nonlinear material properties. Furthermore, the time-stepping nature of FDTD inherently accounts for dispersion, allowing for more realistic modeling of frequency-dependent behavior within the waveguide structure. To prevent artificial reflections at the boundaries of the simulation domain, absorbing boundaries, typically in the form of PMLs, are essential in FDTD simulations. Despite this similarity with FEM, the FDTD method often requires more computational resources, particularly for simulations involving large-scale or high-resolution structures, as the uniform grid and time-stepping approach are computationally intensive, especially in three-dimensional models. This computational load underscores the need for careful balancing between grid resolution, simulation accuracy, and available computational capacity in FDTD modeling of HPWs.

Moreover, in comparing FEM and FDTD methods for HPW designs, it is essential to examine their relative accuracy and computational complexity to determine the most suitable approach for specific scenarios. Regarding accuracy, FEM often achieves higher precision in frequency-domain analysis of HPW structures due to its ability to adapt the mesh to capture small structural features and areas with intense field gradients. This adaptability makes FEM particularly effective for HPW designs where subwavelength features and sharp material interfaces play a significant role. Conversely, FDTD is most accurate for time-domain analyses, making it a valuable tool for modeling transient and broadband responses. However, because FDTD relies on a uniform or near-uniform grid, it can be less precise for subwavelength details unless the grid is exceptionally fine, which can increase computational demands. From a computational complexity perspective, FEM can be demanding due to the large matrix systems that must be solved, especially in three-dimensional simulations. This approach typically requires substantial memory allocation and computational power but can offer faster convergence in some cases, depending on the complexity of the HPW structure and mesh adaptation. FDTD, on the other hand, is conceptually straightforward but often requires more memory and processing power for intricate or large-scale designs. The need for a uniform grid and high temporal resolution in FDTD, particularly in cases involving nonlinear or dispersive materials, further contributes to its computational load. Thus, while both methods offer distinct advantages, FEM and FDTD differ significantly in how they balance accuracy and computational demands, making the choice of method highly dependent on the specific requirements and constraints of HPW design.

2.1 Geometrical parameters

Multiple studies have delved into the exploration of the influence of structural parameters on the characteristics and performance of HPWs [19,26,27,44–49,51,55–58]. This discussion consolidates and reviews the general observations and findings. A strong coupling occurs between the SP mode of the plasmonic waveguide and the guided mode of the dielectric waveguide, predominantly near the low-index dielectric layer. The resultant coupled modes display incomplete symmetry, leading to the manifestation of quasi-even and quasi-odd TM modes [19,51]. The thicknesses of both low-index and high-index layers emerge as pivotal geometric parameters in the formation of both quasi-even and quasi-odd TM modes. Examination of the variations in the effective mode index of HPW upon altering these thicknesses for the excitation of a different hybrid mode reveals that [19,26,27,51] the modes supported by the HPW are significantly influenced by the thickness of the high-index layer (h_H), leading to diverse scenarios. An exceedingly thick high-index layer results in a conductor-gap-dielectric waveguide hosting an unusual mode [59]. Further, when the thickness exceeds 340 nm, higher order modes such as TM_2 surface, which, to the best of our knowledge, have not been explored for the control and guidance of confined light through HPW [19,26]. Under the condition of h_H = 340 nm, the effective mode index of the dielectric waveguide surpasses that of the plasmonic waveguide, thereby not only supporting the hybrid mode in the HPW but also separately propagating the dielectric waveguide mode as TM_0 mode [60–62].

Moreover, the thickness of the low-index layer (h_L) has a profound effect on the emergence of quasi-even and quasi-odd modes. While the quasi-even mode is confined to any low-index layer thickness, the quasi-odd mode cannot be confined in thin layers. A decrease in h_L results

in the propagation of a hybrid TM mode rather than pure plasmonic and dielectric modes. The effective index of the quasi-even (odd) mode is higher (lower) than the effective indices of modes in plasmonic and dielectric waveguides [19,26,63]. It is important to note that to generate a hybrid TM plasmonic mode, only modes from dielectric waveguide and SP mode with analogous effective refractive indices can engage in coupling [19,64,65]. In addition to the fundamental hybrid TM mode, the first-order hybrid mode emerges from the amalgamation of the SP mode and the TM_1 mode of the dielectric waveguide. A prerequisite for the propagation of this mode is that the thickness of the low-index layer should fall below the cut-off thickness of the TM_1 mode of the dielectric waveguide [19,26]. This first-order hybrid TM mode can be supported by plasmonic nanowaveguides fashioned as a slot in a metallic layer [66].

3 Superiorities and restrictions of HPW configurations

Since the initial proposal of the first HPW by Alam *et al.* in 2007, numerous multilayer HPWs have been numerically and experimentally explored to achieve long- and ultra-long-range modes with substantial confinement [19,26,27,43–49,51,55–58,67–104]. For a comprehensive understanding, it is helpful to classify HPWs based on the shape of their cross section, such as rectangular, circular, and so forth, to elucidate the unique strengths and limitations of various proposed HPWs. Although these suggested HPWs offer substantial confinement and a reasonable loss reduction compared to plasmonic waveguides, the complex fabrication processes for some of these HPW structures, such as symmetric and circular designs, pose significant challenges. These challenges can result in the hindrance of their low-loss nature and cause refraining modal cut-off [56,67,68]. Therefore, compared to dielectric waveguides, which boast a straightforward fabrication process, the complexity of HPW fabrication procedures should be acknowledged as one of their significant limitations [69].

In addition, as depicted in Figure 3, HPWs can support and confine both transverse electric (TE) and TM modes within the high-index and low-index layers, respectively. This is a noteworthy feature considering that plasmonic waveguides only support TM modes [70,71]. Such versatility earmarks HPWs as a promising candidate for implementing photonic devices that operate in a controllable polarization state [70–74].

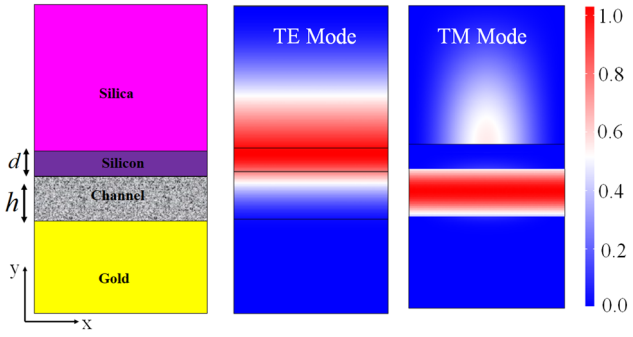

Figure 3: Schematic view of HPW with normalized guided power densities of TE and TM polarizations.

3.1 Rectangular HPWs (RHPWs)

Given that the fabrication process for HPWs with a rectangular cross section is simpler than that for circular and modified ones, a wide variety of structures have been proposed and examined for diverse applications [30,45–49,75–80]. For instance, materials such as active, passive, and ferroelectric substances [93,94,102], vanadium oxide [103], vanadate [104], and polymers [95–99] have been utilized to capitalize on the multifaceted nature of HPWs. In addition, HPWs have been designed using a metal strip [46], composite structure [50], and semi-MIM design [100,101], in either symmetric or asymmetric configuration [81–92].

To investigate the limitation and advantage of HPWs, the propagation length ($L_p = \lambda_0/4\pi n''_{\text{eff}}$) and effective mode area

$$\left(A_m = \frac{\left(\iint W(r)\mathrm{d}A\right)^2}{\iint W(r)^2\mathrm{d}A},\ W(r) = 0.5\,\mathrm{Re}\left\{\frac{\mathrm{d}[\omega\varepsilon(r)]}{\mathrm{d}\omega}\right\}|E(r)|^2 + 0.5\mu_0\,|H(r)|^2\right)$$

should be studied. L_p is defined as the distance that the amplitude of the field attenuates to $1/e$ of its maximum value and A_m is the ratio of the total mode energy flux and the peak energy flux density, where $E(r)$ and $H(r)$ are the electric and magnetic fields, $\varepsilon(r)$ is the electric permittivity, and μ_0 is the vacuum magnetic permeability [30].

Figure 4 presents various RHPWs and their corresponding electric field distributions, confined to the low-index layer. These have been explored numerically and theoretically in the literature. The first proposed HPW (Figure 4(a)) consists of 100 × 160 nm² dielectric layers on top of a metallic substrate [68]. Dai and He have introduced a HPW comprising an SOI rib with a metal cap (Figure 4(b)), thus paving a novel path to HPW design that is compatible with silicon photonics and CMOS technology [45]. Minimizing the rib thickness to zero yields a shallow etching depth, reducing the complexity of the fabrication process.

One of the major trends in choosing the material for dielectric layers and their dimensions is to enhance the

coupling efficiency between the HPW and other photonic and dielectric components. To this end, replacing SiO_2 with 100 nm thick alumina in Figure 4(b) resulted in a coupling efficiency of 70% between the HPW and tapered plasmonic waveguide at the wavelength of 1,550 nm [47].

Hydrogen silsesquioxane (HSQ), a structure akin to silica, adheres well to silicon wafers and has a low refractive index of 1.4. Its attributes such as high uniformity, high etching resistance, high resolution, and minimal line edge roughness make it a suitable candidate for the low-index layer of HPWs [105–107]. Utilizing this, an HPW crossing with an insertion loss and cross talk of 4.9 and −22 dB, respectively, at 1,550 nm has been proposed (Figure 4(c)) [49]. The fabricated HSQ-based HPW enhances the performance of direct waveguide crossings, significantly reducing the fabrication complexity in dense circuits when implemented as a hybrid cross-grid array.

Figure 4(d) demonstrates the concept of using a thin silicon strip positioned in the silica gap between the silver substrate and silicon ridge [30]. Compared to the aforementioned conventional HPWs [45,49,68], this configuration has reported nearly 50 and 60% improvement in the confined power and effective mode area, respectively, with a maximum long-range propagation length of 65 μm. Unlike standard HPWs, strip-loaded HPWs can confine light within two nanoscale regions, as demonstrated in the electric field distribution in Figure 4(d).

However, it is essential to note that these structures face challenges related to the lateral misalignment of the silicon strip and small gap (less than 5 nm) between the strip and metal substrate. These factors affect the mode properties and can cause rapid nonradiative quenching [30,108]. As such, managing the misalignment and the gap between the strip and metal layer represents a significant challenge in strip-loaded HPWs [30]. For instance, a 50 nm misalignment has been found to result in asymmetric modal distribution and changes in the propagation length and effective mode area of 1.5 and 2.5%, respectively [30]. Sharma and Kumar have achieved an increase in the propagation length of strip-loaded HPWs from 65 to 142 μm by introducing a hollow HPW with a smaller effective mode area and low propagation loss of 0.0685 μm^2 and 0.03 dB/μm, respectively [48].

One approach to enhance the propagation length of plasmonic waveguides involves the use of a gain medium [21], a strategy first introduced by Dai *et al.* for both low-

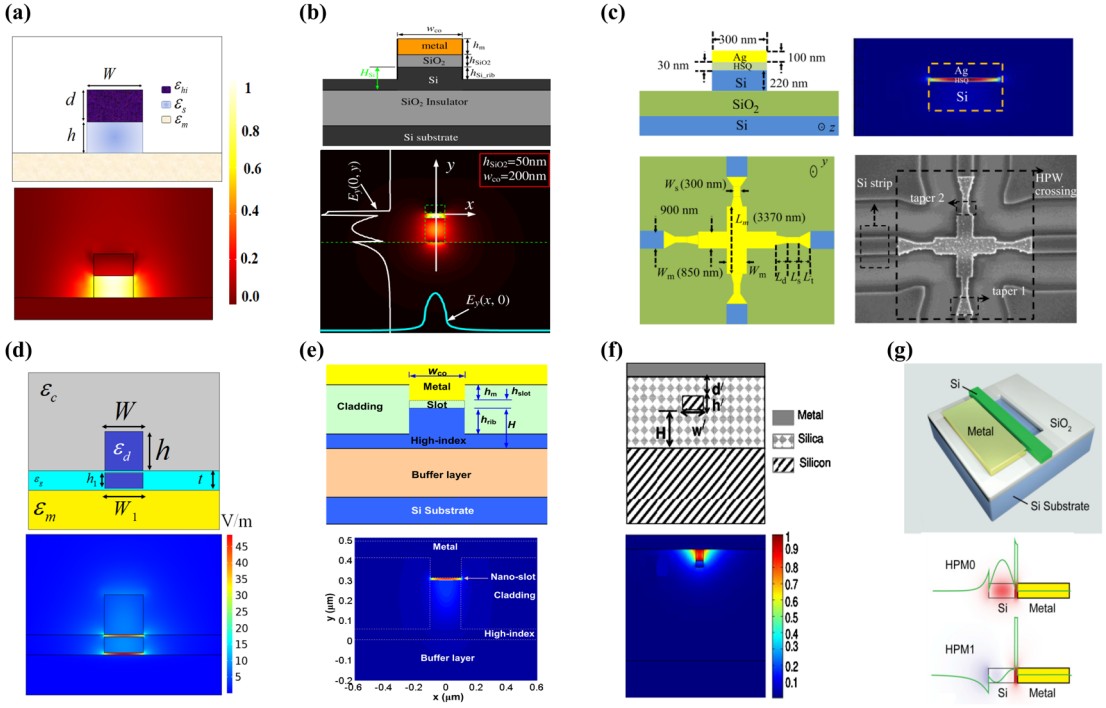

Figure 4: Different topologies of conventional HPWs and their electric field distributions at the cross section. (a) First schematic view of the proposed HPW, (b) HPW compatible with CMOS technique (reproduced with permission from the study by Dai and He [45], © Optica Publishing Group), (c) HSQ HPW-based crossing (reproduced with permission from the study by Li *et al.* [49], © Elsevier), (d) low-index strip loaded HPW, (e) gain medium with inverted metal slab HPW (reproduced with permission from the study by Dai *et al*. [79], © Optica Publishing Group), (f) metal–dielectric HPW (adapted with permission from the study by Alam *et al*. [80], © Optica Publishing Group), and (g) vertical HPW (VHPW) (reproduced with permission from the study by Li *et al*. [76] © Optica Publishing Group).

index and high-index layers [79]. Figure 4(e) exemplifies the concept of using an inverted metal rib to improve the adhesion between the metal and low-index layer. Silicon nanocrystal and polymers with quantum dots can serve as the low-index medium, while silicon with Erbium (Er) doping and a III-V semiconductor are suitable for the high-index layer [79]. Various thin-film deposition techniques and spin-coating technologies for silicon nanocrystal and Er doping can be employed to integrate these gain media [109–112]. Dai *et al.* have assumed moderate gains of 35.2, 176, and 352 dB cm^{-1} for both of these gain media. Their findings demonstrate that as the height of low-index slot decreases, the intrinsic loss increases, a situation that can be mitigated by incorporating more gain. Furthermore, by augmenting the gain, the loss of the proposed HPW with the inverted metal rib decreases significantly compared to the conventional media [79].

A rib metal cap structure similar to that depicted in Figure 4(e) has been fabricated and assessed by Wang *et al.*, with a reported fiber-to-fiber loss of 0.22 dB μm^{-1} [77]. The structure presented in Figure 4(f) can simplify the fabrication process by eliminating the need for a deposited silicon layer atop the silica, thus removing the subsequent requirement for etching these two layers [80].

All of the aforementioned HPWs are capable of confining the excited TM mode into the low-index layer. Notably, Li *et al.* have conducted the first experimental demonstration of a vertical metal dielectric HPW that can predominantly confine TE optical modes into the high-index Si layer [76]. As shown in Figure 4(g), the VHPW comprises a metal layer, which runs parallel to a strip Si layer on a standard SOI wafer. The introduction of the vertical configuration of HPW has led to a decrease in optical loss compared to the structures proposed by Sorger *et al.* [113] and Oulton *et al.* [114]. This is due to an enhancement in the optical mode confinement, which results in an improvement of the optical force by an order of magnitude or more [115,116].

One approach to show the advantage of VHPWs in comparison with other waveguides is investigation of total optical force $\left(F = \frac{\int_0^L |\, p(x)\,|\, \mathrm{d}x}{P(0)} = p_n \int_0^L e^{-\alpha x}\mathrm{d}x = \frac{p_n}{\alpha}(1 - e^{-\alpha L})\right)$ instead of propagation loss and propagation length, where L, $p(x) = P(0)e^{-\alpha x}$, p_n, and $\alpha = 4\pi n''_{\mathrm{eff}}/\lambda_0$ are waveguide length, optical power as a function of position x, normalized local optical force, and decay constant, respectively [76].

Figure 5 illustrates the superiority of VHPW by comparing the optical force of VHPW proposed by Li *et al.* with other waveguide configurations presented in the literature. Due to the field enhancement effect, the achieved

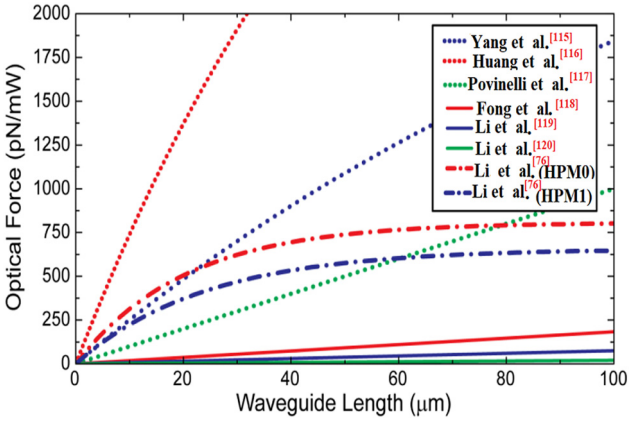

Figure 5: Comparison of total optical force dependence on the waveguide length in different dielectric, plasmonic, and HPW configurations. Solid lines represent experimental work, while the other line styles represent theoretical calculation. Adapted with permission from the study by Li *et al.* [76], © Optica Publishing Group.

optical force of the metal–dielectric VHPW is stronger than that of dielectric systems [117–120] over a short distance. According to this figure, HPWs can generate high optical forces over short distances and thus potentially contribute to the miniaturization of the footprint of PICs. However, for longer distances, the loss of HPWs may become too substantial to compete with dielectric waveguides in generating high optical forces [76].

Another strategy to decrease optical loss involves the use of an HPW configuration constructed from metal with a dielectric coating [95–99]. As demonstrated in Figure 6(a), the introduction of a silicon nitride (SiN_x) cladding layer not only dramatically reduces the effective mode area from 0.18 to 0.029 μm^2 but also provides superior control over the optical properties of HPW, due to the impact of high density of dangling bonds on the Si layer [96]. Compared to the HPW proposed by Song *et al.* [98], which has high propagation loss due to the use of an alumina dielectric spacer, the loss of SiN_x-covered HPW is significantly lower. However, the use of dielectric-loaded HPWs can present some experimental challenges, especially in protecting the device from ambient native oxidation, which occurs when the Si layer is exposed to air [121,122]. The thickness of the oxide layer and the growth of native oxide on the Si layer can vary depending on different environmental conditions, which in turn leads to unpredictable optical performance [123,124].

The issue of Si native oxidation can be addressed by introducing metal and dielectric cladding layers [96–99]. As shown in Figure 6(a), the best optical mode confinement occurs at h = 50 nm, with a propagation length of approximately 60 μm. Therefore, to strike a balance between the

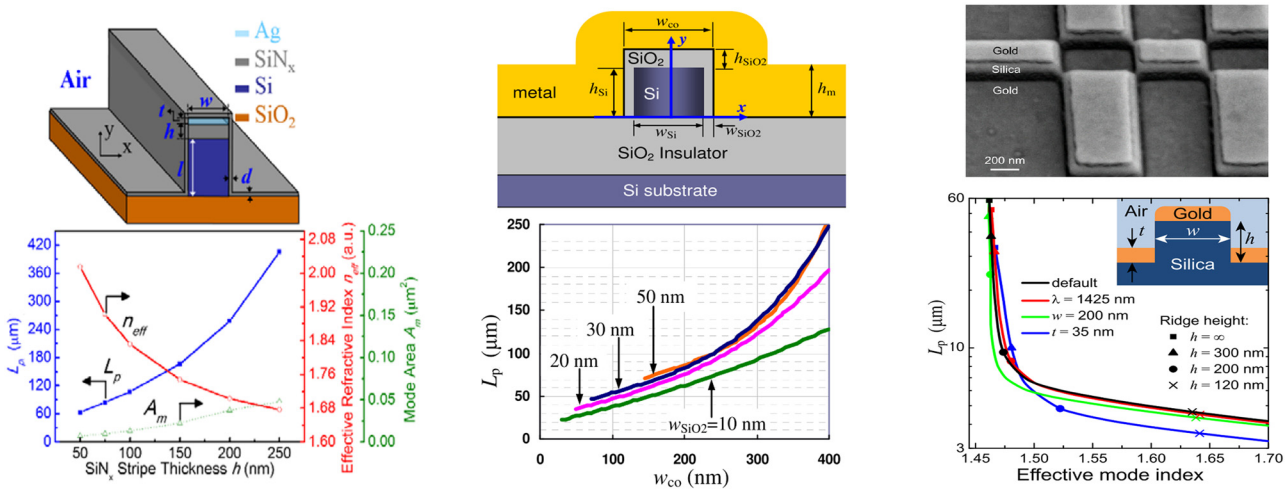

Figure 6: Various types of dielectric and metal cladding layers of HPWs with their related propagation length diagram. (a) Dielectric covering HPW with propagation length *versus* the variations of SiN_x strip thickness. Adapted with permission from the study by Hsieh *et al*. [96], © Electromagnetics Academy. (b) Metal covering HPW with double low-index slots and its propagation length *versus* the variations of waveguide width. Adapted with permission from the study by Dai and He [99], © Optica Publishing Group. (c) Gold coating of ridges etched into a silica substrate with its propagation length *versus* the variations of effective mode index. Adapted with permission from the study by Zenin *et al*. [97] © Optica Publishing Group.

propagation length and mode confinement, an optimal thickness for the SiN_x strip would be h = 150 nm [96]. The thickness of the cladding layer (d) also significantly affects the trade-off between the effective mode area and propagation length. By setting d to 10 nm, a propagation length of 350 μm has been achieved.

Moreover, the introduction of a metal cladding layer with double low-index slots, as shown in Figure 6(b), significantly reduces the effective mode area to 0.007 μm^2 for w_{SiO_2} = 10 nm and w_{co} = 50 nm. However, the high intrinsic loss of the metal cladding layer results in a propagation length of less than 50 μm [99]. Compared to the dielectric cladding layer (Figure 6(a)), this metal coating configuration offers an ultra-small mode area, but the propagation length is more than seven times shorter [96,99]. Zenin *et al.* have proposed and fabricated an HPW that consists of gold-coated ridges etched into a silica substrate, reporting a moderate propagation length of 10 μm [97]. While the area covered by gold in the structure shown in Figure 6(c) has been reduced compared to Figure 6(b), the propagation is not long range.

As depicted in Figure 7, super-mode HPWs, consisting of both symmetric and asymmetric hybrid insulator–metal–insulator (HIMI) waveguides and hybrid metal–insulator–metal (HMIM) waveguides in horizontal and vertical configurations, are capable of confining two distinct even and odd modes in two low-index regions [85,86,89]. In addition, these super-mode HPWs can support both long- and short-range hybrid modes due to differences in their propagation lengths. Analyses of the advantages and limitations of symmetric and asymmetric HPWs reveal that the fundamental mode of the asymmetric HPW, known as TM_0, has a shorter propagation length compared to the long-range TM_1 mode of the symmetric HPW [86,89].

In addition, a crucial aspect in designing symmetric or asymmetric HPWs is to select a metal thickness that is less

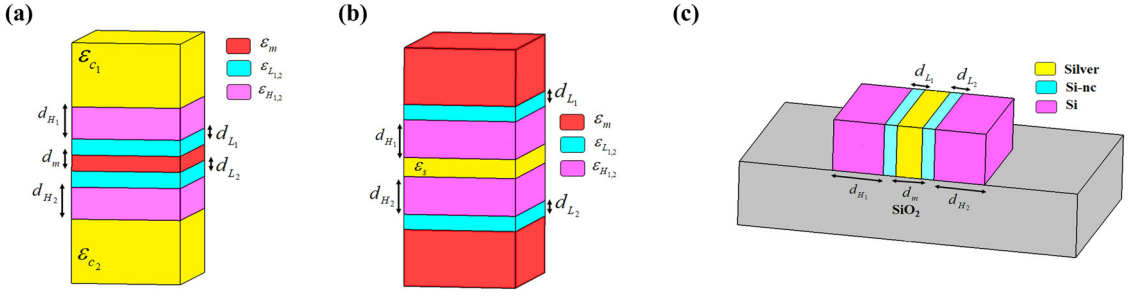

Figure 7: Three-dimensional perspective views of super-mode symmetric/asymmetric HPWs. (a) HIMI, (b) HMIM, and (c) vertical HIMI.

than the penetration depth, allowing for relatively strong coupling between SPPs on both sides of the structure. Conversely, reducing the metal thickness in the HIMI structure enhances the coupling of SPPs, causing the symmetric and asymmetric excited modes to diverge from each other more substantially. Further analysis, based on coupling theory, reveals that strong coupling occurs predominantly for symmetric structures. Hence, for both HMIM and HIMI configurations, the propagation loss in symmetric structures is less than in their asymmetric counterparts. Despite these advantages of symmetric HPWs, their performance is constrained by the fabrication process and the choice of the substrate material. When a silica substrate is used, it not only disrupts the symmetry of the upper and lower dielectric layers but it also leads to a decrease in propagation length and an increase in spatial length [86,89].

Vertical super-mode HPWs, comprising a vertical metal layer nestled between two high-index and low-index layers, entail a less complex fabrication process compared to their horizontal counterparts with a high aspect ratio, as shown in Figure 7(c) [85].

Following this practical perspective, asymmetric HIMI and symmetric HMIM waveguides are deemed favorable, given the constraints of fabrication. Leveraging the analytical method introduced in Section 2, the dispersion function ($F(\gamma)$) for both HIMI and HMIM structures can be defined as follows [86,89]:

$$F(\gamma) = -j\left(\frac{k_s}{\varepsilon_s}m_{11} + \frac{k_c}{\varepsilon_c}m_{22}\right) - m_{21} + \frac{k_s k_c}{\varepsilon_s \varepsilon_c} = 0, \qquad (6)$$

where $k_{s,c} = \sqrt{\gamma^2 - k_0^2\varepsilon_{s,c}}$ and $\varepsilon_{s,c}$ are the attenuation coefficient and dielectric constant of the substrate and cladding, respectively. Also, m_{ij} coefficients are the total transfer matrix (M_T) elements resulting from the products of M_n (n = 1, ..., N: number of layers) written as follows [86,89]:

$$M_T = M_1 M_2 \ldots M_N = \begin{pmatrix} m_{11} & m_{12} \\ m_{21} & m_{22} \end{pmatrix}, \quad M_n = \begin{pmatrix} \cos(k_n d_n) & -j\frac{\varepsilon_n}{k_n}\sin(k_n d_n) \\ -j\frac{k_n}{\varepsilon_n}\sin(k_n d_n) & \cos(k_n d_n) \end{pmatrix}, \qquad (7)$$

where $k_n = \sqrt{k_0^2\varepsilon_n - \gamma^2}$, ε_n, and d_n are transverse wave number, dielectric constant, and thickness of each layer, respectively.

Khodadadi and Nozhat have numerically and theoretically explored a practical CMOS-compatible HPW composed of horizontally arranged Si–SiO_2–Al–SiO_2–Si layers, as shown in Figure 8(a). A theoretical and numerical comparison between the short-range and long-range supermodes of the proposed symmetric HPW is depicted in Figure 8(b) and (c) [125].

3.2 Circular HPWs (CHPWs)

Certainly, as stated earlier, RHPWs can confine light in one dimension. To implement HPWs that support two-dimensional light confinement, a CHPW can be designed. This

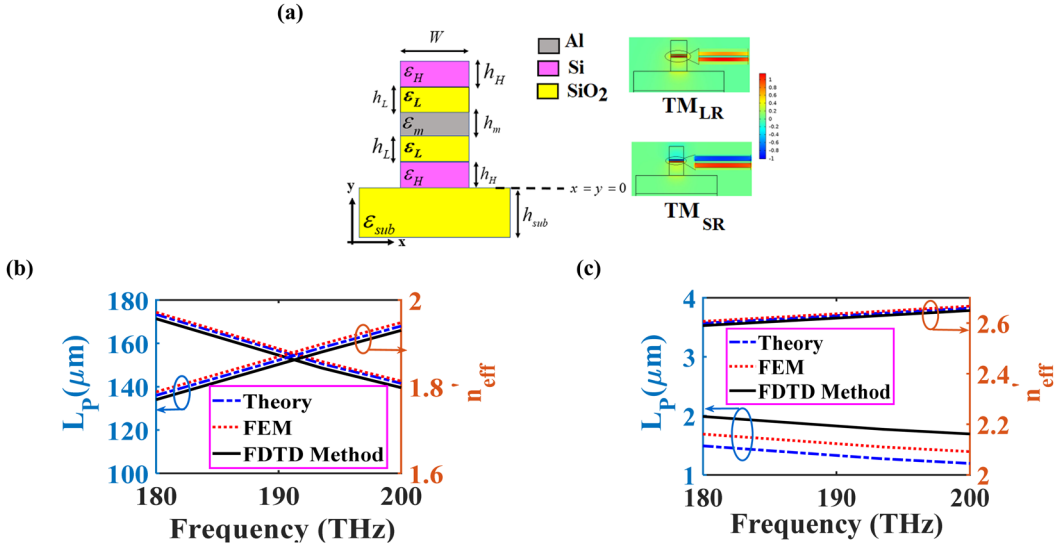

Figure 8: (a) Cross section of symmetric HPW. Spectra of propagation length and real part of effective refractive index of the proposed symmetric HPW for (b) long-range and (c) short-range fundamental TM modes. h_L = 20 nm, h_H = 220 nm, h_m = 10 nm, h_{sub} = 310 nm, W = 250 nm, ε_L = ε_{sub} = 2.07, and ε_H = 12.09, and the relative permittivity of ε_m is extracted from the Johnson- Christy data. Adapted with permission from the study by Khodadadi and Nozhat [125], © IEEE.

type of waveguide consists of low-index and high-index dielectric layers and a metallic layer.

According to Figure 9, three different configurations are typically present for the design of a CHPW:

(1) Metal core: Here, a metal core is surrounded by a low-index layer and then by a high-index dielectric cladding.
(2) Metal cladding: In this configuration, a high-index core is surrounded by a low-index dielectric layer, which in turn is wrapped in a metallic cladding layer.
(3) Semiconductor nanowires: In this scenario, a metallic nanowire is sandwiched between semiconductor nanowires, each surrounded by a low-index dielectric cladding.

These configurations are introduced to achieve two-dimensional light confinement, offering flexibility in designing and tailoring the optical properties of waveguides to meet specific requirements [126–132].

The electric field distributions of CHPWs displayed in Figure 9(a) and (b), at their circular cross sections, demonstrate that only the fundamental TM_{01} mode can be confined within the low-index layer [126,128,132]. Essentially, by harnessing the capabilities of nanowires and merging them with the features of HPWs, it is possible to attain subwavelength mode confinement and ultra-long propagation lengths [130,133–135]. Joeng *et al.* have reported an ultra-long propagation length of over 103 μm and a robust mode confinement on the order of 10^{-4} in normalized effective mode area, with a structure that consists of a silica nanowire sandwiched between a gold metallic core and an indium gallium arsenide (InGaAs) layer, as shown in Figure 9(a) [126]. Even though this CHPW design resulted in extremely low loss and tightly confined mode, the fabrication process, especially the growth of metallic core nanowire, poses significant challenges [136]. To address this, Xu *et al.* have proposed a structure with a dielectric nanowire enveloped in a silver cladding, as schematically portrayed in Figure 9(b), which notably decreased the propagation length to 160 μm [128]. The notable differences between the structures shown in Figure 9(a) and (b) can be attributed primarily to the loss compensation facilitated by the high-index layer of InGaAs, an active and gain medium resulting from the band-to-band recombination effect. Secondly, the increased radius of the metallic cladding nanowire significantly impacts the effective loss of the CHPW [126,137].

Fabricating CHPW involves several complex steps, such as the growth of the outer nanowire, etching a hole in the cladding layer, and then filling the structure with a low-index shell and core nanowire [126]. However, due to the complexity of the etching and filling steps, an alternative CHPW structure composed of three parallel nanowires

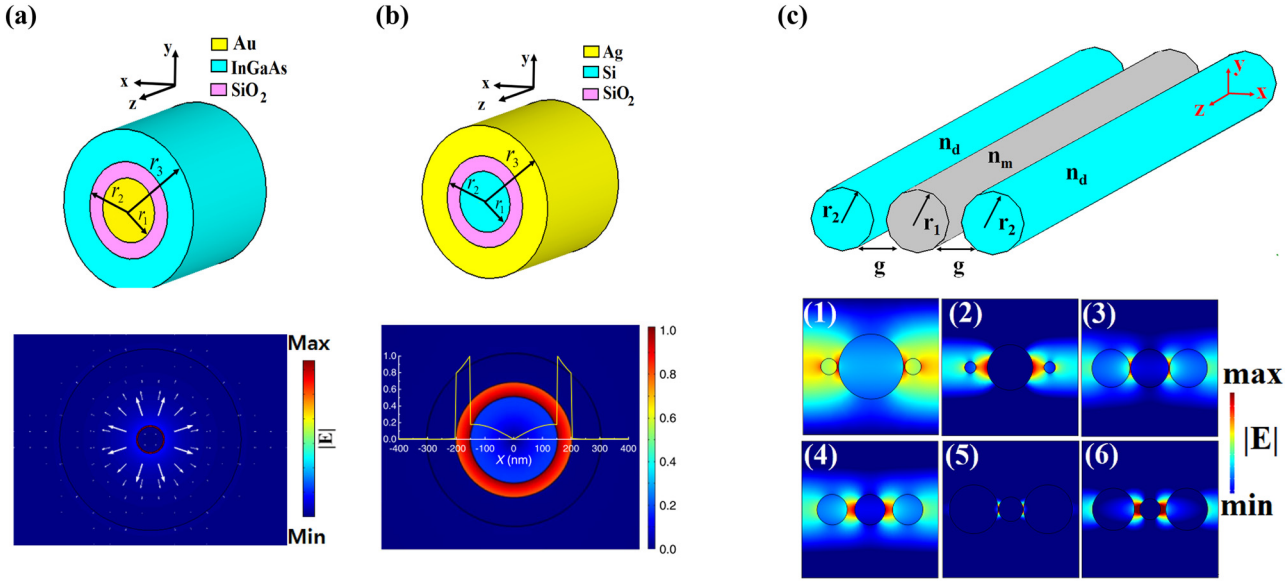

Figure 9: Three-dimensional schematic view of CHPWs and electric field distributions of the fundamental mode of TM_{01}: (a) metallic core (r_1 = 10 nm, r_2 = 11 nm, r_3 = 66 nm, ε_{InGaAs} = 13.84, ε_{SiO_2} = 2.1055, ε_{Au} = −115.13 + j 11.259) (b) metallic cladding nanowires (r_1 = 150 nm, r_2 = 200 nm, r_3 = 300 nm, ε_{Si} = 12.09, ε_{Ag} = −129.17 + j 3.2841) at 1,550 nm. (c) CHPW based on semiconductor nanowires placed on both sides of metallic nanowire symmetrically and its electric field distributions for different geometrical structures at 1,550 nm ((1) [r_1, r_2, g] = [100, 25, 5] nm, (2) [r_1, r_2, g] = [100, 25, 50] nm, (3) [r_1, r_2, g] = [100, 100, 5] nm, (4) [r_1, r_2, g] = [100, 100, 50] nm, (5) [r_1, r_2, g] = [100, 200, 5] nm, (6) [r_1, r_2, g] = [100, 200, 50] nm). (a) Adapted with permission from the study by Jeong *et al.* [126], © Optica Publishing Group. (b) Adapted with permission from the study by Xu *et al.* [128], © Optica Publishing Group.

has been proposed, as displayed in Figure 9(c). This proposed CHPW not only offers a propagation length of 1 mm, but its effective mode area is also around 0.038 μm^2.

Figure 10 provides a clear comparison between the advantages of CHPW, metallic wire waveguide [138], and dielectric wire HPW [114]. It is evident that the most optimal values for both propagation length and normalized effective mode area can be obtained by employing a CHPW with a low-index layer radius of r_1 = 2 nm [126]. This comparison underscores the potential of CHPWs in achieving exceptional performance characteristics in terms of light propagation and mode confinement.

The theoretical analysis by Khodadadi *et al.* offers the first detailed exploration of the properties of CHPWs and shows their superior performance over other wire structures [132]. To meet the conditions necessary for the excitation of SPPs ($n_i^2k_0^2 - \beta^2 < 0(n_i = \sqrt{\varepsilon_i}(i = 1, 2, 3))$), the modified Bessel function of the first and second kind is used to calculate variations in electric and magnetic fields in relation to the radial coordinate r. These calculations apply specifically to the inner and outer nanowire layers of CHPW. Figure 11 illustrates a comparison of the propagation length and real part of the effective refractive index for the CHPW structure (from Figure 9(a)) with parameters r_1 = 80 nm, r_2 = 115 nm, r_3 = 235 nm. These results are analyzed using two numerical approaches of FEM and FDTD method [132].

3.3 Modified HPWs

Apart from traditional rectangular and circular HPWs [65–132], several modified HPWs have been proposed as attractive solutions to address the inevitable trade-off between loss and confinement [139–159]. One such modification involves introducing a ridge on top of the high-index layer in a conventional HPW. This results in improvements in both propagation length and effective mode confinement [139]. In particular, for structures with the same parameters, the propagation length of the modified HPW has increased from 80 to 130 μm, and the normalized effective mode area has decreased from 0.9 to 0.05 [139]. Consequently, these results suggest that the modified structure outperforms conventional HPWs.

Modified HPWs encompass a range of configurations including dielectric or metal wedge or ridge [139–147], bow-tie [148], combinations of ridge or wedge structures with dielectric nanowire [149–153], terahertz (THz) and UV-modified CHPWs [154–156], vertical IMI structures with dielectric wire [157], and two identical dielectric nanowires situated on each side of a thin metallic film [158,159]. Various types of modified HPWs are shown in Figure 12. A comparison of an HPW with a silver-coated dielectric wedge (Figure 12(a)) and a channel HPW with an upside-down triangular high-index dielectric wedge embedded inside the silver groove (Figure 12(b)) shows that although their propagation lengths are comparable, the normalized effective mode area of the channel HPW is much smaller than the wedge metal. This can be attributed to the strong coupling between dielectric and plasmonic modes in the channel HPW [141,145]. Indeed, it is important to note that metallic groove structures can support channel plasmon polaritons (CPPs). In comparison to conventional CPP waveguides, the mode confinement of CPP HPWs is much stronger [141,145]. However, the angle and lateral misalignments of

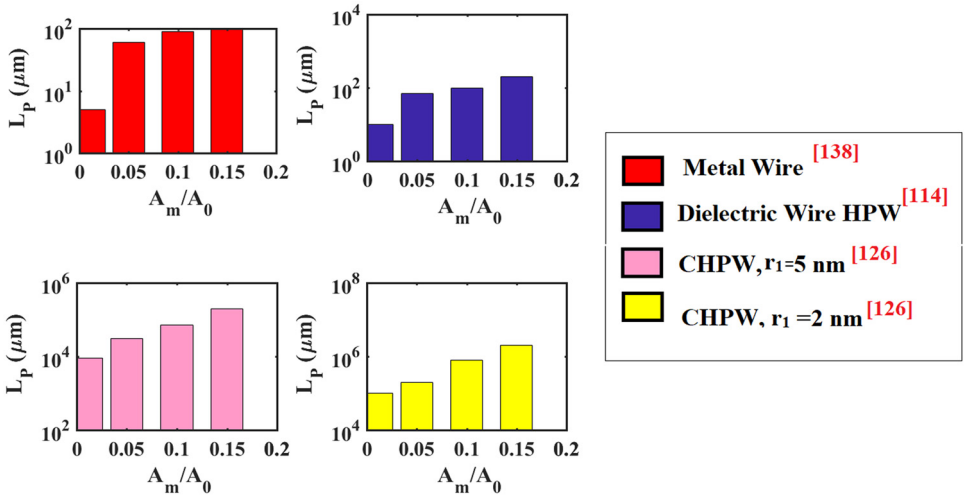

Figure 10: Propagation length *versus* normalized effective mode area for different wire structures to show the superiority of CHPW with metallic core nanowire. This figure is produced by the authors based on data extracted from previous studies [114,126,138].

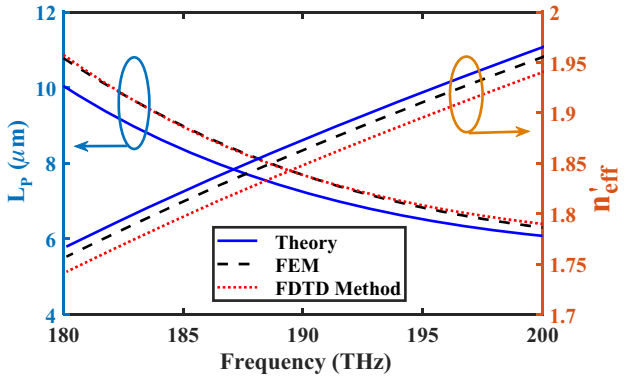

Figure 11: Spectra of propagation length and real part of the effective refractive index of CHPW with the metallic core nanowire. Adapted with permission from the study by Khodadadi *et al.* [132], © Nature Publishing Group.

HPWs with ridge and wedge structures can complicate the fabrication process. To mitigate this, Bian *et al.* have proposed a CPP HPW with relatively low confinement by introducing a trapezoidal upside-down silver ridge to avoid the lateral misalignment issue [160].

Furthermore, near-field optical tweezers are powerful devices capable of manipulating nanoscale objects. They can apply optical forces to control molecules and biological particles such as red blood cells [140,161,162], DNA [163], proteins [164], and bacterial cells [165]. One strategy to enhance the mode confinement of HPWs involves improving the optical force, leading to different configurations of modified HPWs [148,150,152] including a triangular upside-down high-index wedge above the metallic film (Figure 12(c)) [166], a bow-tie structure (Figure 12(d)) [148], a high-index dielectric nanowire embedded in a dielectric-coated V-shaped metal groove (Figure 12(e)) [153], a high-index dielectric nanowire positioned above a triangular metal wedge (Figure 12(f)) [150], and two identical dielectric nanowires above a diamond-shaped metal wire (Figure 12(g)) [152]. All these modified HPWs can focus light into the gap between the vertex of the ridge or wedge and the film or nanowire layer, providing enhancements suitable for improving the performance of near-field optical tweezers.

Indeed, when compared to the high-index structures with square and circular cross sections atop the metal film in modified HPWs, the triangular one (Figure 12(c)) demonstrates superior performance with a long propagation length (almost 47 μm) and a minimum normalized effective mode area (on the order of 0.09). This superior performance is mainly attributed to the fact that between 20 and 40% of the total power resides in the high-index nanowire region [166]. Also, 30–40% of the total excited power can be confined on both sides of the high-index GaAs nanowire as depicted in Figure 12(g), which leads to a stronger mode confinement compared to the conventional HPW. However, it is also important to highlight that fabrication limitations must be considered in practical scenarios. For instance, instead of a sharp triangle tip, a round corner with a nonzero radius is often formed due to manufacturing constraints [166]. This implies that in practice, the ideal geometric configurations may not always be fully realized due to these limitations.

Zhang *et al.* have proposed modifications to the HPW as illustrated in Figure 12(g), leading to a substantial propagation length of approximately 1,000 μm when θ equals 140°. However, these adjustments also amplify the intricacy of fabrication process.

As a result, investigating the tolerance of fabrication process to errors is essential, as these errors can lead to specific outcomes. For example, a horizontal misalignment of ±10 nm can result in a 6% change in propagation length and a 4% variation in effective mode area. In contrast, vertical asymmetries have little effect on the propagation length. A variation of ±5° in the wedge tip angle can cause fluctuations of 5% in propagation length and 10% in mode confinement. Moreover, a rotation of ±10° in the metal wire can affect the mode characteristics [152].

Tian *et al.* have demonstrated that substituting dielectric nanowires with nanotubes enhances the flexibility in tuning the optical attributes of the structure represented in Figure 12(h). It also reduces the propagation loss when compared to traditional nanowire HPWs, resulting in superior mode confinement [156,158]. By introducing a high index nanowire atop the vertical rib-slot-rib configuration, as depicted in Figure 12(i), an ultra-strong mode squeezing with a mode area of 200 μm² and a significantly extended propagation length of 23.78 μm have been achieved when compared to conventional HPWs [157]. Moreover, the investigations showed that a curved silver rib with a radius of 9 nm can extend the propagation length by more than 5 μm, which is attributed to the reduced light scattering from uncurved silver ribs [157].

Figure 12(j) shows a modified THz HPW made up of a Si microwire on the top of a GaAs curved ridge. This arrangement yields a tightly squeezed mode area that varies between $\lambda^2/360$ and $\lambda^2/156$, with propagation lengths ranging from 374 to 506 μm [154]. Building upon these enhancements, He *et al.* have suggested a gain-assisted THz HPW to further boost performance, achieving a maximum propagation length of 1,200 μm [155].

To date, a variety of HPWs, such as those discussed earlier, have been proposed for various applications including nanolasers, plasmonic systems, and biological uses, particularly at the popular telecommunication wavelength of

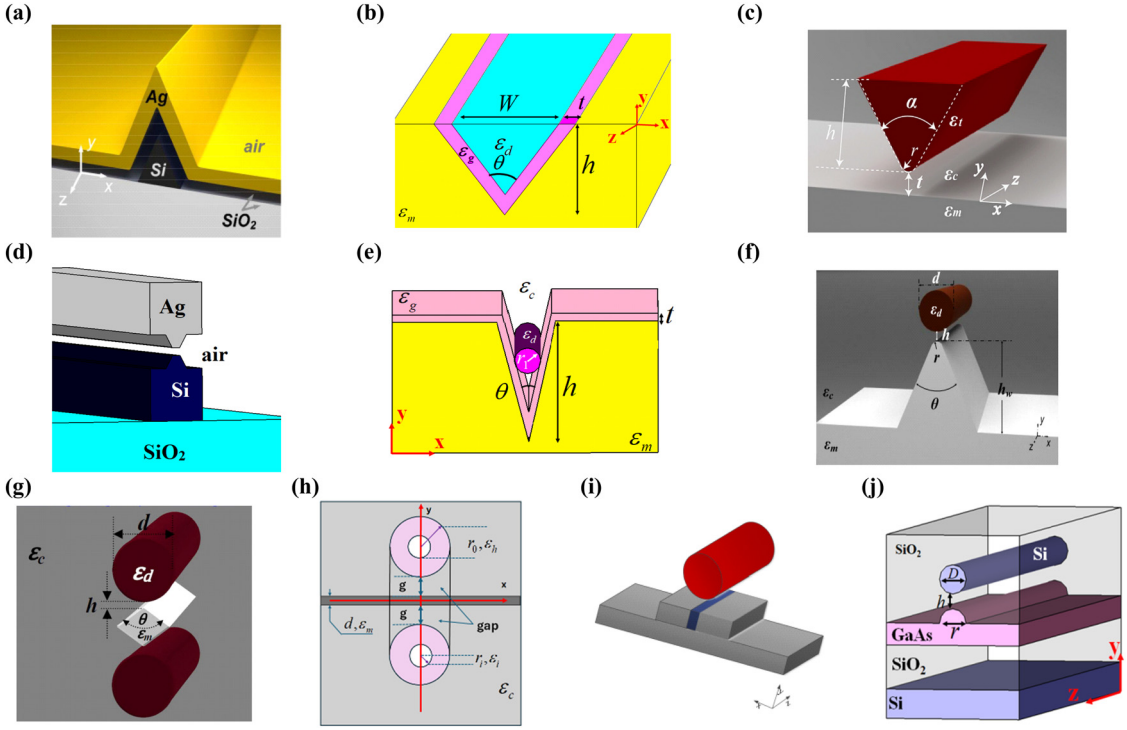

Figure 12: Different types of modified HPWs. (a) Triangular silver-coated silicon wedge (reproduced with permission from the study by Bian and Gong [141], © Optica Publishing Group), (b) triangular upside-down high-index wedge inside the metal groove, (c) triangular upside-down high-index wedge above the metallic film (reproduced with permission from the study by Lu *et al.* [166], © Elsevier), (d) bow-tie structure, (e) high-index dielectric nanowire embedded in a dielectric-coated V-shaped metal groove, (f) high-index dielectric nanowire placed above a triangular metal wedge (reproduced with permission from the study by Bian *et al.* [150], © Optica Publishing Group), (g) two identical dielectric nanowires above a diamond-shaped metal wire (reproduced with permission from the study by Zhang and Wang [152], © Nature Publishing Group), (h) two identical dielectric nanotubes placed on each side of a thin metallic film, (i) high-index nanowire above a vertical IMI waveguide (reproduced permission from the study by Zheng *et al.* [157], © American Institute of Physics), and (j) THz modified HPW.

1,550 nm due to its reduced metal absorption [65–154]. Recently, THz semiconductor plasmonics have garnered substantial attention [154]. There have been numerous efforts to develop THz HPWs with extended propagation lengths for both scientific and industrial applications [154–156,166,167]. In addition, the significant advancements in nanolaser technology have necessitated shorter wavelengths, such as those in the UV band [156,168,169]. UV Raman spectroscopy also plays a crucial role in detecting biological particles [156,170]. To cater to these needs, Li *et al.* have suggested, for the first time, a UV HPW designed for nanolaser applications. Their design comprises an Al ridge and a high-index GaN nanowire positioned atop a low-index MgF_2 slab, making it compatible with CMOS techniques [156]. This innovative approach significantly improves the performance of UV HPWs compared to metallic film UV waveguides. The introduction of a ridge metal results in a normalized effective mode area of 0.0359 and a propagation length of 1027.3 nm [156].

Finally, a crucial geometrical factor in modified HPWs is the angle of the groove and wedge. According to the results of the study by Bian *et al.* [145], the conventional CPP waveguide with the groove angle of 25° exhibits low transmission loss, resulting in a longer propagation length of 200 μm. However, it has a large effective mode area. By introducing the modified HPW (Figure 12(b)), the effective mode area significantly decreases by two orders of magnitude while maintaining a reasonable propagation length [145]. Further, as suggested by the data from the study by Bian *et al.* [160], the sidewall angle significantly influences the optimization of loss-confinement relationship in modified HPWs. It is clear that by selecting larger angles, the propagation length can be considerably extended compared to the conventional HPW.

In conclusion, for a comprehensive understanding of advantages and disadvantages of various HPW types, Table 1 offers a detailed performance summary of each.

3.4 Nonlinear HPWs

The impressive capabilities of optical nonlinearities, including high-speed signal switching and demultiplexing [171],

Table 1: Summary of advantages and limitations of different configurations of HPWs

Ref.	Topology	λ (nm)	A_m/A_0	L_p (μm)
[28]	VRHPW[a)]	1,550	—	10
[29]	CHPW	1,550	0.2	10^8
[30]	RHPW	1,550	0.1	30
[45]	RHPW	1,550	—	450
[46]	RHPW	1,550	0.175	6
[48]	RHPW	1,550	0.0685	142
[50]	ASHPW[b)]	1,550	0.076	2.49×10^3
[55]	ASHPW	1,550	4.89×10^{-2}	2.69×10^4
[56]	ASHPW	1,550	0.38	6
[57]	ASHPW	1,550	0.076	2.49×10^3
[77]	RHPW	1,550	0.01	400
[79]	RHPW	1,550	0.066	176
[80]	RHPW	1,200	2.33	400
[81]	SHPW[c)]	1,550	0.05	10^4
[82]	SHPW	1,550	2.16×10^{-3}	696
[85]	VSHPW[d)]	1,550	—	14.5
[87]	SHPW	1,550	—	1,500
[88]	MCHPW[e)]PW	1,550	0.01	10^4
[92]	SHPW	1,550	0.07	113
[93]	RHPW	1,550	—	1,250
[95]	CRHPW[f)]	1,550	—	10
[96]	CRHPW	1,550	0.053	60
[97]	CRHPW	1,550	—	10
[99]	CRHPW	1,550	0.011	25
[102]	RHPW	575	0.04	23
[104]	RHPW	1,550	—	1,000
[115]	MCHPW	1,550	0.006	40
[127]	CHPW	1,550	0.1	—
[128]	CHPW	1,550	0.11	20
[129]	CHPW	1,550	0.06	15
[130]	CHPW	1,550	0.69×10^{-3}	1,260
[131]	CHPW	1,550	0.009	20
[139]	MRHPW[g)]	1,550	0.02	50
[141]	MHPW[h)]	1,550	0.35	100
[145]	MHPW	1,550	0.08	25
[146]	MHPW	1,550	4.71×10^{-3}	26
[148]	MHPW	1,550	1.57×10^{-4}	138
[150]	MHPW	1,550	0.02	20
[151]	MHPW	1,550	0.06	110
[152]	MHPW	1,550	0.06	1,000
[153]	MHPW	1,550	0.07	20
[154]	MHPW	THz	0.01	506
[155]	MHPW	1 THz	0.3	1,200
[156]	MHPW	UV	0.0359	1027.3
[157]	MCHPW	1,550	8×10^{-4}	21.59
[158]	MCHPW	1,550	0.14	1,000
[160]	MRHPW	1,550	0.15	35
[166]	MRHPW	1,550	0.09	46.5

[a)]Vertical RHPW, [b)]Asymmetric HPW, [c)]Symmetric HPW, [d)]Vertical SHPW, [e)]Modified CHPW, [f)]Covered RHPW, [g)]Modified RHPW, and [h)]Modified HPW.

wavelength conversion [172], light amplification [173], and supercontinuum generation [172], have spurred increasing interest in the study of nonlinear waveguides. Incorporating these capabilities into an on-chip photonic platform could provide advantages in cost, footprint, energy efficiency, and overall performance. The pioneer platform for integrated nonlinear optics has traditionally been SOI due to the silicon compatibility with CMOS fabrication technology [172]. While silicon, with its high refractive index and third-order susceptibility, is suitable for efficient nonlinear interactions at low power levels, it suffers from two primary drawbacks: strong two-photon absorption (TPA) and incompatibility with device footprints smaller than 100 μm. Furthermore, purely dielectric waveguides exhibit reduced nonlinear effects due to their confinement limitations [172]. This is because field confinement is essential for achieving significant nonlinear effects, as it enhances light-matter interactions while maintaining low power requirements. To address this limitation, longer propagation lengths are required to observe noticeable nonlinear effects, which in turn increases the overall footprint. Therefore, platforms that can enhance effective nonlinearity while reducing the required propagation lengths are more desirable, depending on the application. In this regard, two approaches have been proposed: (1) combining SOI waveguides with polymers such as 2-[4-(dimethylamino) phenyl]-3-([4(dimethylamino)phenyl]-ethynyl) buta-1,3-diene-1,1,4,4 tetra carbonitrile (DDMEBT), poly[2,4-hexadiyne-1,6-dial-bis(p-toluenesulfonate)], and (2) introducing hybrid plasmonic platforms which generate strongly confined fields to increase nonlinear interactions, potentially reducing device footprints [172,174–177].

In addition, the combination of these methods enables the creation of ultra-dense silicon waveguides with strong field confinement, achieving exceptional third-order nonlinear effects while maintaining low nonlinear losses [178]. Diaz *et al.* conducted the first experimental investigation into third-order nonlinear effects in HPWs, using a configuration where a thin layer of silicon nitride (Si_3N_4) is sandwiched between a 100 nm gold film and a silicon nanowire (Figure 13(a)) [179]. In this design, the nonlinearity is explored within the Si_3N_4 layer, which is crucial for confining and propagating the excited TM mode. The obtained results show that 5 nm Si_3N_4 layer generates a stronger nonlinear signal compared to the 10 nm layer. However, the proposed configuration with high confined intensity in the Si_3N_4 layer cannot beat conventional silicon nanowires [179].

Third-order nonlinear effects arise from the third-order susceptibility of a material, where the polarization

response to an applied electric field is not directly proportional to the field but involves cubic terms in the field intensity. These nonlinearities are particularly significant in optics when dealing with high-intensity light such as laser beams. Among the various third-order effects, the most common phenomenon is the optical Kerr effect ($n(I) = n_0 + n_2 I$), where the refractive index of a material (n_0) changes with light intensity (I) [178]. In recent decades, the Kerr nonlinear effect has garnered increased attention compared to two-photon and free-carrier absorption due to its ultrafast response in all-optical switching devices [174], paving the way for further investigation into the Kerr nonlinear effect in HPWs.

A key metric for demonstrating the superiority of nonlinear effect across different HPWs is the efficient nonlinear coefficient [175]:

$$\gamma = 2\pi\bar{n}_2/\lambda A_m, \quad \bar{n}_2 = \frac{\varepsilon_0 \iint n_0^2 n_2 [2\,|\mathbf{E}|^4 + |\mathbf{E}^2|^2]\mathrm{d}A}{3\mu_0 \iint |\mathbf{E} \times \mathbf{H}^* \cdot \hat{z}|^2 \mathrm{d}A}, \quad (8)$$

where μ_0, n_0, n_2, and $\bar{n}_2$ are vacuum permeability, linear refractive index, nonlinear refractive index, and the average value of the effective nonlinear refractive index, respectively. Also, **E** and **H** are electric and magnetic fields, respectively.

To date, the largest calculated $\gamma \approx 10^4 (\mathrm{W^{-1}\,m^{-1}})$ for HPW platforms was reported by Pitilakis and Kiezis (Figure 13(b)), where the highly nonlinear organic polymer DDMEBT was selected as the gap material [177]. As depicted in Figure 13(c), a novel high figure of merit (FOM) silicon hybrid waveguide has been developed by integrating an IMI structure. This design utilizes highly nonlinear DDMEBT and silver materials within a silicon slot to effectively confine the optical field. The introduction of two rectangular silicon nanobridges plays a crucial role in mitigating propagation losses, which are often a limiting factor in hybrid plasmonic systems. The DDMEBT layer, being highly nonlinear, serves as the primary medium for nonlinear interactions while also benefiting from negligible TPA. This absence of TPA is significant, as it ensures that the system can operate efficiently even under high incident power without the detrimental effects of power-induced absorption losses [180]. The combination of these factors – strong optical confinement, reduced loss, and enhanced nonlinearity – enables the waveguide to achieve a high FOM of 0.55 at a wavelength of 2.1 μm. This performance demonstrates the potential of hybrid waveguide configuration for applications requiring both high optical field confinement and efficient nonlinear response, such as in all-optical switching, signal processing, and sensing. Figure 13(d) shows the FOMs of four waveguides as the incident power varies at the wavelength of 2 μm. The FOM of the metal–insulator waveguide is low. The silicon hybrid waveguide has a comparable FOM with the symmetric hybrid plasmonic (SHP) and SOI waveguides when the incident power is low, but it has an obvious advantage in FOM when the incident power is larger than 1 W [180].

While DDMEBT-based platforms demonstrate significant potential, recent advancements have also drawn attention to alternative materials with exceptional nonlinear properties such as graphene. Graphene has gained significant attention in the field of nonlinear optics because of its extremely high third-order nonlinear susceptibility, which leads to strong nonlinear effects even at relatively low power levels. Its atomic thickness, combined with exceptional electrical and thermal conductivity, makes it a promising candidate for integrating with plasmonic structures to enhance nonlinear processes. The ability of graphene to support high-intensity optical fields and its ultrafast carrier dynamics open new possibilities for applications requiring efficient nonlinear responses, such as in broadband optical signal processing, all-optical switching, and high-speed communications. In addition, the tunability of graphene *via* electrostatic gating allows for dynamic control over its optical properties, making it a highly flexible material for next-generation photonic devices. Jin *et al.* have proposed a graphene-silicon hybrid waveguide to significantly enhance the nonlinear optical response and achieve ultra-wide bandwidth coverage spanning both near-infrared (NIR) and mid-IR regions (Figure 13(e)) [181]. In a degenerate four-wave mixing (FWM) process, the conversion efficiency reaches −18.5 dB with a pump power of just 0.5 W and a waveguide length of only a few tens of microns. This configuration achieves a 3 dB bandwidth of 40–110 nm for each fixed pump wavelength.

While several basic nonlinear HPWs have been proposed, the next challenge is integrating them into more complex circuits with multiple functional and modular elements, akin to traditional PICs. Ideally, these circuits would be fully chip-based and compatible with standard photonic components, facilitating seamless integration with conventional technologies. Tuniz *et al.* have achieved a significant milestone by fabricating the world's first modular nonlinear hybrid plasmonic circuit, operating at a wavelength of 1.32 μm. As illustrated in Figure 13(f), the circuit consists of two key modules: a mode converter that efficiently transforms an incoming photonic TE mode into a hybrid-plasmonic TM mode, followed by a plasmonic nanofocuser. This nanofocuser functions as a nonlinear wavelength converter, experimentally demonstrating intensity enhancements exceeding 200 in a confined mode area of 100 $\mathrm{nm^2}$, at a pump wavelength of 1.32 μm [182]. In contrast to typical nonlinear HPWs, in this configuration, the high

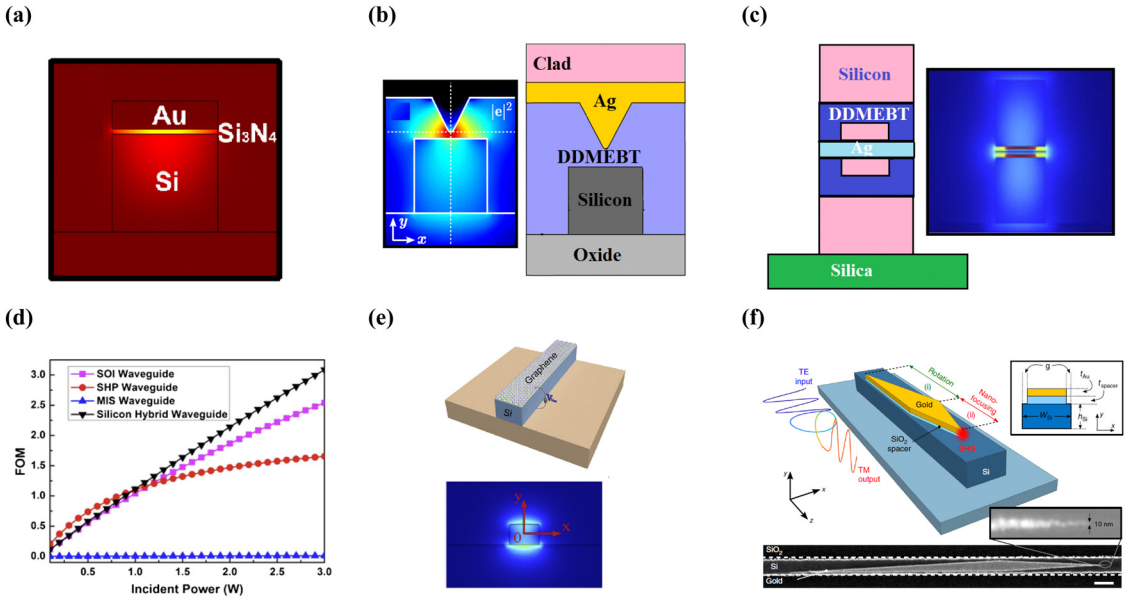

Figure 13: Nonlinear HPWs configuration and analysis. (a) Electric field distribution of a RHPW demonstrating the effectiveness of Si_3N_4 as a nonlinear material (reproduced with permission from the study by Diaz *et al*. [179], © Optica Publishing Group), (b) electric field distribution and configuration of an HPW utilizing the DDMEBT (reproduced with permission from the study by Pitilakis and Kiezis [177], © Optica Publishing Group), (c) electric field and 2D schematic view of an IMI HPW with two nonlinear sections (reproduced with permission from the study by Tu *et al*. [180], © Optica Publishing Group), (d) analysis of the FOM for various waveguide configurations as a function of incident power, highlighting the superiority of silicon-based HPWs (reproduced with permission from the study by Tu *et al*. [180], © Optica Publishing Group), (e) investigation of graphene nonlinear effect in an HPW for designing reconfigurable waveguides (reproduced with permission from the study by Jin *et al*. [181], © Nature Publishing Group), and (f) scheme and scanning electron micrograph of an SOI hybrid plasmonic circuit designed to achieve second-harmonic generation (SHG) modulation (reproduced permission from the study by Tuniz *et al*. [182], © Nature Publishing Group).

field intensities at the apex of the gold tip are utilized to estimate the field enhancement through nonlinear SHG experiments. Building on these advancements, further progress in developing highly efficient nanoscale coherent light sources is critical for a range of technological applications, including integrated photonic circuits, bioimaging, and sensing. One key step in this direction is the implementation of an on-chip wavelength converter based on SHG. However, achieving high light-conversion efficiency in small devices remains a significant challenge. To address this, recent efforts have demonstrated a strongly enhanced SHG with a high conversion efficiency of 4×10^{-5} W^{-1} in an HPW consisting of a cadmium selenide (CdSe) nanowire coupled with a gold film. This advancement represents a crucial step toward the realization of efficient, integrated nanoscale light sources [183].

In parallel, nonlinear HPWs are also driving innovations in all-optical logic operations. In the study by Dai *et al*. [184], all-optical logic operations, such as NOT, NOR, and NAND gates, have been theoretically demonstrated using polarization-dependent FWM processes in highly nonlinear silicon HPW microring resonators. An ultra-compact microring resonator with a radius of approximately 1 μm was designed, utilizing a silicon HPW capable of sub-wavelength bending. The HPW exhibits exceptionally high confinement ($A_{\text{eff}} \sim 0.045\ \mu m^2$), which, combined with a highly nonlinear gap material, results in a remarkably high nonlinear parameter ($\gamma \sim 3{,}000\ W^{-1}\ m^{-1}$). By manipulating the polarization properties of the pump and signals with a very low electric field ($|E| \sim 10^8$ V/m), these compact devices achieve stable all-optical logic operations [184]. In addition, to fulfill the need for monolithic integration of active and passive components on a single substrate, the utilization of indium gallium arsenide phosphide (InGaAsP) and indium phosphide (InP) has been proposed to achieve a dense PIC. In this context, Firouzabadi *et al.* have introduced a nonlinear shallow-etched HPW structure comprising a layer stack of Ag/DDMEBT/InGaAsP/InP [174,175].

It is essential to mention that in modeling nonlinear effects in HPW designs, both FEM and FDTD approaches offer ways to incorporate nonlinear response terms, though each method presents distinct advantages based on the type of nonlinearity and the temporal behavior of the system. FEM is particularly advantageous for steady-state nonlinear responses due to its inherent flexibility in defining complex material properties. This flexibility

enables precise modeling of nonlinear phenomena, such as Kerr effects, saturable absorption, or other intensity-dependent refractive index changes that may occur in steady-state conditions. Mesh adaptability of FEM allows it to concentrate computational resources in areas with strong nonlinear effects, enhancing accuracy while managing computational costs. Thus, FEM is often the preferred choice for nonlinear HPW simulations where the response does not vary significantly with time. On the other hand, FDTD is more suited to capturing time-dependent nonlinearities, as it operates in the time-domain and can naturally simulate dynamic changes in the field and material properties over time. This makes FDTD particularly effective for HPW designs involving transient nonlinear phenomena, where the response varies with the incident pulse or signal dynamics, such as in ultrafast processes or when studying the temporal evolution of nonlinear effects in response to a changing input. However, the inclusion of time-dependent nonlinearities in FDTD is computationally demanding. Accurately capturing these effects requires a fine spatial and temporal resolution, which increases both memory usage and processing time. This computational intensity makes FDTD more resource heavy than FEM for nonlinear modeling, especially in three-dimensional designs or in cases involving strong nonlinearity that necessitates very small time steps to maintain stability and accuracy. Therefore, the choice between FEM and FDTD for nonlinear modeling depends largely on the nature of the nonlinearity: FEM excels in steady-state scenarios with complex material properties, while FDTD is better suited to dynamic nonlinear processes, albeit at a higher computational cost.

In conclusion, Table 2 presents various details including topology, propagation length, nonlinear coefficient, and FOM (FOM = $\gamma L_p P_{0,th}$) for different nonlinear HPWs.

3.5 Graphene-based HPWs

As previously discussed, HPWs provide a practical solution to address the conundrum of balancing light confinement and low loss in PICs. In the realm of nanophotonics, graphene has recently garnered substantial interest as a two-dimensional material due to its remarkable properties. These include high electron mobility, strength, and stiffness; extraordinary thinness; transparency; impressive electrical and thermal conductivity; optical absorption of approximately 2.3% across the UV to IR spectrum; flexibility; low contact resistance; and a tunable chemical potential [191–195]. These unique characteristics make graphene particularly suitable for enhancing HPWs, especially at the widely used 1,550 nm wavelength in optical communication systems. At 1,550 nm, graphene enables enhanced light confinement and strong field localization by supporting SPPs at the graphene-dielectric interface. This allows the electric field to be concentrated at a subwavelength scale, which is crucial for minimizing device size in PICs and for increasing the interaction of light with the guided mode. Furthermore, the optical properties of graphene can be dynamically tuned by adjusting its chemical potential through electrical gating or doping, enabling real-time control of the waveguide performance. This tunability

Table 2: Comparison of the performance of Kerr nonlinear HPWs at 1,550 nm

Ref.	Topology	Nonlinear material	Composition	L_p (μm)	γ (W^{-1} m^{-1})	FOM
[172]	RHPW	DDMEBT	SOI-based	35	0.3×10^4	—
[174]	RHPW	DDMEBT	InP-based	135	6.4×10^2	0.02
[175]	RHPW	DDMEBT	SOI-based	120	$<1.06 \times 10^3$	0.03
[176]	RHPW	Polymer	SOI-based	—	$>8.5 \times 10^4$	—
[177]	MHPW	DDMEBT	SOI-based	29.3	10^4	—
[178]	RHPW	DDMEBT	SOI-based	400	10^2	—
[179]	RHPW	Si_3N_4	SOI-based	—	1.5×10^2	—
[180]	SHPW	DDMEBT	SOI-based	—	—	>0.54
[181]	RHPW	Graphene	SOI-based	105	6246.9	—
[183]	CHPW	CdSe	SOI-based	—	$<10^3$	—
[184]	RHPW	Silicon	SOI-based	100	3×10^3	—
[185]	RHPW	DDMEBT	SOI-based	60	5.7×10^3	0.03
[186]	RHPW	DDMEBT	InP-based	155	1.06×10^3	0.04
[187]	ASHPW	Si_3N_4	SOI-based	4.7×10^3	—	$>10^5$
[188]	ASHPW	Polymer	SOI-based	20	1×10^3	—
[189]	MHPW	Graphene	SOI-based	80	2.68×10^4	0.029
[190]	HPW	Graphene	SOI-based	—	7.36×10^5	2.10

is particularly valuable for designing reconfigurable optical devices, such as modulators and switches [196,197].

Moreover, graphene exhibits lower propagation loss compared to traditional metals like gold or silver, which typically suffer from high losses in the NIR region. This allows graphene-based HPWs to guide light over longer distances with less attenuation, thereby enhancing the overall efficiency of the device [198]. Another important advantage of graphene is its strong nonlinear optical properties, which are especially pronounced at 1,550 nm. These properties facilitate the development of ultrafast optical modulators and switches [181,189]. As a result, graphene-based HPWs offer a novel approach to reducing the effective mode area while improving propagation length, outperforming conventional graphene-based waveguides across both visible and THz frequencies [194].

Importantly, graphene surface conductivity is almost entirely imaginary at THz and far-IR frequencies, making it an ideal candidate for the proposal and fabrication of THz devices with specific applications like optical modulation, filtering, and near-field imaging [191–195]. Manipulating light is central to modern PICs. This can be achieved by actively tuning graphene chemical potential with an appropriate applied gate voltage (V_g) [193]. While graphene, similar to noble metals, suffers from absorption loss, this can be mitigated by raising its Fermi level [194]. The optical properties of graphene are introduced by its surface conductivity ($\sigma_g(\omega, \mu, \tau, T) = \sigma_{\text{intra}}(\omega, \mu, \tau, T) + \sigma_{\text{inter}}(\omega, \mu, \tau, T)$) based on the Kubo formula [192]. Therefore, the complex permittivity of monolayer graphene ($\varepsilon_g(\omega, \mu, \tau, T)$) with a thickness of $\Delta = 0.34$ nm can be written as follows:

$$\varepsilon_g(\omega, \mu, \tau, T) = 1 + j\frac{\sigma_g(\omega, \mu, \tau, T)}{\omega\varepsilon_0\Delta}. \tag{9}$$

Leveraging the electro-absorption effect of graphene, Hu and Wang have proposed a graphene-based HPW with a rectangular and symmetric cross section. This structure consists of two graphene layers sandwiched between a silicon strip and a low-index layer, as shown in Figure 14(a) [192]. It can be seen that the attenuation of the long-range graphene-based HPW can be regulated by tuning graphene chemical potential, rendering it suitable for covering the entire O, E, S, C, L, and U telecommunication bands. Vahed and Ahmadi have studied the effect of a number of graphene layers on the attenuation of a graphene-based HPW, composed of a graphene-hexagonal-boron-nitride-graphene (graphene–hBN–graphene) sandwich [193]. The study indicates that as the number of graphene layers increases, the attenuation enhances due to the relationship between the loss and the imaginary part of the effective refractive index of the proposed structure at 1,550 nm (Figure 14(b)).

In parallel, graphene plays a crucial role in enabling HPWs in the THz frequency range due to its remarkable electrical and optical properties. One of the key advantages of graphene is its high carrier mobility and tunability, which allow it to support SPPs at THz frequencies. In addition, graphene conductivity can be dynamically tuned by adjusting its chemical potential through electrical gating or chemical doping, which allows for real-time control of the plasmonic response. This feature is especially beneficial in the THz range, where precise control over plasmon propagation is essential. Moreover, graphene exhibits much lower losses at THz frequencies compared to metals, making it a highly efficient material for supporting long-range plasmonic modes, which is crucial for high-performance HPWs [194,195].

In HPWs, graphene is typically combined with a dielectric or metal to confine electromagnetic fields between two materials. This hybridization results in enhanced light-matter interactions, especially in the THz range where such interactions are more challenging to achieve with traditional materials. The strong field confinement at the graphene interface, combined with the low loss propagation in dielectrics, leads to significant improvements in the FOM for these waveguides. As a result, graphene-based HPWs offer better field confinement, reduced losses, and dynamic tunability, which are critical for a wide range of THz applications such as sensing, imaging, and communication systems. These properties make graphene an ideal material for advancing the development of efficient THz waveguides, where traditional approaches struggle with high losses and limited confinement at such frequencies. However, one significant challenge in designing a graphene-based HPW for THz frequencies lies in reducing the effective mode area. This could be achieved by narrowing the gap between the high-index layer and graphene sheets, but practical considerations limit further downscaling of this gap. To address this issue, He *et al.* have proposed a novel graphene-based HPW comprising a low-index SiO_2 rectangular layer situated between a high-index cylindrical GaAs layer and a substrate coated with graphene, as depicted in Figure 14(c) [194]. This innovative approach results in obtaining an impressively small normalized effective mode area of 0.0018 at 3 THz, along with ultra-low crosstalk. Building on this approach, Chen *et al.* have examined a symmetric THz graphene-based HPW, as demonstrated in Figure 14(d). This design incorporates two Si cylindrical layers positioned on either side of a graphene sheet, achieving an effective mode area and propagation length of 4 μm² and 26.7 μm, respectively, at the frequency of 10 THz [195]. As a result, the combination of graphene and HPWs holds significant promise for proposing and fabricating actively controllable and cutting-edge PICs.

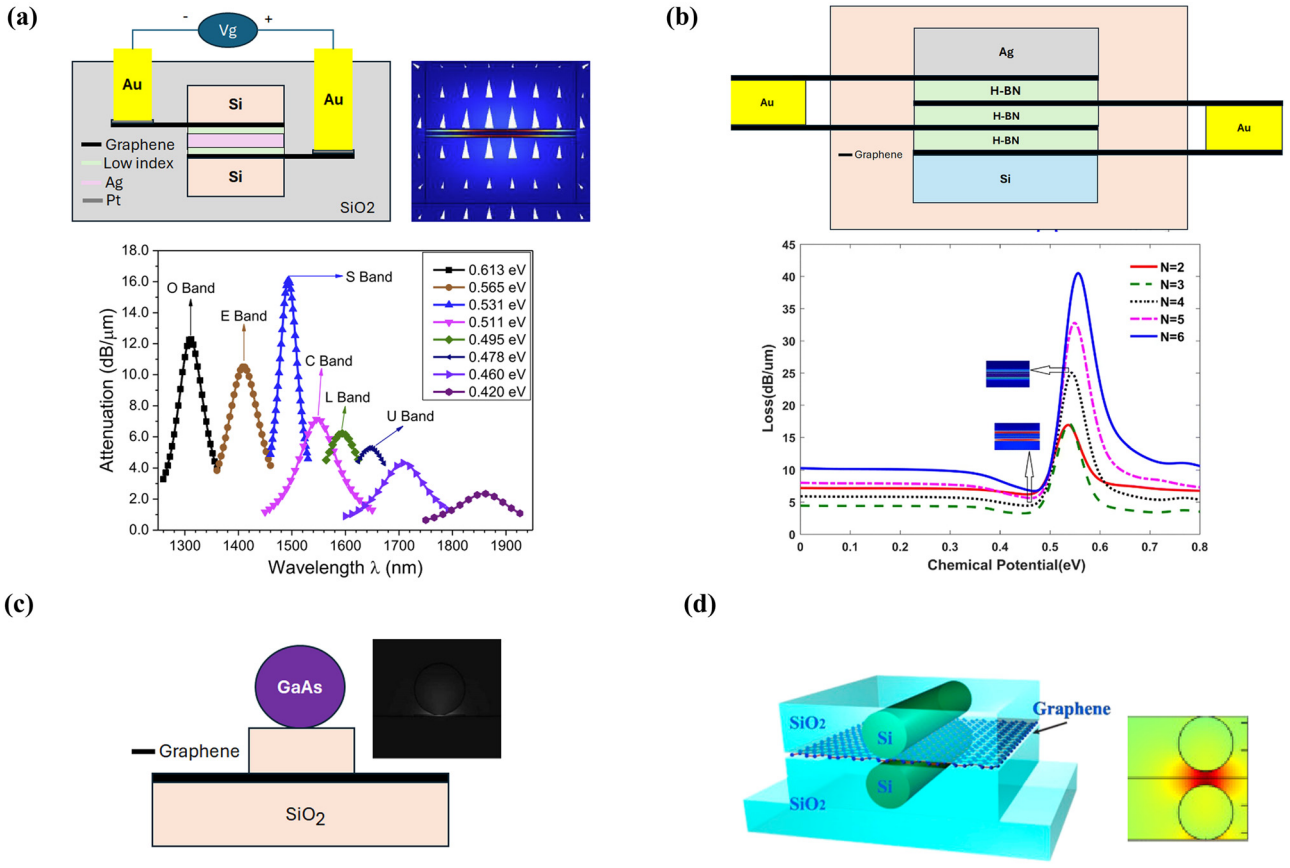

Figure 14: Various graphene-based HPW structures and their performance characteristics. (a) 2D cross-sectional view of graphene-based long-range HPW and its electric field (E_y) distribution for the TM mode. The plot also illustrates the attenuation spectra under different chemical potentials of graphene, with SiO_2 as the low-index slot material. Reproduced with permission from the study by Hu and Wang [192], © IEEE. (b) 2D schematic view of a multilayer graphene-based HPW and its electric field distribution. The graph analyzes the impact of the number of graphene layers on propagation loss as a function of graphene chemical potential. Reproduced with permission from the study by Vahed and Ahmadi [193], © Springer Nature. (c) 2D cross-sectional view of graphene-based HPW with an active cylindrical top layer, showing its electric field distribution. Reproduced with permission from the study by He *et al.* [194], © Optica Publishing Group. (d) 3D schematic view of the symmetrical graphene-based HPW along with the corresponding electric field distribution. Reproduced with permission from the study by Chen *et al.* [195], © Elsevier.

4 Applications of HPWs

HPWs have a wide range of applications due to their unique ability to confine light below the diffraction limit while maintaining long propagation lengths. As shown in Figure 15, these properties make HPWs suitable for various fields, including telecommunications, sensing, and photonics. In data transmission and telecommunications, HPWs are used in optical interconnects and systems due to their small footprint and ability to confine light at subwavelength scales. This results in significant improvements in data transmission capacity and speed, making HPWs ideal for ultra-high-speed telecommunication systems [199–204]. Additionally, HPWs are widely used in nanoscale sensing applications, where their ability to confine light and enhance light-matter interaction makes them ideal for detecting small changes in the refractive index or the presence of molecules, thus enabling highly sensitive biological and chemical sensors [3–8].

In bio-imaging, HPWs allow for imaging biological specimens at resolutions far beyond the diffraction limit of light, making them invaluable in nano-biophotonics [205]. In the fields of photovoltaics and light emission, HPWs enhance light-matter interactions, leading to improved absorption efficiency in solar cells and increased emission efficiency in light-emitting diodes (LEDs) [206]. Moreover, HPWs are utilized in nanoscale lasers, which benefit from tight light confinement and enhanced interactions, allowing for extremely small mode volumes and low thresholds [207]. On-chip optical circuits also benefit from HPWs, enabling the creation of compact and highly integrated optical components such as waveguides, modulators, and switches for

optical processing on chips [208]. Additionally, HPWs play a role in near-field optical tweezers, where their high field confinement and enhancement generate strong optical forces, making them effective in manipulating nanoparticles, molecules, and biological cells [115]. Finally, HPWs are applied in plasmonic hot-electron devices, which take advantage of the hot electrons generated by the nonradiative decay of SPs, with applications in photodetection, photocatalysis, and photovoltaics [209].

Remember, the specific design and the structure of HPW can impact its suitability for different applications. Different applications may require different trade-offs between factors like light confinement, propagation length, loss, and fabrication complexity. For a more comprehensive understanding of the performance and application of HPWs, it is crucial to delve into the details of several significant simulated and fabricated devices. This approach facilitates a closer look into how HPWs are leveraged in practical contexts. Here, we will discuss key examples from different domains, highlighting how HPWs are utilized in their operations.

4.1 HPW polarization beam splitter (PBS)

HPWs are highly effective in enhancing the functionality of PBSs due to their unique properties. PBSs work by separating incoming light into two orthogonal polarization states, and HPWs are adept at this task because of their polarization-dependent behavior. The superiority of HPWs in designing PBSs can be more clearly understood by looking at the limitations of alternative technologies. Traditional dielectric waveguides, for instance, often face challenges such as high losses when handling high index contrast and tight bends, which significantly reduce efficiency. In addition, their larger physical sizes limit the overall device density in PICs. In contrast, HPWs provide tighter light confinement in a subwavelength region, allowing for device miniaturization and reduced losses. Conventional plasmonic waveguides, although capable of strong light confinement, suffer from high propagation losses due to metal absorption. HPWs address this issue by striking a balance between metal-induced losses and dielectric-induced mode confinement, offering a more optimized solution. Similarly, SOI technology, while being well established for PICs, presents limitations related to its fabrication process. These include challenges with high-temperature processing, thermal expansion issues, and difficulties in integrating with other materials. HPWs, in contrast, can be fabricated through more flexible methods and offer better compatibility with various components, making them a preferred choice for integration.

Therefore, considering high field confinement, adequate propagation length, low loss, device miniaturization, and fabrication versatility, HPWs emerge as a leading technology for designing efficient PBSs. The principle of HPWs can be employed to realize an array of polarization control devices. This includes TE-pass and TM-pass polarizers, polarization rotators, and polarization splitters. These devices benefit from the unique characteristics of HPWs, such as their exceptional field confinement and their ability to support different polarization states, thereby offering distinct propagation constants for TE and TM modes. The ability to manipulate these propagation constants allows the design of sophisticated polarization control devices, thus enhancing the potential applications of HPWs in PICs and optoelectronic systems.

Polarization splitting can be primarily achieved through two approaches: adiabatic mode evolution and mode coupling. Adiabatic designs often necessitate a substantial device footprint due to restrictions imposed by adiabatic operations. For instance, a design reported by Watts *et al.* used a 200 mm long device to achieve an extinction ratio of 22 dB [210]. On the other hand, mode coupling-based devices can be significantly smaller, with coupling length in the micrometer range.

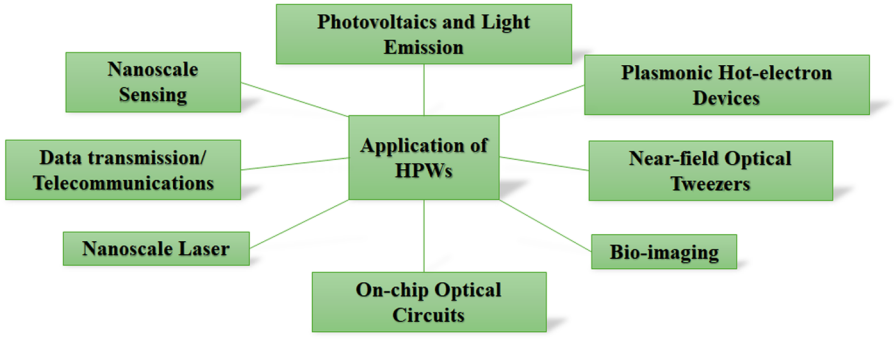

Figure 15: Applications of HPWs. HPWs enable a range of advanced applications due to their ability to confine light at subwavelength scales while maintaining low loss.

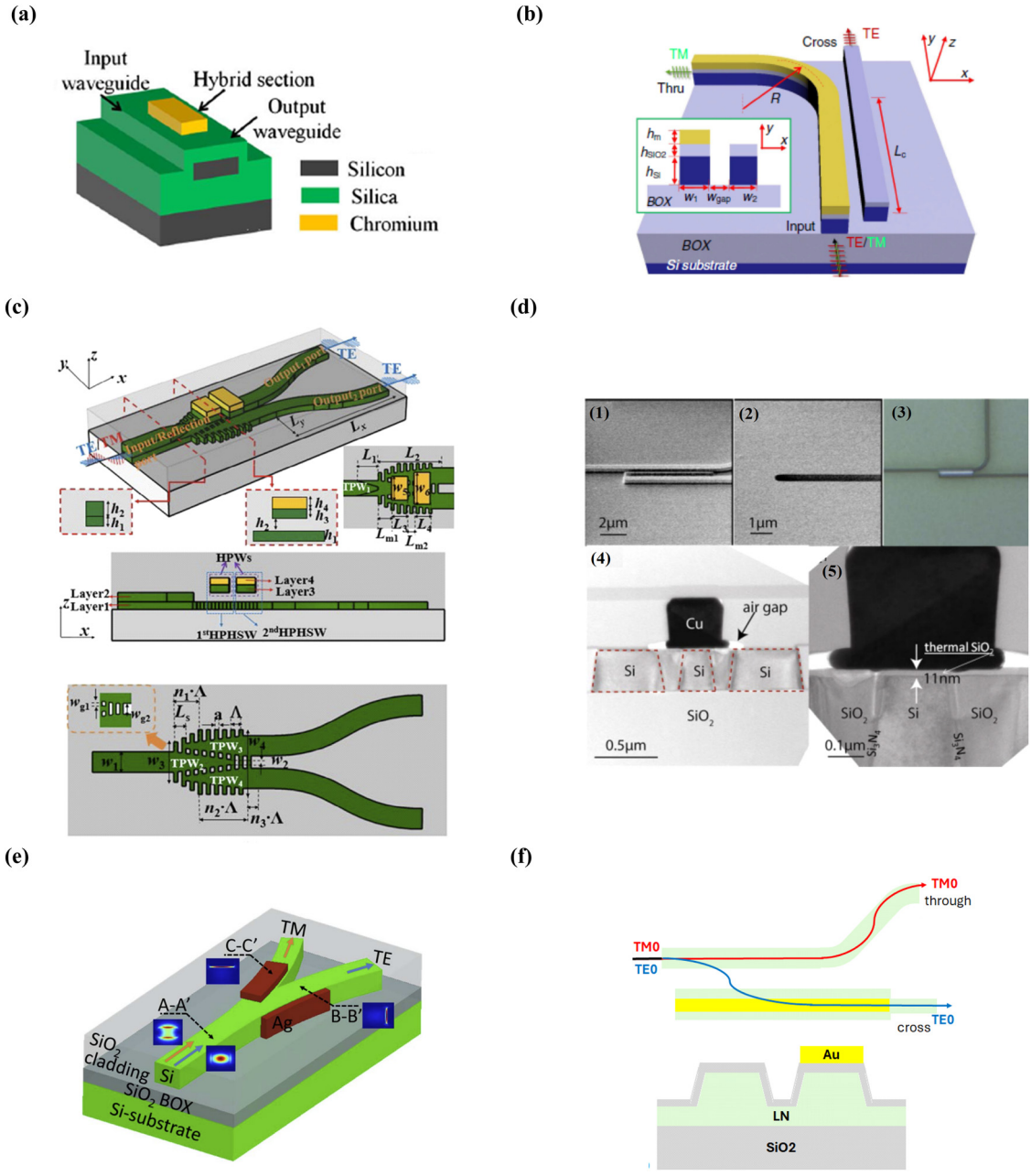

Figure 16: Various imaging and schematic illustrations of splitter structures: (a) HPW TE-pass polarizer. Reproduced with permission from the study by Sun *et al.* [212], © Optica Publishing Group. (b) PBS as well as its cross section based on an asymmetric directional coupler. Reproduced with permission from the study by Guan *et al.* [213], © Optica Publishing Group. (c) Ultra-compact TE-mode-pass power splitter. Reproduced with permission from the study by Lu *et al.* [214], © Elsevier. (d) Detailed imaging of the splitter and waveguide features: (1) scanning electron microscopy (SEM) showing Si waveguide cores prior to oxide and copper deposition. (2) SEM revealing the window that has been created to expose the central waveguide core. (3) Optical micrograph of a splitter highlighting a device with a pronounced 3 μm radius bend postwaveguide. (4) Cross section transmission electron microscopy (XTEM) of the coupling region of the manufactured splitter, with overlaid representations of the Si waveguide and Cu cap structure. (5) Zoomed-in XTEM near the hybrid waveguide area. Reproduced with permission from the study by Chee *et al.* [218], © Optica Publishing Group. (e) 3D scheme of HPW PBS with unnecessary phase-matching in comparison to PBS with directional coupler configuration. Reproduced with permission from the study by Hu *et al.* [220],© IEEE. (f) 2D cross-sectional view of the LN-based HPW PBS. Adapted with permission from the study by Li *et al.* [232], © Elsevier.

However, these designs usually have smaller bandwidths and require more precise fabrication tolerances. Given these trade-offs, mode coupling-based designs are typically preferred due to their compactness and integration-friendly characteristics, factors that are particularly applicable in the context of HPW polarization splitter [211].

The shortest TE-mode PBS, based on HPW concept, has been proposed experimentally by Sun *et al.* This work signifies a remarkable achievement in the field due to the device compact size and efficient performance (Figure 16(a)) [212]. For a compact polarizer with a length of just 30 μm, the reported extinction ratio ranges from 23 to 28 dB. In additionally, the insertion loss for the TE mode is maintained at a low value of 2–3 dB. Guan *et al.*, leveraging the concept of evanescent coupling between an HPW and a silicon nanowire, have proposed an innovative PBS, as depicted in Figure 16(b). By manipulating the waveguide width, the phase-matching condition is achieved exclusively for TE polarization, while significant phase mismatch is introduced for TM polarization. The resulting design of the PBS offers a remarkably small footprint, measuring around 1.9 × 3.7 μm^2. In addition, this design features a broad bandwidth of about 120 nm, an extinction ratio greater than 12 dB, and a significant tolerance in fabrication, allowing for a variation in a waveguide width of ±30 nm [213].

As shown in Figure 16(c), to achieve an ultra-compact TE-pass polarizer with a length of only 2.7 μm, a combination of subwavelength grating (SWG) and HPW has been utilized [214]. For the input TE mode, it can be uniformly split due to the enhanced coupling efficiency of the SWG coupler. The TM mode is converted into the eigenmodes of the segmented HPWs and is subsequently radiated into the silica claddings by the end facet of each HPW and absorbed by adjacent metals. This prevents the TM mode from launching efficiently. The efficiency is owed to the improved mode coupling of the TE mode by the SWGs in the coupling region and the large metal absorption and mode radiation of the TM mode by segmented HPWs. An insertion loss of 0.64 dB and a high extinction ratio of 20.56 dB have been achieved. In addition, return losses of TE and TM modes are 26.60 and 23.16 dB, respectively, at 1,550 nm. In the context of HPWs, the TE mode typically remains stable when the spacer layer is significantly thick. Yet, this stability alters dramatically as the spacer layer thickness decreases.

At optical wavelengths, noble metals like gold and silver can still be regarded as good conductors due to their large negative permittivity. This characteristic causes them to resist the presence of tangential electric fields on their surface. As a result, in the case of a thin spacer layer, the TE mode, characterized by a dominant tangential electric field, is extruded from the core, reaching a cutoff. Exploiting this characteristic, a TM-pass polarizer design has been introduced, demonstrating an extinction ratio of 21.8 dB and an insertion loss of 3.2 dB [215].

An asymmetric TM-pass polarizer, which is based on a cylindrical silicon nanowire HPW, has been detailed in previous studies [216,217]. However, the fabrication of such a cylindrical structure using planar lightwave circuit technology presents certain challenges. Addressing this challenge, as illustrated in Figure 16(d), Chee *et al.* have fabricated a TM-pass polarizer, which integrates an HPW as the central waveguide in a three-core setup on an SOI platform. This configuration effectively achieves large birefringence, resulting in an extinction ratio exceeding 15 dB, with an insertion loss of less than 0.5 dB [218].

A PBS with a compact footprint of 1.8 × 2.5 μm^2 has been developed utilizing an HPW and a multimode interference (MMI) coupler. The MMI section, partially covered with a metal strip, has been designed to achieve mirror imaging specifically for TE polarization. Conversely, for TM polarization, the MMI effect is largely absent because higher-order TM modes have been scarcely excited due to the hybrid plasmonic effect [219].

Moreover, a hybrid plasmonic Y-branch (HPYB) structure of Figure 16(e) represents a significant advancement in the design of PBSs due to its simplified architecture and exceptional performance [220]. This structure offers a breakthrough in achieving ultra-large bandwidth and compact size, making it highly suitable for next-generation PICs. Unlike conventional designs that rely on complex phase-matching conditions or SPPs to couple modes, the HPYB directly excites vertical and horizontal hybrid modes from the input TE and TM modes, enabling efficient splitting into separate ports. This approach not only streamlines the device complexity but also results in an impressive bandwidth of 285 nm, far exceeding many of the PBSs reported in previous studies [213,221–229]. Moreover, the elimination of phase-matching requirement, as seen in HPW directional couplers [213,229], reduces design constraints, offering greater flexibility and fabrication tolerance with waveguide width variations of up to 210 nm. In addition, this PBS combines compactness with low insertion loss, positioning it as a strong candidate for high-performance photonic applications despite a slightly higher insertion loss compared to some designs.

Polarization rotators are crucial for on-chip polarization control, as they allow the orientation of the polarization plane of light to be adjusted, which is critical for the function of many integrated photonic devices. Most designs for polarization rotators currently reported are primarily based on either mode interference or adiabatic mode evolution. Mode interference involves controlling the phase and amplitude of different polarization modes to achieve

rotation. This method allows for the creation of compact devices, but they often require precise fabrication and are typically limited in bandwidth. Adiabatic mode evolution, on the other hand, relies on a slow, gradual change in the waveguide properties to transfer light from one polarization state to another. This method usually yields devices that are highly tolerant to fabrication variations and offer large operational bandwidths, but they tend to require a larger footprint [230].

HPWs can significantly improve the performance of polarization rotators due to their ability to support both TE and TM modes and facilitate their coupling, which is a critical aspect of polarization rotation [230,231]. The confinement of light within the HPW subwavelength scale also enables high levels of control over the propagation characteristics of the light, which can be beneficial for the design of compact and efficient polarization rotators. In the study by Abu-Elmaaty and Shalaby [231], a practical application of HPWs in the design of polarization rotator has been demonstrated. In this study, the researchers have proposed a novel design for a polarization rotator that uses an HPW to induce a phase shift between TE and TM modes of the light, resulting in a rotation of the polarization plane. The design shows a polarization conversion efficiency of greater than 90% over a broad bandwidth. The proposed HPW-based polarization rotator is not only efficient and broadband but also has a small footprint, making it ideal for integration into compact photonic circuits. Furthermore, the study shows that the device has a high tolerance to fabrication variations.

Most of these PBS designs have been implemented on the SOI platform. However, with recent advancements in crystal ion slicing techniques for thin film fabrication, it is now feasible to construct high-performance PBSs on the lithium niobate on insulator (LNOI) platform [232]. Lithium niobate (LN) is a highly favored optical material due to its superior properties including significant electro-optic response, large nonlinear coefficient, and broad transparency window. LNOI, compared to traditional LN waveguides, produced by titanium diffusion or proton exchange, offers higher refractive index contrast, superior subwavelength light confinement, and a more compact device size. In addition, the LNOI platform is compatible with the CMOS fabrication process, making it an attractive candidate for realizing compact PICs. Despite these advantages, LNOI intrinsic anisotropy and geometric birefringence introduce polarization sensitivity, which is a significant challenge. A polarization diversity system has been proposed as a solution to this issue. In such systems, the PBS plays a fundamental role in separating and combining TE and TM polarizations [232].

Some PBSs based on the LNOI platform have been compared in terms of polarization extinction ratio (PER), insertion loss, bandwidth, device length, and crystallographic cut, which show the superiority of the combination of LN with HPW technology. For z-cut devices, PER values for the TE and TM modes vary from 21.3 to 31 dB, with insertion losses ranging between 0.05 and 1.0 dB. These devices exhibit bandwidths up to 185 nm for TE and 85 nm for TM polarizations, with lengths from 16 to 160 μm [233,234]. Other studies, such as by Xu *et al.* [235], report a significantly higher PER of up to 48 dB for both TE and TM modes in x-cut configurations, but with greater insertion losses, particularly reaching 0.9 dB for TE modes. Furthermore, bandwidths over 200 nm are achievable with longer device lengths exceeding 430 μm, although some devices reach 6 mm [236].

As shown in Figure 16(f), Li *et al.* have implemented an asymmetric directional coupler consisting of a single-mode waveguide and HPW, achieving one of the shortest PBS on the x-cut LNOI platform with a total device length of only 47 μm. The compactness of this design was enabled by the polarization-sensitive nature of plasmonic phenomena. The device demonstrates impressive performance, achieving a bandwidth of at least 200 nm with −10 dB extinction for TE polarization and at least 200 nm with less than −20 dB extinction for TM polarization [232].

Table 3 presents a comprehensive summary of the most important various types of HPW-based PBSs and polarization rotators that have been proposed to date.

4.2 HPW-fed nanoantenna

The importance of designing HPW-fed nanoantennas lies in their ability to bridge the gap between nanoscale photonic devices and larger, macroscopic waveguide structures. These structures take advantage of the benefits provided by both nanoantennas and HPWs. Nanoantennas, much like their radio-frequency counterparts, help in directing, capturing, and enhancing electromagnetic radiation at nanoscale dimensions. They are particularly useful at optical frequencies, helping to overcome the diffraction limit of light and enabling highly localized light concentration. HPWs, on the other hand, provide a mechanism to guide light along a desired path with reduced propagation loss and subwavelength confinement. When combined, HPW-fed nanoantennas offer the potential for directed and enhanced light-matter interactions at the nanoscale, making them valuable for a wide range of applications. In light emission, these structures can be used to direct and enhance emissions from quantum emitters, such as quantum dots or single-photon sources, which is particularly

Table 3: The characteristics of different HPW-based devices

HPW-based PBSs						
Applications			**Advantages**		**Limitations**	
Optical communications, photonic circuit			**High polarization discrimination, compact size**		**Limited to specific polarization states**	
Ref.	**Footprint (μm^2)**	**Waveguide type**	**Bandwidth (nm)**	**Coupling length (μm)**	**Output power (%)**	**Polarization performance**
[72]	2.38 × 10	HPSW[a)]	10	5.44	96.02 (TE), 99.37 (TM)	TM_0/TE_1-to-TE_1/TM_0
[104]	900 × 15	CaV_3-HPW	100	15	99.99	TM_0/TE_1-to-TE_1
[210]	N[b)] × 200	High-index-HPW	30	200	99.36	TE_{11}/TM_{11}-to TE_{21}/TM_{21}
[208]	2.9 × 4.45	HPW	303	2.25	95	TM_0/TE_1-to-TE_1/TM_0
[208]	2.9 × 4.45	HPW-graphene	303	2.25	25	TM_0/TE_1-to-TE_1/TM_0
[213]	3.7 × 1.9	HPW	120	2.2	95	TM_0/TE_1-to-TE_1/TM_0
[216]	—	DW-graphene[c)]	74	8.3	27.55	TM_0/TE_1-to-TE_1/TM_0
[217]	—	MHPW	300	6.8	100 (TE), >90 (TM)	TM_0/TE_1-to-TE_1/TM_0
[218]	—	Cu-HPW	300	6.5	52.8 (TE), 75.94 (TM)	TM_0/TE_1-to-TE_1/TM_0
[219]	1.8 × 2.5	MMI-HPW[d)]	80	1.1	100	TM_0/TE_1-to-TE_1/TM_0
[221]	—	ASHPW	40	200	—	TM_0/TE_1-to-TE_1/TM_0
[232]	N × 47	LNOI-HPW	200	32	90 (TE), 99 (TM)	TM_0/TE_1-to-TE_1/TM_0
[243]	—	Nanoparticle-HPW	—	3.8 (TM), 4.2 (TM)	75 (TE), 100 (TM)	TM_0/TE_1-to-TE_1/TM_0
[266]	—	HPW	70	7.7	95	TM_0/TE_1-to-TE_1/TM_0
[267]	2.6 × 8.1	HPW	100	2.42	95.49	TM_0/TE_1-to-TE_1/TM_0
[268]	2 × 5.1	DW-HPW	20	3.5	41.25	TM_0/TE_1-to-TE_1/TM_0
[269]	—	HPW	100 (TE), 64 (TM)	6.1	98 (TE), 96 (TM)	TM_0/TE_1-to-TE_1/TM_0
[270]	0.920.92	Combined-HPW	400	0.920	79.1	TM_0/TE_1-to-TE_1/TM_0
[271]	*N* × 5	HPW	100	5	99	TM_0/TE_1-to-TE_1/TM_0
[272]	—	InP-HPW	100	650 (TE), 60 (TM)	95 (TE), 70 (TM)	TM_0/TE_1-to-TE_1/TM_0

[a)] HPSW, hybrid plasmonic slot waveguide; [b)] Not mentioned; [c)] DW-graphene, dielectric waveguide-graphene; [d)] MMI-HPW, multimode interference-HPW.

HPW polarization rotators				
Applications			**Advantages**	**Limitations**
Integrated photonic systems, optical devices			**Compact, efficient polarization conversion**	**Alignment precision required**
Ref.	**Bandwidth (nm)**	**Total length (μm)**	**Insertion loss (dB)**	**Extinction ratio (dB)**
[70]	—	5	2.1	>14
[230]	40	4.5	3.6	>11
[231]	—	12.5	1.19	21
[241]	500	5	1.94	—

HPW-fed nanoantennas						
Applications			**Advantages**		**Limitations**	
Nano-optics, sensing, energy harvesting			**High field confinement, strong near-field enhancement**		**Narrow bandwidth, sensitive to fabrication**	
Ref.	**Topology**	**Bandwidth (THz)**	**Gain/directivity (850 nm)**	**Gain/directivity (1,310 nm)**	**Gain/directivity (1,550 nm)**	**Footprint (nm^2)**
[51]	Coupled HPW	250	10.5/11	9.05/9.35	9.39/9.7	1,000 × 850
[125]	SHPW	20	—	—	9.34/7.01	1,400 × 900
[132]	CHPW	20	—	—	9.03/9.38	1,200 × 950
[199]	Typical RHPW	15	—	—	5.6/6	700 × 700
[200]	MIM RHPW	40	—	—	8.3/8.4	1,100 × 800

(Continued)

Table 3: *Continued*

HPW-fed nanoantennas						
Applications			**Advantages**		**Limitations**	
Nano-optics, sensing, energy harvesting			**High field confinement, strong near-field enhancement**		**Narrow bandwidth, sensitive to fabrication**	
Ref.	**Topology**	**Bandwidth (THz)**	**Gain/directivity (850 nm)**	**Gain/directivity (1,310 nm)**	**Gain/directivity (1,550 nm)**	**Footprint (nm^2)**
[201]	Typical RHPW	250	2.06/N	4.6/N	5/N	800 × 800
[202]	Typical InP RHPW	40	—	—	8.97/9.27	1,100 × 800
[203]	Typical InP RHPW	50	—	7.84/7.96	10/10.72	1,000 × 900
[204]	Typical RHPW	<250	4.8/N	7.3/N	4.7/N	1,100 × 800
[208]	Typical RHPW	40	—	—	10.3/10.5	1,560 × 1,600
[237]	Quantum Well VHPW	40	—	—	10.6/11.8	1,350 × 1,600

HPW directional couplers				
Applications		**Advantages**		**Limitations**
Optical switching, signal processing		**High coupling efficiency, compact size**		**Limited range of coupling control**
Ref.	**Topology**	**Bandwidth (nm)/ wavelength (nm)**	**Coupling length (μm)**	**Coupling efficiency (%)**
[47]	RHPW	200/1,550	0.4	70
[73]	RHPW	64/1,550	4.25	86.4 (TE), 94.6 (TM)
[219]	MMI-HPW	80/1,550	1.1	—
[238]	SG-HPW[a)]	270/1,550	16.48	>50
[241]	RHPW	500/1,550	5	>64
[246]	GHPW[b)]	73/1,550	—	79
[247]	InP-HPW	300/1,550	2	86
[248]	CHPW	*N*/1,550	1.646	80
[273]	CHPW	*N*/980	1.9	60
[274]	RHPW	*N*/1,550	4.8	100
[275]	MHPW	40/1,550	8.9	>50
[276]	VHPW	*N*/1,550	0.492	>97
[277]	CHPW	*N*/1,550	2.488	95
[278]	DW-HPW	*N*/1,550	4.5	73

[a)] SG-HPW, strip grating HPW; [b)] GHPW, grating HPW.

HPW power splitters				
Applications		**Advantages**		**Limitations**
Optical networks, signal distribution		**Efficient signal distribution, broadband operation**		**Insertion loss increases with complexity**
Ref.	**Topology**	**Footprint ($μm^2$)**	**Output power (%)**	**Controllability**
[44]	1 × 4 RHPW	—	91, 91	No
[44]	1 × 4 RHPW	1.9 × 2.6	25.6, 24.3, 25.6, 24.5	No
[98]	1 × 2 RHPW	—	82.1, 78.3	No
[98]	1 × 3 RHPW	—	76.1, 76.1, 75.5	
[214]	1 × 2 Grating-HPW	− × 2.7	>50, >50	No
[208]	1 × 3 Graphene-HPW	2.4 × 2.8	30.52, 29.91, 29.91	Yes-Graphene HPW
[249]	1 × 5 Graphene-HPW	>5 × 3.8	83	Yes-Graphene HPW
[279]	1 × 2 ASHPW	1 × 1.1–1.5	50, 50/100, 0	No
[280]	2 × 2 MMI- InP-HPW	1 × 2	79.82, 9.98	No

(Continued)

HPW optical forces (slot HPW and HPW ring resonator (HPW RR))

Applications (slot HPW)			Advantages		Limitations
Optical sensing, nonlinear optics			Strong field confinement, high nonlinearity		High propagation loss due to confinement
Applications (HPW RR)			**Advantages**		**Limitations**
Biosensing, filtering, WDM			High sensitivity, compact size		Sensitive to fabrication imperfections
Ref.	**Topology**	**Type of sensor**	**Sensitivity/FOM/Q factor**	**MRR radius (μm)**	**Propagation loss (dB/μm)**
[43]	Cu-TiO_2-Si VHPW	Thermo-sensor	52 (pm/°C)/N/140	1.2–2.5	0.2
[50]	Composite SHPW	Thermo-sensor	0.052 (nm/°C)/N/6507	2.5	0.03
[58]	Au–SiO_2–SU-8 polymer HPW	—	N/255/150	15	0.0476
[184]	DDMEBT nonlinear HPW	Not logic gate	N/130.36 (W^{-1})/132,250	1	0.01
[208]	HSQ HPW	Bio-sensor	133 (nmRIU^{-1})/26.61 (RIU^{-1})/N	0.270	0.046
[208]	$In_{0.53}$ $Al_{0.1}$ $Ga_{0.37}$ As HPW	Thermo-sensor	0.05 (nm/K)/N/N	0.270	0.046
[253]	CSSHPW	Bio-sensor	511.5 (nmRIU^{-1})/21,176 (RIU^{-1})/64,174	2	0.08
[255]	SWG racetrack HPW	Bio-sensor	477.7 (nmRIU^{-1})/N/346.5	10	—
[256]	Racetrack HPW				
[281]	Slot HPW	Bio-sensor	555 (nmRIU^{-1})/154.16 (RIU^{-1})/N	5	—
[282]	Si–Au–SiO_2 HPW	Bio-sensor	238 (nmRIU^{-1})/N/392.8	3	—
[283]	SSHP[a)]	Bio-sensor	458.1 (nmRIU^{-1})/27,009 (RIU^{-1})/91,354	1	0.08

[a)] SSHP, suspended slot hybrid plasmonic.

beneficial in quantum information processing and improving the efficiency of LEDs. In addition, HPW-fed nanoantennas can greatly increase the field intensity near the nanoantenna, making them ideal for sensitive detection of biological and chemical species. This sensitivity positions them for use in medical diagnostics, environmental monitoring, and security applications. Furthermore, they hold potential in photovoltaics, where they could enhance light absorption in thin-film solar cells, thus improving overall efficiency.

Despite their promising applications, the design and implementation of HPW-fed nanoantennas present several challenges. Fabrication at the nanoscale requires highly advanced lithographic techniques, which are complex and prone to imperfections that can affect performance. The materials used in these structures also pose limitations; for optical frequencies, the availability of materials with suitable plasmonic properties is restricted. Moreover, concentrating light at the nanoscale can lead to significant local heating, which may degrade both the performance and long-term reliability of the devices. Finally, the small size and complex light interactions with these structures make accurate simulation and design computationally intensive, adding further complexity to their development.

Despite these challenges, the unique capabilities of HPW-fed nanoantennas make them a promising area of research for a variety of applications.

HPW-fed nanoantennas are capable of controlling far-field characteristics to receive in-plane electromagnetic waves and radiate them into free space (or vice versa). By proposing varying structures based on diverse types of HPWs, these antennas can offer a horizontal radiation pattern with maximum efficiency, making them ideal for integration with other elements in PICs. An HPW-fed nanoantenna comprises two major components: HPW and hybrid plasmonic radiation part. The HPW, acting as a feed line, is essential for confining and transmitting the excited TM fundamental mode through the low-index layer to the radiation part. In subsequent sections, we explore various HPW-fed nanoantennas, examining their advantages and limitations.

The initial HPW-fed patch nanoantenna was put forth by Yousefi and Foster [199], as shown in Figure 17(a). This structure comprises a Si–SiO_2 substrate, topped with a three-layered arrangement including a 200 nm Si layer, a 10 nm SiO_2 layer, and a 100 nm silver layer. Efficiently operating at the wavelength of 1,550 nm, this nanoantenna achieves a gain of 5.65 dB and an efficiency of 87%. However, its bidirectional radiation pattern is not ideal for on-chip applications due to the radiation emanating from the substrate. This can potentially interfere with the performance of PICs when the nanoantenna is integrated with other devices. Addressing this issue, a hybrid MIM patch

nanoantenna has been proposed [200], featuring a silver slab situated atop the SiO_2 substrate, as depicted in Figure 17(b). This design absorbs radiation emitted from the substrate, thereby facilitating a vertical unidirectional radiation pattern. The antenna exhibits superior gain, bandwidth, and efficiency of 8.32 dB, 24.38 THz, and 96%, respectively, at 1,550 nm. As a result, it becomes suitable for on-chip wireless links between different PICs stacked atop one another.

Saad-Bin-Alam *et al.* have introduced an innovative design aimed at broadening the bandwidth of the proposed patch nanoantenna to nearly 250 THz. The new design involved a broadband Vivaldi hybrid plasmonic nanoantenna. As shown in Figure 17(c), while it shared the same HPW configuration with the structures proposed by Yousefi, it presented a different radiation section [201]. The Vivaldi nanoantenna has been designed to effectively radiate the excited TM fundamental mode into free space. It boasted a substantial fractional bandwidth of 86%, along with the peak gains of 2.06, 4.64, and 5.03 dB at the wavelengths of 850, 1,310, and 1,550 nm, respectively. However, the nanoantenna performance at 1,550 nm is similar to that of Yousefi's design, and the low gain at this wavelength could limit its capability for long-range wireless data transmission.

Khodadadi *et al.* have introduced a novel design for a wideband HPW-fed nanoantenna, capable of delivering an impressive bandwidth of 250 THz, high realized gain and efficiency, ultra-long range SPPs, and a horizontal unidirectional radiation pattern. This is achieved by employing a unique design featuring two coupled parallel SiN_x HPWs and a V-shaped radiation part, as demonstrated in Figure 17(d) [51]. However, a significant challenge to the implementation of this design is the high aspect ratio required for its fabrication. The exploration of a ±5% fabrication error on the structural parameters showed that the most sensitive parameter is the angle between two branches of the radiation part, with a maximum error of 4%. This angle plays a crucial role as it regulates the coupling of the SPPs emitted from each branch, thereby determining the desired radiation pattern. Any variation in this angle could significantly affect the radiation pattern and performance of the antenna.

For the first time, Nikoufard *et al.* have proposed the concept of integrating active materials such as InP and InGaAsP into the design of HPW-fed nanoantennas [202]. This idea originates from the challenge of integrating monolithically the SOI- and polymer-based hybrid plasmonic devices with active elements of PICs like lasers and photodetectors. An InP-based laser can be smoothly connected to passive hybrid plasmonic devices such as HPW, HPW-based nanoantennas, and hybrid plasmonic tapers using the butt-joint technology [202]. To illustrate the advantages of nanoantennas with active materials, a bow-tie nanoantenna has been introduced, as shown in Figure 17(e). This innovation signifies a breakthrough in the integration of hybrid plasmonic devices with PICs, thereby enhancing their performance and functionality. Adding to this, Khodadadi *et al.* have further innovated the design of active HPW-fed nanoantennas by introducing a new director, which results in significant improvements in both bandwidth and efficiency [203].

In a ground-breaking approach, a novel concept of a complementary SHPW-fed nanoantenna has been proposed, as illustrated in Figure 17(f) [125]. Within a SHPW, the interplay of constructive and destructive interactions between excited SPPs in both low-index layers produces long-range and short-range TM super-modes, each with distinct radiation patterns. The long-range excited TM super-mode facilitates a unidirectional pattern with an impressive directivity of 9.34 dBi and efficiency of 96.82%. Conversely, the short-range super-mode yields a directivity of 7.01 dBi but suffers from a lower efficiency of 9.66%, attributed to the destructive interaction between the coupled modes in the low-index layers.

The oxidation of aluminum (Al) in HPW-based nanoantennas presents a challenge, as it can degrade antenna performance over time. To address this issue, several strategies can be employed to mitigate oxidation [125,208]. One common approach is the use of passivation layers, where a thin protective coating of a nonreactive material is applied to shield the Al from contact with air, thus preventing oxidation. Alternatively, in some applications, Al can be substituted with materials that are more resistant to oxidation, such as gold or silver, though the choice of material depends on the specific requirements of the application. Another method involves the application of antioxidants to slow down the oxidation process. This technique is often combined with other strategies for maximum protection. In addition, careful storage and handling procedures can minimize exposure to moisture, heat, or other conditions that accelerate oxidation. Finally, designers can account for a certain degree of oxidation in the design phase. Research shows that a 6 nm layer of aluminum oxide (Al_2O_3) has a minimal impact on the bandwidth and plasmonic behavior of nanoantennas, making Al_2O_3 a viable protective layer that effectively shields against oxidation without significantly altering performance characteristics [125].

In comparison to multiband horn nanoantenna, which has a maximum gain of 4.67 dB at 1,550 nm [204], a significantly more efficient design has been proposed. This

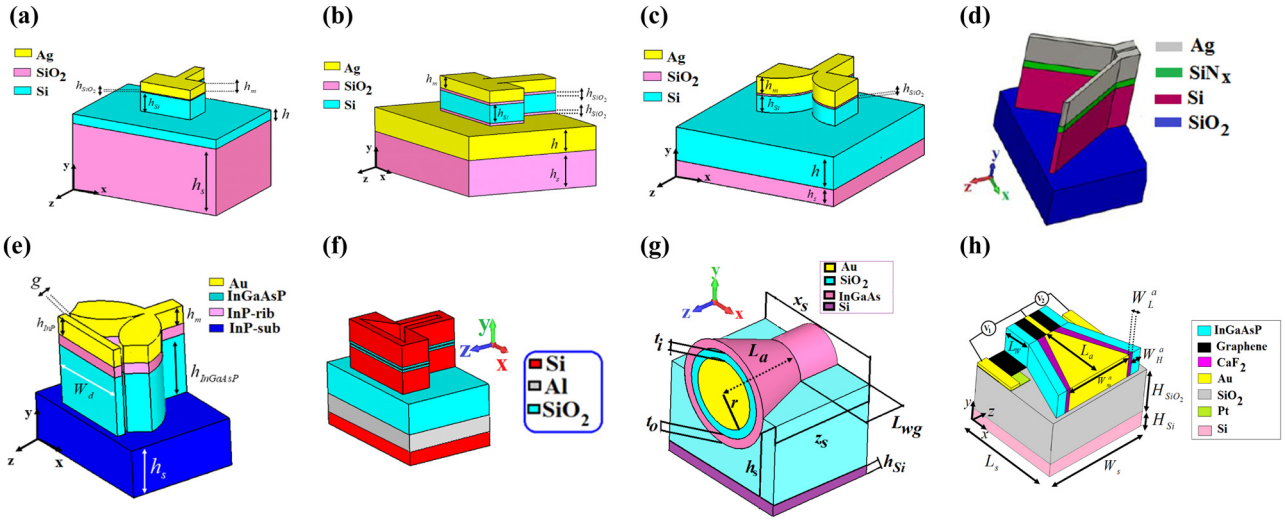

Figure 17: Schematic view of the HPW-fed nanoantennas. (a) Patch, (b) MIM patch, (c) Vivaldi, (d) V-shaped (adapted with permission from the study by Khodadadi *et al*. [51], © IOP Publishing), (e) bow-tie, (f) complementary SHPW (adapted with permission from the study by Khodadadi and Nozhat [125], © IEEE), (g) CHPW horn (reproduced with permission from the study by Khodadadi *et al.* [132], © Nature Publishing Group), and (h) graphene quantum well VHPW configurations (reproduced with permission from the study by Khodadadi *et al*. [237], © Elsevier).

model, a CHPW-fed horn nanoantenna, achieves a high gain of 9.03 dB, as shown in Figure 17(g) [132]. This design improvement results in a significant enhancement of nanoantenna performance. However, the fabrication of this specific structure presents considerable challenges. The complexities involved in its construction, along with the high precision required, make it difficult to produce on a large scale or with consistent results. It is crucial for further research and development to explore methodologies that can simplify and standardize the fabrication process. In addition, a pioneering approach for a smart multiuser wireless link has been proposed by Khodadadi *et al.*, as depicted in Figure 17(h). This concept leverages a nanoantenna fed by a graphene quantum well VHPW, opening new horizons for advanced nanoscale communication systems [237]. Leveraging multimode graphene quantum well VHPW has led to designing a selective mode nanoantenna. This nanoantenna features a unique ability to alternate between broadside and end-fire radiation patterns. The high directivities of 9.38 and 11.8 dBi, respectively, at the frequency of 193.5 THz have been achieved.

Table 3 provides a comprehensive summary of various types of HPW-fed nanoantennas that have been proposed to date. This overview facilitates the comparison of different designs based on their features, performances, and applications, helping researchers to navigate the broad range of existing designs and optimize their choices for specific applications.

4.3 HPW directional coupler and power splitter

Directional couplers and power splitters are essential components in PICs and optical communication systems. They are used to efficiently split or combine optical signals and route them to different paths or devices. The performance of these devices is crucial in achieving high signal fidelity, low insertion loss, and precise power distribution.

HPWs can significantly enhance the performance of directional couplers and power splitters through various mechanisms. First, HPWs enable efficient mode conversion between different waveguide modes, such as transitioning from a narrow strip waveguide to a wider HPW. This seamless mode conversion reduces mismatches and improves the overall transmission of light between different sections of the device. Second, HPWs provide strong field confinement within the low-index dielectric layer, allowing for precise spatial control of the optical signal, which improves power splitting and coupling efficiency. Moreover, HPWs support strong evanescent field interactions, leading to efficient power transfer between closely spaced waveguides. This enhances the performance of directional couplers by promoting high coupling efficiency and reducing insertion loss. Furthermore, HPWs offer enhanced control over light propagation, minimizing crosstalk between waveguide channels, which results in improved signal isolation. Finally, HPWs enable broadband operation, supporting multiple wavelength channels simultaneously,

which is particularly beneficial for applications like wavelength division multiplexing (WDM) systems.

In the rapidly evolving realm of HPW couplers, recent advancements have demonstrated that HPWs are bridging the traditionally perceived divide between photonics and plasmonics. Their unique ability to tap into the field confinement of plasmonics while retaining the low-loss attributes of traditional photonics has led to the emergence of novel coupler designs that promise compact footprint, efficient power transfer, and broadband operation. Directional hybrid plasmonic couplers, as highlighted by hypothetical works such as Xu and Sun [238], have underscored the advantage of broadband operation and efficient power transfer. While their size remains a point of contention, ongoing research is keenly focused on leveraging advancements in fabrication to miniaturize these structures without compromising their performance. Y-Junction couplers, often cited for their compact nature, are paving the way for PICs that require efficient on-chip signal splitting and routing. The promise they hold is overshadowed by concerns regarding insertion loss, but as fabrication techniques evolve, such as deep UV lithography, there is hope for even more refined and efficient designs in the future [239]. The beauty of adiabatic taper HPW couplers, as illustrated by researchers such as Shi *et al.*, lies in their low-loss transitions. Their application in high-signal integrity domains like quantum photonics is a testament to their importance. The challenge of their size remains, but with the continuous evolution of precision fabrication techniques, this concern is poised to be addressed [240]. Finally, mode converter hybrid plasmonic couplers present a revolutionary approach to interfacing different photonic components. By providing a platform for seamless mode conversion, they are breaking barriers in multimode system designs and high-capacity data transmission [241].

The work by Kim and Qi further illustrates this innovation through their mode-evolution-based polarization rotation and coupling structure, which adiabatically rotates the TE mode in a silicon waveguide and couples it to the hybrid plasmonic mode in a silicon-dielectric-metal waveguide (Figure 18(a)) [241]. Achieving a coupling factor as high as 92% with a sliver metal cap over a broad wavelength range of 1,300–1,800 nm, this design demonstrates how hybrid plasmonic couplers enable efficient, low-reflection mode transitions, thus contributing to enhanced performance in multimode photonic systems. These advancements underscore the potential of hybrid plasmonic technology in overcoming challenges related to mode conversion, enabling more robust, high-capacity optical communication systems. However, coupling losses present a significant bottleneck in the development of low-loss active HPW components. The primary difficulty arises from the mode mismatch between silicon photonic access waveguides, where modes are predominantly confined within the silicon core, and hybrid plasmonic structures, where modes are primarily confined in the insulating layer between the silicon and metal.

Previous works have proposed both butt-coupling [47,242] and evanescent coupling [243] as potential solutions, but many of these designs are difficult to fabricate. The hybrid plasmonic modulator described in [244] employs butt-coupling for photonic-to-plasmonic conversion with a loss of only 0.25 dB. However, the 800 nm-wide hybrid plasmonic section supports multiple modes, reducing the coupling efficiency to a single mode and causing mode beating between the silicon and insulating layers. While this may not significantly impact modulators based on electro-absorption, modulators relying on phase shifts due to a nonlinear material in the insulating layer could experience diminished efficiency due to the electric field periodically exiting the active region. Another example demonstrates butt-coupling to a 200 nm wide HPW, but the highest measured efficiency (−1 dB) falls short of the numerically predicted optimum (−0.55 dB), and the issue of multiple mode excitation persists [16]. To tackle this issue, as shown in Figure 18(b), a fabrication-tolerant directional coupling approach between a silicon photonic waveguide and an HPW, achieving an efficiency of 94% (−0.27 dB), has been introduced [245].

In addition, various methods have been proposed to achieve efficient coupling between dielectric waveguides and plasmonic or HPW. Song *et al.* [47] have introduced a hybrid plasmonic linear taper to improve the coupling efficiency between a silicon waveguide and an HPW. The HPW consists of an Al_2O_3 layer sandwiched between silver and silicon, as depicted in Figure 18(c). This compact plasmonic taper, with a length of just 0.4 μm, enables broadband coupling and achieves a coupling efficiency of 70% (1.5 dB) at 1,550 nm.

Besides increasing efficiency, direct coupling between a standard single-mode fiber and photonic or plasmonic components is essential for several other reasons. It ensures efficient light transfer, as single-mode fibers are widely used in optical communications due to their ability to maintain the integrity of light signals over long distances. Direct coupling not only increases efficiency by minimizing optical power losses, but it also addresses the issue of mode mismatch between fibers and target components, such as waveguides or hybrid plasmonic structures. This enhances the overall performance of the system by ensuring efficient mode conversion and reducing coupling losses. Moreover, direct coupling simplifies system

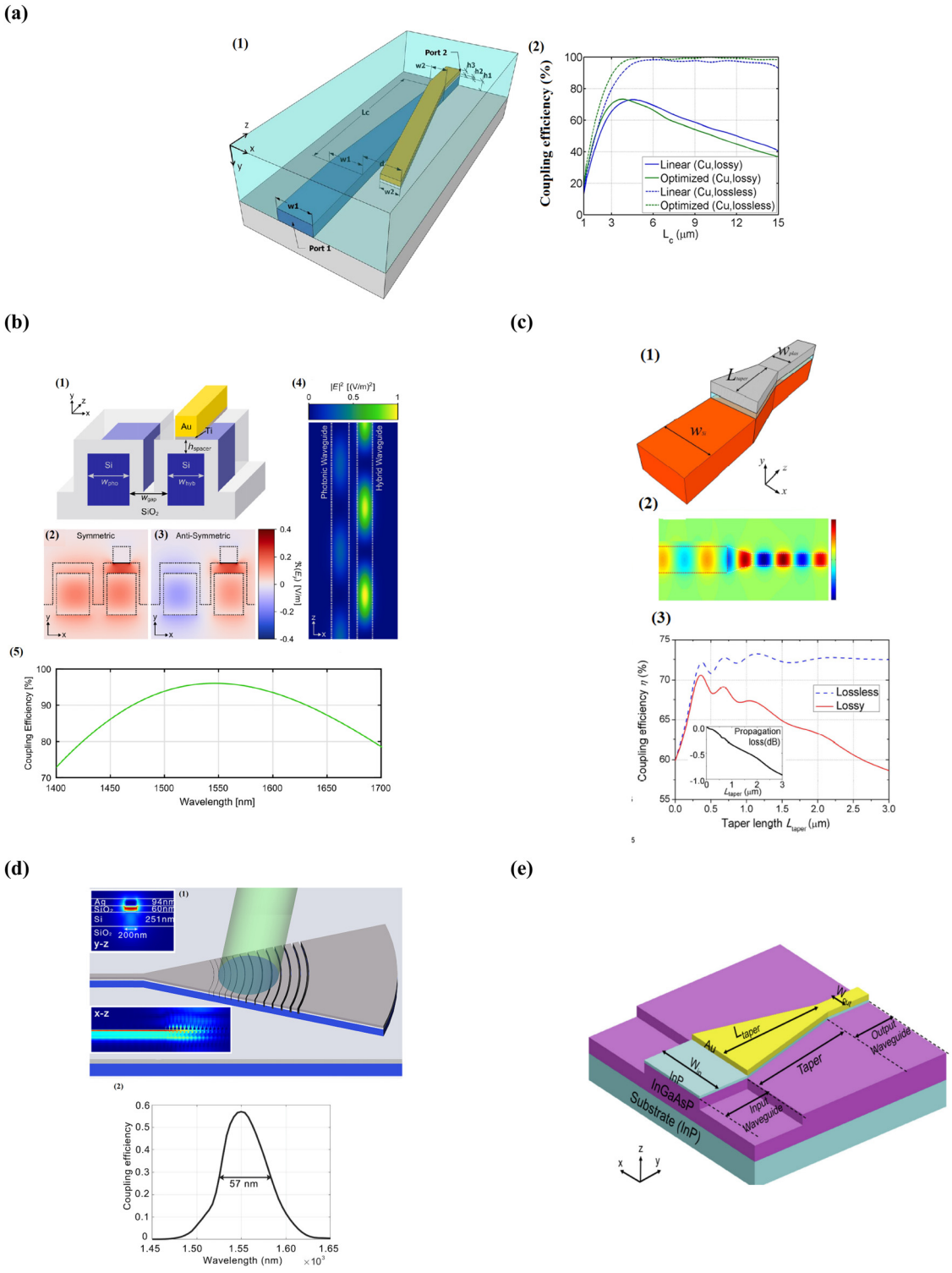

Figure 18: Various HPW couplers along with their analysis. (a) Polarization rotation and coupling structure based on mode evolution: (1) 3D scheme and geometric properties. The metal cap is depicted in yellow, the silicon core in blue, and the SiO_2 substrate and cladding shown in grey and cyan, respectively. (2) Coupling efficiency as a function of L_c for both lossy and lossless copper (Cu). Reproduced with permission from the study by Kim and Qi [241], © Nature Publishing Group. (b) Ultralow loss HPW coupler: (1) Cross-sectional diagram of the coupler illustrating the layer stacks of the photonic waveguide (on the left) and the hybrid waveguide (on the right). (2) Symmetric super-mode and (3) antisymmetric super-mode y-component electric field profiles of the coupler. (4) Top-view intensity profile of the coupler showing mode beating between the two waveguides during propagation. (5) Simulated spectral response of the coupler. Reproduced with permission from the study by Chelladurai *et al.* [245], © Optica Publishing Group. (c) Linear tapered HPW coupler: (1) Schematic representation of the hybrid plasmonic taper coupler. (2) Distribution of the

y-component electric field at y = 275 nm (center of the Al layer) for coupling with a 0.4 μm-long taper. (3) Coupling efficiency of the taper as a function of its length compared to the design using lossless silver. The inset illustrates the corresponding propagation loss for the taper. Reproduced with permission from the study by Song *et al*. [47], © Optica Publishing Group. (d) Silicon HPW fiber coupler: (1) 3D schematic view. Here, the HPW has a Si stripe and a metal cap. The upper and lower insets show the mode profile of the TM_0 mode of a 200 nm wide HPW (y–z plane) and the light propagation (x–z plane), respectively. (2) Simulated coupling spectra from the fiber to the 200 nm wide HPW. Reproduced with permission from the study by Tan *et al*. [246], © MPDI. (e) 3D schematic view of the InP-based directional coupler. Reproduced with permission from the study by Nikoufard *et al*. [247], © Elsevier.

integration, making it easier to connect external optical systems to on-chip devices, which is critical in applications like telecommunications and sensing. This approach also streamlines packaging, reducing the complexity of alignment and optical interfaces, which in turn leads to more cost-effective and reliable manufacturing processes. Furthermore, direct coupling improves signal quality by minimizing signal distortion and dispersion, which is vital for maintaining high data rates in optical communication systems. Finally, it promotes the scalability of PICs and plasmonic devices, enabling straightforward connections to standard fiber networks without requiring complex intermediary components or adapters, making it an indispensable element in modern optical technologies. In this context, Tan *et al.* were the first to propose on-chip grating couplers for silicon HPWs, marking the first known approach to direct coupling between a standard single-mode fiber and an HPW (Figure 18(d)). By utilizing apodized gratings and a two-stage taper mode converter, they have achieved a theoretical coupling efficiency of 79% (−1.03 dB) at 1,550 nm wavelength, along with a 3 dB bandwidth of 73 nm between the fiber and a 100 nm wide silicon HPW that includes a bottom metal layer. In addition, they have proposed grating couplers for three other types of silicon HPWs with metal caps, obtaining theoretical coupling efficiencies greater than 47% and bandwidths exceeding 51 nm. This direct coupling scheme offers significant advantages, including avoiding the extra insertion losses and additional alignment steps associated with conventional indirect coupling methods [246].

In parallel, SOI-based waveguides face challenges in achieving monolithic integration with active devices such as photodetectors, optical amplifiers, and lasers due to silicon indirect bandgap at optical communication wavelengths. As a result, these active devices must be integrated using a more expensive hybrid approach in silicon photonics chips [247]. In contrast, one of the key advantages offered by compound semiconductor materials based on InP is their ability to support the monolithic integration of compact and highly efficient active components, making them an attractive alternative for such applications. Therefore, as shown in Figure 18(e), a novel HPW with a layer stack of Au/InP/InGaAsP on an InP substrate has been designed. In addition, a directional coupler was integrated into the design, taking advantage of the material properties to enhance performance in optical communication systems [247]. Finally, building on the concept of CHPW, a directional coupler based on an elliptic cylindrical nanowire HPW has been proposed. This design offers a remarkably low propagation loss of 0.076 dB/μm, with a maximum energy transfer efficiency reaching 80%. These features present significant competitive advantages for achieving ultracompact directional couplers with low propagation loss, making it a promising solution for advanced photonic integration [248].

In addition to couplers, power dividers are essential components in photonic and plasmonic circuits for various reasons. Power dividers play a crucial role in splitting optical signals into multiple paths with controlled power distribution, making them indispensable in applications such as optical communication, signal processing, and sensing. By efficiently dividing power, they enable the creation of complex optical networks that can route, modulate, or process signals in parallel, enhancing the overall functionality and scalability of integrated photonic systems. Moreover, power dividers help in distributing optical power evenly among different branches of a circuit, which is vital for applications requiring uniform signal strength, such as phased arrays or multiplexing systems. When used alongside directional couplers, power dividers enable more sophisticated light manipulation and routing capabilities, making them a key building block for advanced photonic circuits and systems. Thus, incorporating power dividers, along with couplers, is fundamental for the development of efficient, compact, and highly integrated optical devices.

It is well known that a 50:50 power splitter is one of the most important fundamental elements for optical telecommunications and interconnects. As illustrated in Figure 19(a), Wang *et al.* have proposed a simple variable power splitter based on HPWs using an asymmetric Y-branch [44]. In their design, one arm of the Y-branch is fixed at a width of 200 nm while the other arm (w_1) varies from 50 to 200 nm. The resulting power splitting ratio ranges from 84%:16% to 16%:84%. This variable range is slightly larger than that of typical dielectric Y-branch power splitters.

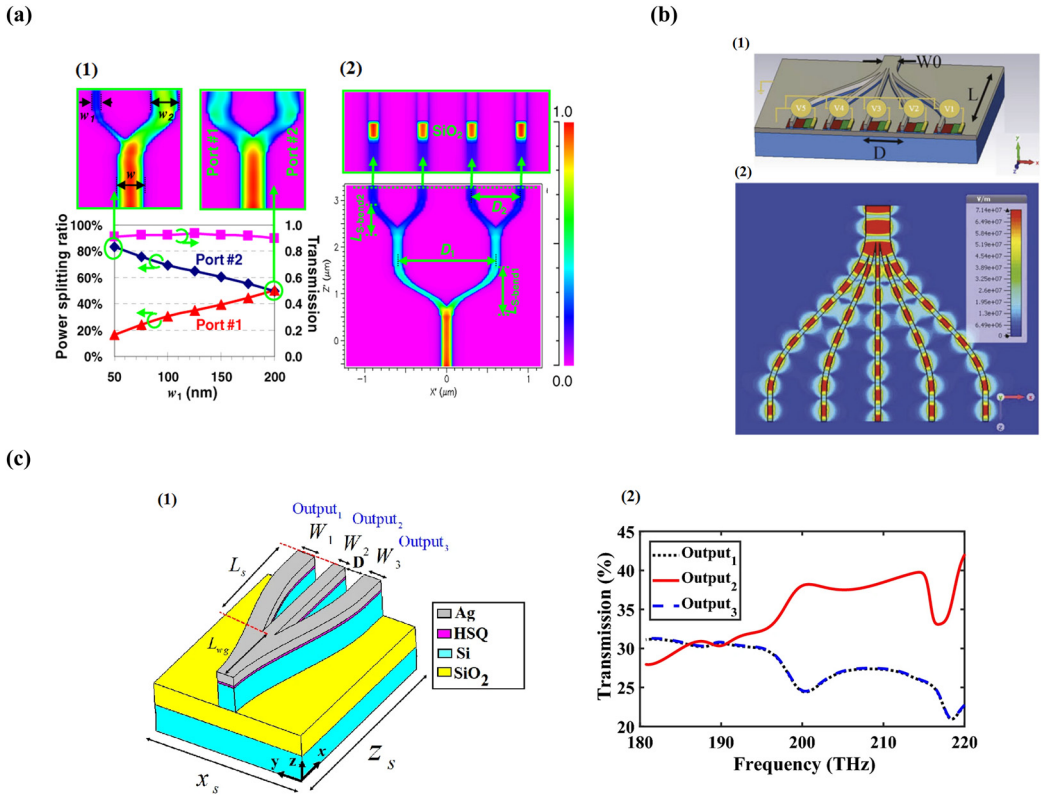

Figure 19: Different HPW power splitters and their performance. (a) 50:50 HPW splitter: (1) Power splitting ratio of the 1 × 2 Y-branch power splitter *versus* the S-bend width (w_1). The upper insets illustrate the power transmission for w_1 = 50 nm and w_1 = 200 nm. (2) Power propagation in the 1 × 4 Y-branch power splitter. The upper inset shows the output power distribution at the 10 nm-thick SiO_2 layer. Reproduced with permission from the study by Wang *et al*. [44], © Optica Publishing Group. (b) Graphene-based HPW 1 × 5 splitter: (1) Perspective view. (2) Power propagation in the 1 × 5 Y-branch. Reproduced with permission from the study by Nia *et al*. [249], © IEEE. (c) 1 × 3 Y-branch power: (1) 3D schematic view. (2) Transmission spectra. Adapted with permission from the study by Khodadadi *et al*. [208], © Nature Publishing Group.

Unlike variable MMI power splitters, the total transmission remains stable as w_1 changes. The power splitting ratio can also be tuned over a larger range by shifting the center position of the narrow S-bend with w_1 = 50 nm. They have further cascaded two Y-branch stages to create a 1 × 4 power splitter, as shown in Figure 19(a).

To reduce crosstalk, a large Y-branch has been used. A 0.5 µm long straight waveguide connects the stages. Figure 19(a) also shows power propagation through the 1 × 4 splitter, with output power distributions of 25.6, 24.3, 25.6, and 24.5%. The total transmission is approximately 83%. The device footprint, at 1.9 µm × 2.6 µm, is about 1/1,200 the size of a silicon waveguide-based 1 × 4 splitter. However, due to the intrinsic losses of HPWs, the splitter loss is slightly higher than that of its dielectric counterpart.

Moreover, Nia *et al.* have designed a 1 × 5 power splitter with switchable output ports, as shown in Figure 19(b). The structure consists of a MIM waveguide that splits into five asymmetric output branches, with the asymmetry ensuring equal power distribution across the output ports [249]. To control the light direction and switch the desired output ON while turning the other branches OFF, a graphene sheet is embedded within the SiO_2 nanolayer. This layer of graphene can toggle between the ON and OFF states due to its tunable electrical properties. By applying an external voltage, the conductivity of graphene can be modified, allowing it to either absorb or transmit light. This enables precise control over the light propagation, selectively directing it to the desired output port while effectively blocking the others. Finally, the 3D schematic of the designed HPW-based power splitter without switchable functionality is demonstrated in Figure 19(c) [208]. This design features an HPW that splits into three asymmetric output branches. Ideally, each branch would receive 33.33% of the input power to achieve equal distribution. However, due to inherent losses in the HPW and the bends in the lateral branches, the actual power distribution is slightly less. As shown in the transmission spectra, the output powers of the straight and lateral branches at 193.5 THz are 31.91, 30.17, and 30.17%, respectively. The

discrepancy is due to the higher bending losses in the lateral branches, which result in slightly lower transmission power compared to the straight branch. Finally, a comprehensive comparison of different types of HPW-based power splitter and directional coupler have been added in Table 3.

4.4 Optical forces in HPW

The generation and manipulation of optical forces using HPWs are a vibrant area of research, aiming to capitalize on the intense field confinement and enhancement properties of plasmonic structures. The idea of using light to exert forces on matter can be traced back to the early twentieth century with the discovery of radiation pressure. The innovation of optical tweezers in the 1980s, for which Arthur Ashkin received a Nobel Prize in 2018, truly propelled the field [250]. However, the forces exerted in conventional optical systems are often too weak for many applications. The advent of plasmonics provided an avenue to achieve much stronger forces due to enhanced light-matter interactions at the nanoscale. While pure plasmonic systems can produce strong optical forces, they also suffer from significant Ohmic losses. HPWs emerged as a compromise. They retain strong field confinement of plasmonics, but with reduced losses making them excellent candidates for optical force applications [251]. Here is a look at some pivotal developments in this domain.

4.4.1 Slot HPW

The strong field confinement in the slot region has been demonstrated to generate enhanced optical gradient forces. This was a breakthrough, highlighting the potential of hybrid structures in achieving notable forces at lower input powers. The refractive index detection method translates changes in the refractive index of substances into alterations in light intensity or wavelength shifts, offering a label-free means of detecting substances [252]. Many studies utilize ring resonators based on whispering gallery mode due to their noteworthy sensitivity and compact design. Yet, existing ring resonator sensors have several limitations, including a limited spectral range and overlapping resonances. While designs employing cascade rings or those integrated with gold nanodisks have aimed to mitigate these issues, they often introduce challenges such as complexity, larger size, and incompatibility with CMOS technology. Addressing these challenges, Guo *et al.* have introduced a chalcogenide suspended slot HPW (CSSHPW), as shown in Figure 20.

This design offers the advantages of robust light confinement with minimal light loss, positioning it as a potentially superior alternative to earlier models. In the realm of optical waveguide sensors, the choice of material is paramount. Chalcogenide glass (ChG) is distinguished for its unique optical attributes, which include a broad transparency range, adjustable bandgap, impressive nonlinearities, and flexible design possibilities. Owing to these properties, ChG is frequently chosen as a material for various ring resonator structures [253].

4.4.2 Resonant structures

Hybrid plasmonic racetrack resonators and ring resonators have been shown to further amplify optical forces due to the resonance condition, making them attractive for sensitive nanomechanical applications. Furthermore, Mirroring and microdisk resonators hold significant potential in the realms of filtering, optical modulation, and biosensing. Research on HPW-based iterations of these

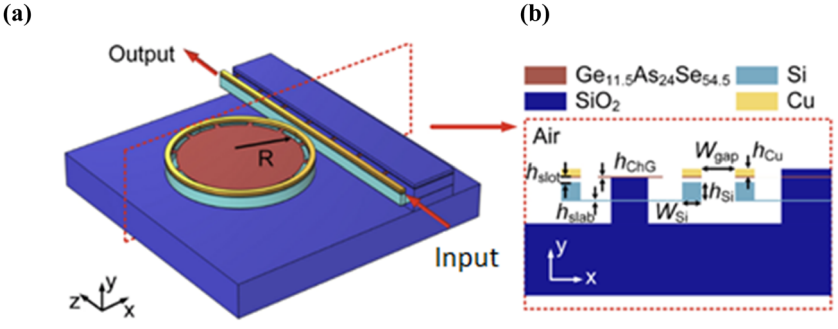

Figure 20: (a) Three-dimensional and (b) cross-sectional views of the CSSHPW mode-microring resonator. Reproduced with permission from the study by Guo *et al.* [253], © Elsevier.

resonators has been gaining traction, owing to their wide-ranging applications.

Lou *et al.* have pioneered an innovative microdisk resonator, characterized by a thin silica layer encapsulated between a gold layer and a thicker amorphous silicon layer. Transmission spectra from their prototypes showed the extinction ratio differences between the fourth- and fifth-order resonances for specific resonator radii [254].

Moreover, Butt has proposed an HPW-based racetrack ring resonator (RTRR) structure, tailored specifically for refractive index sensing applications [255]. As depicted in Figure 21(a), light is initially launched from the input port and couples into the racetrack structure under resonant conditions. Within the racetrack, the light circulates, undergoing multiple reflections and interactions, before eventually exiting through output port 2, where distinctive resonance peaks appear in the transmission spectrum, as illustrated in Figure 21(b). At the output port 1, however, resonance dips are observed, indicating points of reduced transmission at specific resonance wavelengths. These resonance peaks and dips in the transmission spectrum offer key insights into the optical properties and behavior of the RTRR. Notably, the resonance peaks at the output port 2 display a significantly higher extinction ratio compared to the dips at output port 1. However, this comes with a trade-off, as the resonance peaks also exhibit a broader full width at half maximum (FWHM), which may reduce the overall quality factor of the device. For applications such as sensing, narrower FWHM resonance dips are typically preferred for improved performance.

In addition, a microring resonator has been suggested in the study by Tang *et al.* [256], which is a metal horizontally distanced from the high-index medium. This design underscores its potential in diminishing radiation losses. However, a prominent challenge lies in the inherent temperature sensitivity of silicon-based microring resonators. The silicon substantial positive thermo-optic coefficient implies that resonators using silicon waveguides or gold–silica–silicon HPW configuration are critically temperature sensitive. Recognizing this, Zhu *et al.* have studied substituting the silica spacer with materials possessing a negative thermo-optic coefficient, like titanium dioxide (TiO_2). This novel configuration, paired with the CMOS-compatible copper metal, manifested a significant reduction in thermal sensitivity, making it an attractive alternative [43].

Notably, while high index-contrast HPW resonators, such as those deploying silicon and cadmium sulfide (CdS), are compact, they suffer from elevated propagation losses. Horvath *et al.* have championed the adoption of a lower index-contrast HPW, achieving a quality factor nearing 300, an impressive metric for plasmonic microring resonators [58]. One pivotal concern in these resonators is the radiation loss, especially when dealing with waveguide bends. Strategies to mitigate this have been proposed, including a design that separates metal from high-index medium horizontally. This distinct structure promises reduced crosstalk between adjacent devices, opening up new avenues for efficient resonator designs. A comprehensive comparison between different types of HPW ring resonator and HPW slot have been added in Table 3.

4.4.3 Particle manipulation

Nanodisk and nanorod-based hybrid plasmonic structures, emerged as powerful tools to trap, move, and manipulate nanoparticles, showing potential in lab-on-chip and biomedical applications. Nanodisks, characterized by their flat

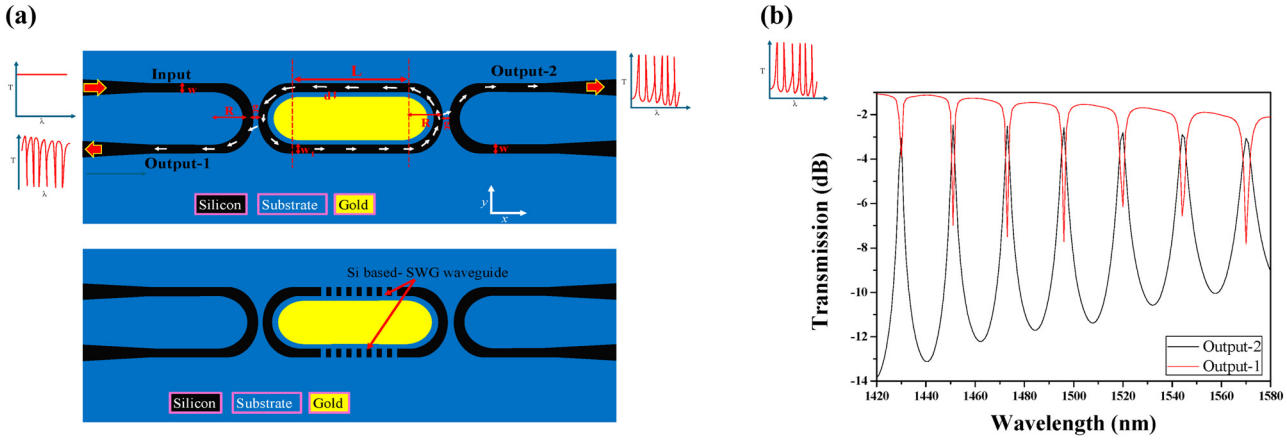

Figure 21: Graphical illustration of (a) HPW-based RTRR and SWG-HPW-based RTRR. (b) Transmission spectrum from output-1 and output-2. Reproduced with permission from the study by Butt [255], © MPDI.

and circular geometry, excel in the field confinement department. Their presence in hybrid plasmonic systems has ushered in significant enhancements in the localized field. Such enhancements have paved the way for nanodisks to become prominent tools in sensing applications. Specifically, the resonance condition of these disks can be modulated by even subtle changes in the surrounding environment. This sensitivity becomes particularly pertinent when molecules bind to the disk surface, triggering detectable resonance shifts. As researchers continue to embed nanodisks into hybrid waveguide systems, a more efficient paradigm for light-matter interactions emerges, heralding the prospect of ultra-sensitive sensors and dynamic modulators [253,257,258].

Conversely, the elongated form factor of nanorods empowers them to support plasmonic resonances along their length, facilitating enhanced interactions with light over extended regions. In practical applications, nanorods have showcased their prowess in diverse roles, including but not limited to, directional scattering, waveguiding, and amplifying nonlinear optical effects. When incorporated into hybrid systems, nanorods promise a spectrum of tunable optical responses, transforming into potent subwavelength antennas in the process. This fusion has spawned a series of innovations, including the creation of devices sensitive to polarization, adaptable optical elements, and tools that redefine the boundaries of high-resolution imaging [259].

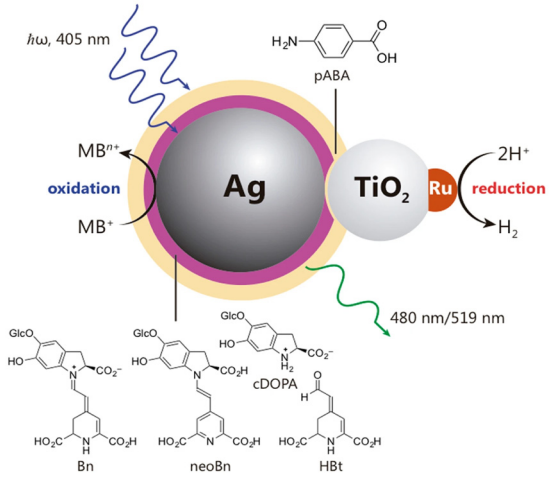

Figure 22: A nanohybrid assembly was synthesized using a modular design approach. This architecture consists of several key components: a light absorber and oxidation catalyst in the form of Ag nanoparticles, a molecular wire linker (pABA), a semiconductor base (TiO_2), a co-catalyst made of Ru nanoparticles, and regenerators (Bts) to facilitate the overall process. Reproduced with permission from the study by Pavliuk *et al.* [261], © Nature Publishing Group.

A prominent study that provides foundational knowledge and recent advances in this field includes work by Oulton *et al.*, who introduced an HPW that set the stage for subwavelength confinement and extended propagation [114]. Khurgin's exploration into plasmonic losses and the compensatory prowess of hybrid structures is another noteworthy contribution [260]. Krasnok *et al.* have further expanded on this with an in-depth discussion of all-dielectric optical nanoantennas, highlighting the diverse applications of nanodisks and nanorods [259]. Building on these foundational works, as shown in Figure 22, Pavliuk *et al.* have demonstrated a breakthrough nanohybrid photocatalytic assembly capable of simultaneous hydrogen production and pollutant oxidation, achieving solar-to-fuel efficiencies of up to 20%. Their modular approach to plasmonic material design enables fine-tuning of photocatalytic properties, representing a significant advancement in light-to-chemical energy conversion and addressing key challenges in sustainable energy development [261].

4.4.4 Dynamic control

Dynamic control: In the rapidly advancing realm of nanophotonics, the quest for dynamic control over optical forces is unceasing. A prominent avenue that has emerged in recent years is the integration of phase change materials (PCMs) and liquid crystals within HPWs. These materials offer a unique set of properties that render them invaluable for enabling tunable and reconfigurable optical forces. PCMs have gained attention for their ability to transition between distinct crystalline states, typically amorphous and crystalline, in response to external stimuli such as heat or light. This transition is often accompanied by significant changes in optical properties, notably refractive index. Within a hybrid plasmonic context, the integration of PCMs can lead to a rapid switch between on and off states, allowing for modulation of propagating SPP modes. This dynamic modulation capability heralds potential applications in reconfigurable optical devices, switchable sensors, and adaptive light-matter interactions. In this regard, electro-optic modulators and switches stand as cornerstones in the field of optical communication. Traditional silicon-based electro-optic modulators, albeit functional, are often bulky due to their reliance on weak nonlinear effects. Microring resonators have paved the way for miniaturization but come with inherent drawbacks like limited bandwidth and a high sensitivity to temperature fluctuations. Notably, a slew of HPW-based modulators and switches have emerged, promising to counter these challenges [244,262–265].

In a notable study, Sorger *et al.* have presented a modulator that employs a gold–ITO-silicon HPW configuration [244]. The application of a forward bias voltage on the waveguide culminates in an accumulation layer within the HPW. This subsequently elevates the imaginary part of the ITO refractive index, amplifying the HPW propagation loss. The device, given its high extinction ratio and extensive bandwidth exceeding 1,000 nm, positions itself as a promising contender for future PICs.

The intriguing property of Mott insulators like vanadium dioxide (VO_2) is their ability to undergo a dramatic metal/insulator phase transition when subjected to thermal or electrical stimuli. This induces significant alterations in their material attributes. Joushaghani *et al.* have introduced a sub-volt hybrid plasmonic VO_2 switch that exploits this phenomenon [262]. The device architecture involves a silver film atop a silica spacer, overlaying a VO_2 film. A subsequent shift in the mode profiles due to temperature fluctuations results in pronounced propagation loss variations, rendering the device exceedingly efficient. Ooi's research team has postulated the implementation of a novel metal–TiO_2–VO_2–TiO_2–metal waveguide for a compact electro absorption modulator [263]. This device oscillates between on and off states based on the phase of VO_2, either insulating or metallic. Simulations from their study hint at a promising modulator with a modulation depth of approximately 10 dB, and an impressively low energy consumption of 2.6 fJ/bit.

Sun *et al.* have conceptualized a modulator with a distinct Ag-polymer–Si-polymer–Ag layout [95]. This structure is fascinating as it supports two hybrid modes with diverse field profiles. The power interplay between these modes profoundly influences the final output, making the device highly efficient with a commendable modulation bandwidth. Moreover, as shown in Figure 23, Li *et al.* have delved into designing a 16-point quadrature amplitude modulation mechanism employing HPW [264]. Their design hinges on two HPW-based phase shifters, leveraging a highly nonlinear polymer as the spacer medium. Preliminary predictions suggest that a compact device could achieve a staggering modulation bandwidth exceeding 1 THz. Furthermore, the first-ever hybrid graphene plasmonic waveguide modulator, employing diverse configurations, has been introduced in the study by Ansell *et al.* [265]. These configurations span from a straightforward coplanar setup, where SPPs traverse along a metal–dielectric interface next to a graphene monolayer, to the most optimized version employing wedge SPPs that generate potent electrical fields along the graphene layer. The modulation approach of the propagating SPP modes leverages the optical Pauli blocking effect. Rooted in the modification of graphene optical conductivity due to the Fermi energy shift brought on by gating, this technique holds the potential to fully obstruct optical transitions in graphene at 1,550 nm.

5 Challenges and perspectives

5.1 HPWs fabrication issues and advanced solutions

The fabrication of HPWs involves multiple complex steps that require nanoscale precision and the use of advanced fabrication techniques. The fabrication procedure as outlined in Figure 24 has been explained in the study by Adhikari *et al.* [284]:

Step 1: The process begins with selecting and preparing a suitable substrate, commonly made of silicon, glass, or other semiconductor materials. The substrate is thoroughly

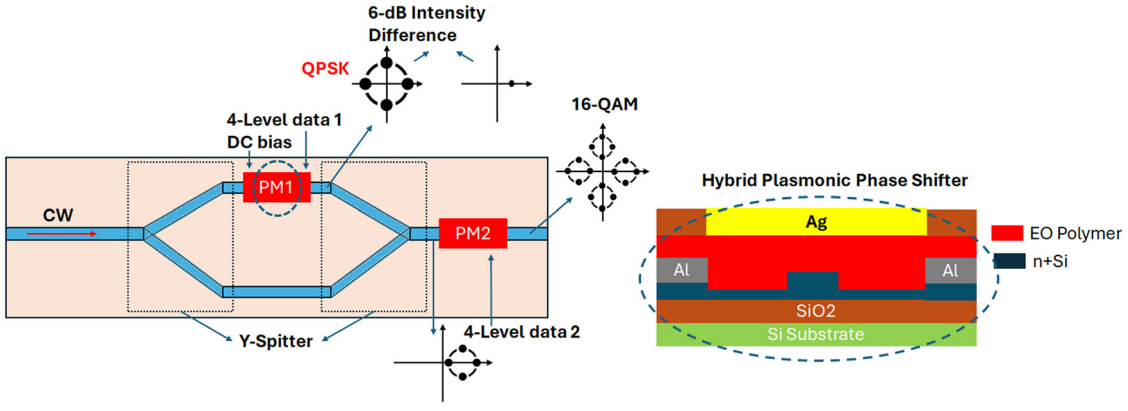

Figure 23: The scheme of the 16-QAM HPW modulator based on HPW phase shifter. The inset is the simulated back-to-back square 16-QAM constellation. Adapted with permission from the study by Li *et al.* [264], © Elsevier.

cleaned using solvent cleaning (acetone, isopropanol, and deionized water) and dried with nitrogen gas. Oxygen plasma cleaning may also be employed to ensure the surface is free from organic contaminants, improving the adhesion of subsequent layers.

Step 2: A high refractive index dielectric material, such as silicon, TiO_2, or Si_3N_4, is deposited onto the substrate. This layer acts as the primary guiding medium in the waveguide. Techniques such as chemical vapor deposition (CVD), plasma-enhanced CVD (PECVD), or atomic layer deposition (ALD) are commonly used for this step, depending on the required thickness and uniformity. The layer thickness typically ranges from tens to hundreds of nanometers.

Step 3: A thin layer of low refractive index material, such as silicon dioxide (SiO_2) or magnesium fluoride (MgF_2), is deposited on top of the high refractive index dielectric layer. This low-index layer helps confine light by creating a refractive index contrast between the high-index layer and the metal layer. The thickness of this layer is typically in the range of a few nanometers to tens of nanometers, depending on the design. Techniques such as ALD, PECVD, or thermal evaporation can be used to deposit this layer with high precision.

Step 4: The metal layer, which acts as the plasmonic component of the waveguide, is deposited on top of the low refractive index layer. Common metals like gold or silver are used due to their excellent plasmonic properties. The metal layer is deposited using electron beam evaporation or sputtering to achieve a smooth and uniform layer. The thickness of the metal layer typically ranges from 10 to 100 nm, depending on the waveguide intended application.

Step 5: The waveguide structure is patterned using electron beam lithography (EBL). A resist layer, such as polymethyl methacrylate, is spin coated onto the metal layer and selectively exposed to an electron beam, creating the desired waveguide pattern. This step defines the shape and geometry of the HPW.

Step 6: After exposure, the resist is developed using a suitable solvent, revealing the underlying material where the waveguide pattern was defined. Reactive ion etching or inductively coupled plasma etching is employed to remove unwanted portions of the metal and dielectric layers, leaving behind the waveguide structure. This step must be carefully controlled to preserve the thin layers and maintain the integrity of the structure.

Step 7 (optional): If needed, chemical mechanical polishing is performed to ensure the smoothness of the layers and to planarize the surface. This step ensures that the structure is free from surface imperfections that could affect light propagation in the waveguide.

Step 8 (optional): In some designs, a passivation layer or additional cladding is deposited on top of the metal layer to protect the structure from environmental factors such as oxidation. This can be done using ALD or PECVD to create a thin dielectric layer (*e.g.*, SiO_2) for protection without affecting the optical performance.

Step 9 (optional): The fabricated waveguide is inspected using techniques such as SEM or atomic force microscopy to verify the nanoscale features and ensure that the layers have the correct thickness and uniformity. Optical characterization methods such as transmission measurements or near-field scanning optical microscopy are used to assess the waveguide performance and validate its design.

Fabricating HPWs experimentally presents several significant challenges that require advanced techniques and meticulous attention to detail. One of the primary difficulties in fabricating HPWs lies in achieving nanoscale precision. These waveguides are extremely small, often with dimensions on the order of tens of nanometers, which necessitates the use of advanced lithographic techniques. Methods such as EBL or focused ion beam milling are typically employed [99,285]. However, these techniques can be both complex and expensive, adding to the difficulty of producing HPWs at a consistent and scalable level. The selection and quality of materials used in HPWs are also critical factors in their fabrication. HPWs require specific material properties to function optimally, such as high conductivity for metal layers and low optical losses for dielectric components. The performance of HPWs is highly sensitive to material quality. Imperfections like surface roughness or inhomogeneities can lead to increased losses and reduced propagation lengths [132]. Therefore, the careful choice of high-quality materials is essential to ensure low-loss operation and maximize the efficiency of light confinement. Another challenge is the fabrication of complex structures found in some HPW designs. Certain configurations, such as those with metallic cores and claddings in coaxial HPWs or dielectric wedges in modified HPWs, involve intricate geometries. Fabricating these structures can require sophisticated and multistep processes, which increase the complexity of the overall fabrication procedure [152].

Maintaining uniformity and precise control over layer thickness is another critical aspect of HPW fabrication. Since HPWs often consist of very thin material layers, even minor deviations in layer thickness can significantly affect their optical properties [286]. For instance, variations in thickness may impact the coupling between SPPs and guided modes, thereby influencing the performance of the waveguide. Techniques such as ALD are often employed to achieve atomic-level thickness control and ensure the uniformity of the deposited layers [287]. Integration of HPWs

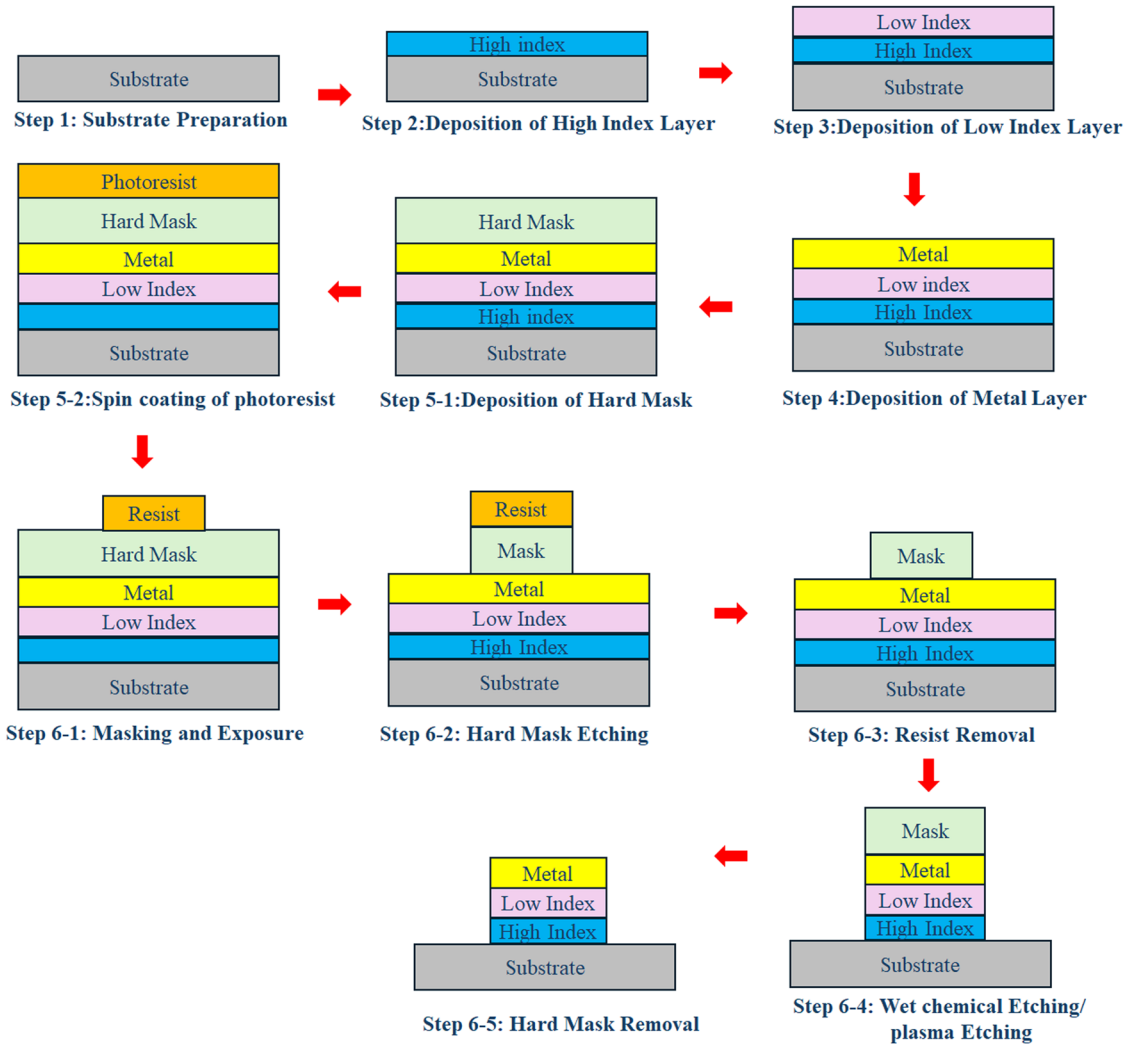

Figure 24: Fabrication steps of a typical HPW consisting of a substrate and a low refractive index layer sandwiched between a high refractive index layer and a metal layer.

with other photonic or electronic components adds further complexity. The small size of HPWs, combined with the potentially different fabrication processes and material requirements of adjacent components, can complicate the integration process. Achieving seamless integration is essential for realizing functional photonic circuits that incorporate HPWs alongside other optical and electronic elements. The stability and durability of HPWs also present challenges [288]. Many HPWs rely on thin metal layers, which are prone to oxidation and degradation over time, especially when exposed to varying environmental conditions. Protecting these delicate structures and ensuring long-term stability is crucial for maintaining their performance in practical applications [125].

Finally, achieving reproducibility in HPW fabrication is a persistent issue. The requirement for nanoscale precision and the potential for imperfections in both materials and fabrication processes mean that reproducing high-performance HPWs consistently can be difficult. Variations in fabrication quality can lead to inconsistencies in performance, hindering the scalability of HPW technology [289]. Addressing these challenges requires a combination of cutting-edge fabrication techniques, careful material selection, and collaborative efforts across various disciplines. By continuing to advance fabrication processes and improve material quality, the development of HPWs will accelerate, paving the way for their integration into a wide range of cutting-edge technologies.

5.1.1 Fabrication tolerances and beyond

Fabrication tolerance is a critical factor in the design of HPWs due to the extreme sensitivity of plasmonic modes to

nanoscale structural variations. HPWs typically involve precise geometries where metal and dielectric materials are positioned within subwavelength distances, and even slight discrepancies during fabrication can introduce significant performance degradation. For instance, variations in the thickness of dielectric layer or the width of metal waveguide by just a few nanometers can drastically alter the effective mode index, propagation loss, and confinement efficiency. A study by Bian and Gong demonstrated that deviations in dielectric thickness within a few nanometers lead to shifts in resonance conditions, causing mismatch in mode coupling and reducing overall device efficiency [148]. This sensitivity is especially pronounced in designs where tight confinement is required, as these modes rely on precise structural parameters to achieve effective field localization.

Surface roughness, an often inevitable result of metal deposition processes like EBL or thermal evaporation, adds another layer of complexity [132]. Research has shown that surface roughness, even at the atomic scale, can significantly increase scattering losses, particularly in HPWs where the plasmonic modes are confined close to the metal surface. In one study, Bian and Gong have quantified the propagation loss in HPWs due to surface roughness, revealing that roughness levels as low as 1–2 nm can lead to a measurable reduction in transmission efficiency [148]. These scattering losses are especially detrimental in HPWs intended for long propagation distances or applications requiring low signal attenuation, as they limit the effective interaction length and reduce the device's operational bandwidth.

Another important aspect of fabrication tolerance in HPWs is its impact on mode coupling, especially in devices designed to interface with other photonic structures or achieve specific modal overlaps. Published works have highlighted that coupling efficiency between HPWs and other components, such as standard dielectric waveguides or grating couplers, can drop sharply when dimensions deviate from optimal values. For example, Bian and Gong have observed that coupling losses increased by over 20% when the HPW width varied by just a few nanometers, underscoring the critical importance of dimensional control [132,148]. To mitigate these coupling losses, some researchers have proposed introducing tapering structures or employing optimized etching techniques to enhance fabrication precision, as these methods can minimize sensitivity to variations in waveguide width and height.

Moreover, tolerance analysis has become a standard part of the design process for HPWs, as recent studies emphasize the need for simulation-based tolerance testing to predict performance under realistic fabrication conditions. Some authors have adopted Monte Carlo simulations to model a range of fabrication imperfections, allowing them to identify design parameters that are less sensitive to variations. For instance, Bian and Gong have used tolerance modeling to identify dielectric thicknesses that maintained mode confinement despite potential deviations [148]. By selecting designs that demonstrate robustness to common fabrication errors, such as those associated with deposition thickness, alignment, and etching precision, designers can increase the yield of functional devices. This approach not only improves reliability but also reduces the cost and time associated with device iteration and testing.

The maximum fabrication error tolerance in HPW simulations is crucial and typically falls within a few nanometers, depending on the specific design and application. This level of precision is essential due to the high sensitivity of HPW to small changes in structural dimensions, which can impact the intense field confinement of plasmonic modes at metal–dielectric interfaces. In most simulations, error tolerances are kept within 1–10 nm to capture the kinds of variations likely to occur during fabrication. For instance, the thickness of the dielectric layer is a critical parameter; small shifts of ±1–5 nm in thickness can impact how electromagnetic fields are confined, resulting in altered resonance conditions and increased propagation losses. Typical designs use a ±3 nm tolerance to accommodate these small but impactful variations while maintaining functionality. Similarly, the width of the waveguide and the spacing in gap-based HPWs, where a small dielectric gap is sandwiched between metal and dielectric layers, require a tolerance of around ±5 nm. Deviations beyond this range can disturb the strong field confinement needed for effective operation, reducing coupling efficiency and altering the device propagation characteristics.

Surface roughness is another factor that requires attention. Roughness on the order of ±1–2 nm at metallic interfaces can increase scattering losses, leading to decreased transmission efficiency, especially over longer propagation distances. Surface irregularities can also influence the plasmonic modes, introducing additional losses and limiting the performance of HPWs in applications where low signal attenuation is essential. For applications with higher performance requirements, stricter tolerances may be necessary, though they tend to increase fabrication costs and complexity. Balancing these tolerances effectively is therefore a key, as it ensures that the HPW design remains both manufacturable and aligned with the intended performance, even within realistic fabrication limits.

Beyond fabrication tolerances, several other considerations are crucial for accurately designing and simulating HPWs, ensuring the device performs as intended

and meets specific design requirements. The choice of materials in HPWs is fundamental, as it directly influences performance due to losses arising from metal absorption and the interactions between metal and dielectric materials. Metals like gold and silver are favored for their plasmonic properties but also introduce optical losses, particularly in the visible and NIR ranges. This makes precise characterization of materials, including refractive index and absorption coefficients, essential, as any changes in these properties, such as those caused by oxidation or alloying during fabrication, can affect plasmonic behavior and reduce device efficiency. Simulations should incorporate realistic material parameters, possibly exploring alternative materials or alloys to minimize losses [290].

Thermal effects also play a significant role in HPW performance, especially in high-intensity applications. Heating can alter the refractive index of dielectric materials and potentially cause thermal expansion of the metal, which impacts mode confinement and propagation characteristics. Over time, repeated thermal cycling may degrade metal surfaces, increasing roughness and scattering losses. To address these issues, simulations can incorporate temperature-dependent material parameters to assess device behavior under typical operating conditions. Thermal management strategies, such as incorporating heat sinks or using low-loss dielectric materials, can help mitigate these effects [291].

Ensuring effective mode confinement is another fundamental aspect of HPW design, as plasmonic modes are highly sensitive to geometry and surrounding materials. HPWs often support hybrid modes where electromagnetic fields are tightly confined at the metal–dielectric interface. Detailed modal analysis in simulations is essential to understand how field distribution, confinement factor, and effective mode index respond to structural and material variations, which helps in optimizing waveguide geometry, particularly for applications that demand high field confinement, such as nonlinear optics or sensing [292].

Coupling efficiency is essential for HPWs to function effectively within larger photonic systems, particularly when connecting with other photonic components like dielectric waveguides or fiber couplers. HPWs often experience mode mismatch with these components due to the strong field localization at the metal–dielectric interface, resulting in coupling losses. To improve this, simulations incorporate coupling interfaces and tapering structures to enhance mode overlap and reduce losses. Various coupling structures, such as grating couplers, tapers, or adiabatic couplers, are frequently explored to increase efficiency while minimizing sensitivity to fabrication variations [110].

Dispersion management is another critical factor in HPW applications requiring broadband or pulsed light. Dispersion affects pulse shape and propagation speed, and HPWs exhibit strong dispersion due to the nature of plasmonic modes, particularly at metal–dielectric interfaces. Simulations should analyze dispersion across the operational bandwidth to meet phase-matching conditions and minimize pulse distortion. Dispersion-compensating designs, such as specific waveguide geometries or multilayered structures, can help achieve the desired dispersion properties [293].

Nonlinear effects also become significant in HPWs with intense optical fields. HPWs enhance nonlinear interactions, which is advantageous for applications like all-optical switching or frequency conversion. However, this adds complexity to simulations since the intensity-dependent refractive index changes alter mode propagation and can lead to self-focusing or defocusing. Accurate modeling requires analyzing field distribution and intensity within the waveguide and incorporating nonlinear material parameters, balancing accuracy with computational demands [173].

As HPWs shrink to nanoscale dimensions, quantum effects may become relevant, particularly in metallic regions where electron confinement influences plasmonic behavior. Quantum confinement, nonlocal response, and tunneling can modify plasmonic modes in ways that classical models cannot capture. Quantum corrections to the dielectric function may be necessary in simulations to improve accuracy, especially for ultrathin layers, though this detail is generally not required for larger structures [294].

Mechanical stability and durability are additional considerations, given that HPWs are constructed with nanometer-scale structures and may experience stress during fabrication, packaging, or operation. Mechanical stability analysis, sometimes coupled with thermal simulations, helps ensure the design can withstand expected stresses without significant deformation. Selecting substrate materials that offer both thermal and mechanical stability or incorporating protective coatings to prevent oxidation can help maintain structural integrity over time.

Scalability and fabrication feasibility also need to be considered. While a design might perform exceptionally in simulations, the feasibility of fabricating it at scale presents unique challenges. HPW structures that require complex fabrication techniques, such as EBL or ALD, can be difficult to mass-produce. Designers must balance performance with manufacturability by simplifying geometries or choosing alternative materials that align with conventional fabrication methods. Some simulation studies use

simplified models that approximate complex designs to determine whether scalable versions of HPWs can still meet performance requirements [295,296].

In summary, HPW design demands a comprehensive approach that accounts for material properties, thermal and mechanical stability, modal and dispersion characteristics, coupling efficiency, and nonlinearity. By accurately modeling each of these factors in simulations, HPWs can achieve high performance and robustness, meeting both functional and manufacturability requirements.

5.2 Perspective of HPWs

HPWs are promising nano-optical components with the potential to influence several fields, including telecommunications, biosensing, quantum information processing, and photovoltaics. Their ability to confine light at scales smaller than the diffraction limit is transforming optical technologies and opening up new possibilities. In telecommunications and data centers, HPWs can contribute significantly to advancements in high-density photonic integration. Their capacity to guide light at the nanoscale can lead to smaller, faster, and more energy-efficient photonic devices, which are essential for ultrafast data transmission, processing, and storage systems. Moreover, in biosensing and medical diagnostics, HPWs can be utilized to create highly sensitive biosensors. The strong light-matter interaction at the metal–dielectric interface allows for the detection of small changes in the local refractive index, making them suitable for identifying biological molecules such as proteins and DNA or monitoring chemical changes. This has the potential to revolutionize point-of-care diagnostics and enable real-time monitoring of biological processes.

HPWs can also be employed in on-chip spectroscopy, where the strong light-matter interaction is beneficial for applications such as Raman spectroscopy or IR absorption spectroscopy, which are critical for chemical analysis in various fields, including pharmaceuticals and environmental monitoring. In addition, in quantum information processing, HPWs can facilitate the development of compact and efficient single-photon sources, detectors, and quantum gates. Their strong light-matter interaction makes them useful for quantum state manipulation and single-photon operations, which are key to the advancement of quantum technologies. HPWs also have potential applications in nonlinear optics, where their ability to confine light can enhance the nonlinear response of a medium. This enables efficient frequency conversion, optical switching, and other nonlinear phenomena, all of which are essential for improving optical communication and processing technologies. Finally, HPWs may play a role in advancing plasmon-enhanced photovoltaics. By incorporating HPWs into solar cells, light absorption can be significantly increased due to the strong interaction between light and plasmonic structures. This could lead to improved efficiency in solar energy harvesting and the development of more cost-effective solar cells.

6 Conclusion

This article has traversed the dynamic and promising terrain of HPWs, laying bare the vast potential they hold in transforming optical communication, data processing, biosensing, and the broader domain of nanophotonics. By ingeniously merging the strengths of dielectric and plasmonic waveguides, HPWs stand at the frontier of overcoming the longstanding dilemma of balancing high propagation loss with strong confinement, heralding a new era of nanoscale optical manipulation. Through a meticulous exploration of the theoretical underpinnings of plasmonics and the evolutionary journey of HPWs, to a detailed examination of their diverse structures and the unique blend of opportunities and challenges they present, this review illuminates the path for future exploration. The critical analysis of HPWs structural varieties, each with its distinct advantages and inherent limitations, underscores the nuanced understanding required to harness their full potential. Moreover, the exploration of HPWs expansive applications highlights their pivotal role in advancing various scientific and technological fields. However, the journey is far from complete. The challenges identified in fabrication, structural integrity, and material constraints not only demarcate the current boundaries of HPWs capabilities but also chart the course for future research. As this review underscores the need for innovative solutions to these challenges, it also envisions a future where the untapped potential of HPWs is fully realized, paving the way for groundbreaking advancements in plasmonics and beyond. This comprehensive review, therefore, does not mark the end but rather a beckoning to the scientific community to further innovate, explore, and expand the horizons of HPWs, ensuring their pivotal role in the future of nanophotonic technologies.

Funding information: The authors state no funding involved.

Author contributions: All authors have accepted responsibility for the entire content of this manuscript and approved its submission.

Conflict of interest: The authors state no conflict of interest.

Data availability statement: Data sharing is not applicable to this article as no datasets were generated or analysed during the current study.

References

[1] Knight MW, King NS, Liu L, Everitt HO, Nordlander P, Halas NJ. Aluminum for plasmonics. ACS Nano. 2014;8:834–40.

[2] Makarov SV, Zalogina AS, Tajik M, Zuev DA, Rybin MV, Kuchmizhak AA, et al. Light-induced tuning and reconfiguration of nanophotonic structures. Laser Photon Rev. 2017;11:1700108.

[3] Lin CCC, Chang PH, Helmy AS. Supermode hybridization: a material-independent route toward record schottky detection sensitivity using <0.05 μm^3 amorphous absorber volume. Nano Lett. 2020;20:8500–7.

[4] Dastmalchi P, Haddadpour A, Veronis G. Nanophotonics: devices for manipulating light at the nanoscale. In: Feldman M, editor. Nanolithography: the art of fabricating nanoelectronic and nanophotonic devices and systems. Cambridge, UK: Woodhead Publishing; 2014. 376–98.

[5] Maier SA, Brongersma ML, Kik PG, Meltzer S, Requicha AA, Atwater HA. Plasmonics-a route to nanoscale optical devices. Adv Mater. 2001;13:1501–5.

[6] Brongersma ML, Halas NJ, Nordlander P. Plasmon-induced hot carrier science and technology. Nat Nanotechnol. 2015;10:25–34.

[7] Lalanne P, Chavel P. Metalenses at visible wavelengths: past, present, perspectives. Laser Photon Rev. 2017;11:1600295.

[8] Teng D, Wang K, Huan Q, Chen W, Li Z. High-performance light transmission based on graphene plasmonic waveguides. J Mater Chem C. 2020;8:6832–8.

[9] Genevet P, Capasso F, Aieta F, Khorasaninejad M, Devlin R. Recent advances in planar optics: from plasmonic to dielectric metasurfaces. Optica. 2017;4:139–52.

[10] Wang G, Lu H, Liu X, Mao D, Duan L. Tunable multi-channel wavelength demultiplexer based on MIM plasmonic nanodisk resonators at telecommunication regime. Opt Express. 2011;19:3513–8.

[11] Fitrakis EP, Kamalakis T, Sphicopoulos T. Slow light in insulator–metal–insulator plasmonic waveguides. J Opt Soc Am B. 2011;28:2159–64.

[12] Veronis G, Fan S. Guided subwavelength plasmonic mode supported by a slot in a thin metal film. Opt Lett. 2005;30:3359–61.

[13] Steinberger B, Hohenau A, Ditlbacher H, Aussenegg FR, Leitner A, Krenn JR. Dielectric stripes on gold as surface plasmon waveguides: Bends and directional couplers. Appl Phys Lett. 2007;91:081111.

[14] Gosciniak J, Holmgaard T, Bozhevolnyi SI. Theoretical analysis of long-range dielectric-loaded surface plasmon polariton waveguides. J Lightwave Technol. 2011;29:1473–81.

[15] Garcia-Ortiz CE, Coello V, Pisano E, Bozhenolnyi SI. Plasmonic directional couplers using channel waveguides in random arrays of metal nanoparticles. Opt Express. 2019;27:22753–63.

[16] Tong H, Xu Y, Su Y, Wang X. Theoretical study for fabricating elliptical subwavelength nanohole arrays by higher-order waveguide-mode interference. Results Phys. 2019;14:102460.

[17] Sun C, Rong K, Wang Y, Li H, Gong Q, Chen J. Plasmonic ridge waveguides with deep-subwavelength outside-field confinements. Nanotechnol. 2016;27:065501.

[18] Kress SJP, Antolinez FV, Richner P, Jayanti SVD, Kim K, Prins F, et al. Wedge waveguides and resonators for quantum plasmonics. Nano Lett. 2015;15:6267–75.

[19] Alam MZ. Hybrid plasmonic waveguides: theory and applications [dissertation]. Ontario (ON): University of Toronto; 2012.

[20] Wassel HMG, Dai D, Tiwari M, Valamehr JK, Theogarajan L, Dionne J, et al. Opportunities and challenges of using plasmonic components in nanophotonic architectures. IEEE J Emerg Sel Top Circuits Sys. 2012;2:154–68.

[21] Citrin DS. Plasmon-polariton transport in metal-nanoparticle chains embedded in a gain medium. Opt Lett. 2006;31:98–100.

[22] Danzi S, Schnabel V, Gabl J, Sologubenko A, Galinski H, Spolenak R. Rapid on-chip healing of metal thin films. Adv Mat Technol. 2019;4:1800468.

[23] Meira DI, Domingues RP, Rodrigues MS, Alves E, Barradas NPB, Borges J, et al. Thin films of Au-Al_2O_3 for plasmonic sensing. Appl Surf Sci. 2020;500:144035.

[24] Gather MC, Meerholz K, Danz N, Leosson K. Net optical gain in a plasmonic waveguide embedded in a fluorescent polymer. Nat Photon. 2010;4:457–61.

[25] Alam MZ, Meier J, Aitchiston JS, Mojahedi M. Gain assisted surface plasmon polariton in quantum wells structures. Opt Express. 2007;15:176–82.

[26] Alam MZ, Atichiston JS, Mojahedi M. Theoretical analysis of hybrid plasmonic waveguide. IEEE J Sel Top Quant Electron. 2013;19:4602008.

[27] Aldawsari S. Comprehensive theoretical studies of guided modes in multilayer hybrid plasmonic waveguides [dissertation]. Ontario (ON): University of Waterloo; 2018.

[28] Salvador R, Martinez A, Garcia-Meca C, Ortuno R, Marti J. Analysis of hybrid dielectric plasmonic waveguides. IEEE J Sel Top Quant Electron. 2008;14:1496–501.

[29] He X, Ning T, Pei L, Zheng J, Li J, Wang J. Deep subwavelength graphene-dielectric hybrid plasmonic waveguide for compact photonic integration. Results Phys. 2021;21:103834.

[30] Bian Y, Zheng Z, Zhao X, Liu L, Su Y, Liu J, et al. Hybrid plasmonic waveguide incorporating an additional semiconductor stripe for enhanced optical confinement in the gap region. J Opt. 2013;15:035503.

[31] Okda HA, Rabia SI, Shalaby HMH. Sensitivity enhancement of a difference interferometer refractive index sensor based on a silicon-on-insulator hybrid plasmonic waveguide. J Opt Soc Am B. 2021;38:1405–15.

[32] Butt MA, Kazanskiy NL, Khonina SN. Modal characteristics of refractive index engineered hybrid plasmonic waveguide. IEEE Sens J. 2020;20:9779–86.

[33] Kumar A, Gosciniak J, Volkov VS, Papaionnou S, Kalavrouziotis D, Vyrsokinos K, et al. Dielectric-loaded plasmonic waveguide components: Going practical. Laser Photon Rev. 2013;7:938–51.

[34] Economou EN. Surface plasmons in thin films. Phys Rev. 1969;182:539–54.

[35] Khurgin JB, Boltasseva A. Reflecting upon the losses in plasmonics and metamaterials. MRS Bull. 2012;37:768–79.

[36] Naik GV, Shalaev VM, Boltasseva A. Alternative plasmonic materials: beyond gold and silver. Adv Mater. 2013;25:3264–94.

[37] McMahon JM, Schatz GC, Gray SK. Plasmonics in the ultraviolet with the poor metals Al, Ga, In, Sn, Tl, Pb, and Bi. Phys Chem Chem Phys. 2013;15:5415–23.

[38] Dabos G, Manolis A, Tsiokos D, Ketzaki D, Chatzianagnostou E, Markey L, et al. Aluminum plasmonic waveguides co-integrated

with Si_3N_4 photonics using CMOS processes. Sci Rep. 2018;8:13380.
[39] Miadecchi G, Gonella G, Zaccaria P, Moroni R, Anghinolfi R, Giglia A, et al. Deep ultraviolet plasmon resonance in aluminum nanoparticle arrays. ACS Nano. 2013;7:5834–41.
[40] Sturlesi B, Grajower M, Mazurski N, Levy U. Integrated amorphous silicon-aluminum long-range surface plasmon polariton (LR-SPP) waveguides. APL Photon. 2018;3:036103.
[41] Fedyanin DY, Yakubovsky DI, Kirtaev RV, Volkov VS. Ultralow-loss CMOS copper plasmonic waveguides. Nano Lett. 2016;16:362–6.
[42] Weeber JC, Arocas J, Heintz O, Markey L, Viarbitskaya S, Colas-des-Francs G, et al. Characterization of CMOS metal based dielectric loaded surface plasmon waveguides at telecom wavelengths. Opt Express. 2017;25:394–408.
[43] Zhu S, Lo GQ, Xie J, Kwong DL. Toward athermal plasmonic ring resonators based on Cu-TiO_2-Si hybrid plasmonic waveguide. IEEE Photon Technol Lett. 2013;25:1161–4.
[44] Wang J, Guan X, He Y, Shi Y, Wang Z, He S, et al. Sub-μm^2 power splitters by using silicon hybrid plasmonic waveguides. Opt Express. 2011;19:838–47.
[45] Dai D, He S. A silicon-based hybrid plasmonic waveguide with a metal cap for a nano-scale light confinement. Opt Express. 2009;17:16646–53.
[46] Gao L, Tang L, Hu F, Guo R, Wang X, Zhou Z. Active metal strip hybrid plasmonic waveguide with low critical material gain. Opt Express. 2012;20:11487–95.
[47] Song Y, Wang J, Li Q, Yan M, Qiu M. Broadband coupler between silicon waveguide and hybrid plasmonic waveguide. Opt Express. 2010;18:13173–79.
[48] Sharma T, Kumar M. Hollow hybrid plasmonic waveguide for nanoscale optical confinement with long-range propagation. Appl Opt. 2014;53:1954–7.
[49] Li Y, Xu C, Zeng C, Wang W, Yang J, Yu H, et al. Hybrid plasmonic waveguide crossing based on the multimode interference effect. Opt Commun. 2015;335:86–9.
[50] Su Y, Chang P, Lin C, Helmy AS. Record Purcell factors in ultra-compact hybrid plasmonic ring resonators. Sci Adv. 2019;5:1790.
[51] Khodadadi M, Nozhat N, Moshiri SMM. A high gain and wideband on-chip hybrid plasmonic V-shaped nano-antenna. J Opt. 2020;22:035005.
[52] Hause H, Huang W, Kawakami S, Whitaker N. Coupled-mode theory of optical waveguides. J Lightwave Technol. 1987;5:16–23.
[53] Bellanca G, Orlandi P, Bassi P. Assessment of the orthogonal and non-orthogonal coupled-mode theory for parallel optical waveguide couplers. J Opt Soc Am A. 2018;35:577–85.
[54] Breukelaar IG. Surface plasmon-polaritons in thin metal strips and slabs: Waveguiding and mode cutoff [dissertation]. Ottawa: University of Ottawa; 2004.
[55] Wei W, Zhang X, Ren X. Asymmetric hybrid plasmonic waveguides with centimeter-scale propagation length under subwavelength confinement for photonic components. Nanoscale Res Lett. 2014;9:599.
[56] Ma W, Helmy AS. Asymmetric long-range hybrid-plasmonic modes in asymmetric nanometer-scale structures. J Opt Soc Am B. 2014;31:1723–9.
[57] Wei W, Zhang X, Huang Y, Ren X. Guiding properties of asymmetric hybrid plasmonic waveguides on dielectric substrates. Nanoscale Res Lett. 2014;9:13.
[58] Horvath C, Bachman D, Wu M, Perron D, Van V. Polymer hybrid plasmonic waveguides and microring resonators. IEEE Photon Technol Lett. 2011;23:1267–9.
[59] Avrutsky I, Soref R, Buchwald W. Sub-wavelength plasmonic modes in a conductor-gap-dielectric system with a nanoscale gap. Opt Express. 2010;18:348–63.
[60] Snitzer E. Cylindrical dielectric waveguide modes. J Opt Soc Am. 1961;51:491–8.
[61] Snitzer E, Osterberg H. Observed dielectric waveguide modes in the visible spectrum. J Opt Soc Am. 1961;51:499–505.
[62] Ditlbacher H, Galler N, Koller DM, Hohenau A, Leitner A, Aussenegg FR, et al. Coupling dielectric waveguide modes to surface plasmon polaritons. Opt Express. 2008;16:10455–64.
[63] Haus HA, Huang W. Coupled-mode theory. Proc IEEE. 1991;79:1505–18.
[64] Kou FY, Tamir T. Range extension of surface plasmons by dielectric layers. Opt Lett. 1987;12:367–9.
[65] Tran NHT, Phan BT, Yoon WJ, Khym S, Ju H. Dielectric metal-based multilayers for surface plasmon resonance with enhanced quality factor of the plasmonic waves. J Electron Mater. 2017;46:3654–9.
[66] Berkovitch N, Orenstein M, Lipson SG. Novel complex modes in asymmetrical nanoscale plasmonic waveguides. Opt Express. 2008;16:17842–7.
[67] Breukelaari I, Berini P. Long-range surface plasmon polariton mode cutoff and radiation in slab waveguides. J Opt Soc Am A. 2006;23:1971–7.
[68] Alam MZ, Meier J, Aitchison JS, Mojahedi M. Super mode propagation in low index medium. Proceedings of the Conference on Lasers and Electro-Optics/Quantum Electronics Laser Science Conference and Photonic Applications Systems Technologies. Baltimore, Maryland, USA: Optica Publishing Group; 2007.
[69] Yoshinaga H, Yoheyama T. Design and fabrication of a nonradiative dielectric waveguide circulator. IEEE Trans Microw Theory Tech. 1988;36:1526–9.
[70] Caspers JN, Alam MZ, Mojahedi M. Compact hybrid plasmonic polarization rotator. Opt Lett. 2012;37:4615–7.
[71] Alam MZ, Bahrami F, Aitchison JS, Mojahedi M. Analysis and optimization of hybrid plasmonic waveguide as a platform for biosensing. IEEE Photon J. 2014;6:3700110.
[72] Chen R, Bai B, Zhou Z. Low-loss hybrid plasmonic TM-pass polarizer using polarization-dependent mode conversion. Photon Res. 2020;8:1197–202.
[73] Zhang L, Pan C, Zeng D, Yang Y, Yang Y, Ma J. A hybrid-plasmonic-waveguide-based polarization-independent directional coupler. IEEE Access. 2020;8:134268–75.
[74] Bai B, Pei L, Zheng J, Ning T, Li J. Compact and high extinction ratio TM-pass polarizer utilizing hollow hybrid plasmonic waveguide. Opt Commun. 2019;445:182–6.
[75] Svintsov DA, Arsenin AV, Fedyanin DY. Full loss compensation in hybrid plasmonic waveguides under electrical pumping. Opt Express. 2015;23:19358–75.
[76] Li H, Noh JW, Chen Y, Li M. Enhanced optical forces in integrated hybrid plasmonic waveguides. Opt Express. 2013;21:11839–51.
[77] Wang Z, Dai D, Shi Y, Somesfalean G, Thylen PH, He S, et al. Experimental realization of a low-loss nano-scale Si hybrid plasmonic waveguide. Proceedings of the 2011 Optical Fiber Communication Conference and Exposition and the National Fiber Optic Engineers Conference; 2011 March 6–10. Los Angeles, CA, USA: IEEE; 2011.
[78] Saito H, Kurata H. Formation of a hybrid plasmonic waveguide mode probed by dispersion measurement. J Appl Phys. 2015;117:133107.

[79] Dai D, Shi Y, He S, Wosinski L, Thylen L. Gain enhancement in a hybrid plasmonic nano-waveguide with a low-index or high-index gain medium. Opt Express. 2011;19:12925–36.
[80] Alam MZ, Meier J, Aitchison JS, Mojahedi M. Propagation characteristics of hybrid modes supported by metal-low-high index waveguides and bends. Opt Express. 2010;18:12971–9.
[81] Chen L, Li X, Wang G. A hybrid long-range plasmonic waveguide with sub-wavelength confinement. Opt Commun. 2013;291:400–4.
[82] Chen L, Li X, Wang G, Li W, Chen S, Xiao L, et al. A silicon-based 3-D hybrid long-range plasmonic waveguide for nanophotonic integration. J Lightwave Technol. 2012;30:163–8.
[83] Kim JT. Characteristics analysis of hybrid plasmonic waveguide for low-loss lightwave guiding. Opt Commun. 2011;284:4171–5.
[84] Kim JT, Ju JJ, Park S, Kim MS, Park SK, Shin SY. Hybrid plasmonic waveguide for low-loss lightwave guiding. Opt Express. 2010;18:2808–13.
[85] Xiang C, Wang J. Long-range hybrid plasmonic slot waveguide. IEEE Photon J. 2013;5:4800311.
[86] Noghani MT, Samiei MHV. Propagation characteristics of symmetric and asymmetric multilayer hybrid insulator-metal-insulator and metal-insulator-metal plasmonic waveguides. Adv Electromag. 2014;2:35–43.
[87] Bian Y, Zheng Z, Zhao X, Zhu J, Zhou T. Symmetric hybrid surface plasmon polariton waveguides for 3D photonic integration. Opt Express. 2009;17:21320–5.
[88] Huang CC. Ultra-long-range symmetric plasmonic waveguide for high-density and compact photonic devices. Opt Express. 2013;21:29544–57.
[89] Noghani MT, Samiei MHV. Analysis and optimum design of hybrid plasmonic slab waveguides. Plasmonics. 2013;8:1155–68.
[90] Aldawsari S, Wei L, Liu WK. Theoretical study of hybrid guided modes in a multilayer symmetrical planar plasmonic waveguide. J Lightwave Technol. 2015;33:3198–206.
[91] Kim JT. CMOS-compatible hybrid plasmonic slot waveguide for on-chip photonic circuits. IEEE Photon Technol Lett. 2011;23:1481–3.
[92] Xiao J, Wei QQ, Yang DG, Zhang P, He N, Zhang GQ, et al. A CMOS-compatible hybrid plasmonic slot waveguide with enhanced field confinement. IEEE Electron Device Lett. 2016;37:456–8.
[93] Zhu N. A novel hybrid plasmonic waveguide with loss compensation via electrically pumped gain medium based on silicon platform. Opt Commun. 2013;311:61–4.
[94] Soleimannezhad F, Nikoufard M, Mahdian MA. Low-loss indium phosphide based hybrid plasmonic waveguide. Microw Opt Technol Lett. 2021;63:2242–51.
[95] Sun X, Zhou L, Li X, Hong Z, Chen J. Design and analysis of a phase modulator based on a metal-polymer-silicon hybrid plasmonic waveguide. Appl Opt. 2011;50:3428–34.
[96] Hsieh CH, Chu YT, Huang MJ, Kuo CM, Leou KC. Design of a low loss silicon based hybrid dielectric-loaded plasmonic waveguide and a compact high performance optical resonator. Prog Electromagn Res. 2015;42:135–44.
[97] Zenin VA, Choudhury S, Saha S, Shalaev VM, Boltasseva A, Bozhevolnyi SI. Hybrid plasmonic waveguides formed by metal coating of dielectric ridges. Opt Express. 2017;25:12295–302.
[98] Song Y, Wang J, Yan M, Qiu M. Efficient coupling between dielectric and hybrid plasmonic waveguides by multimode interference power splitter. J Opt. 2011;13:075002.
[99] Dai D, He S. Low-loss hybrid plasmonic waveguide with double low-index nano-slots. Opt Express. 2010;18:17958–66.
[100] Kumar P, Singh DK, Rajan R. Optical performance of hybrid metal-insulator-metal plasmonic waveguide for low-loss and efficient photonic integration. Microw Opt Technol Lett. 2020;62:1489–97.
[101] Manzoor Z, Mirala A, Pak A, Panahi MA. Low loss semi-MIM hybrid plasmonic waveguide with high electric field confinement. Microw Opt Technol Lett. 2019;61:2557–64.
[102] Lu C, Hu X, Yue S, Fu Y, Yang H, Gong Q. Ferroelectric hybrid plasmonic waveguide for all-optical logic gate applications. Plasmonics. 2013;8:749–54.
[103] Kim JT. CMOS-compatible hybrid plasmonic modulator based on vanadium dioxide insulator-metal phase transition. Opt Lett. 2014;39:3997–4000.
[104] Bian Y, Kang L, Ren Q, Zheng Y, Herbert RE, Werner PL, et al. Hybrid vanadate waveguiding configurations for extreme optical confinement and efficient polarization management in the near-infrared. Nanoscale. 2018;10:16667–74.
[105] Dinh CQ, Oshima A, Tagawa S. Depth dependence of time delay effect on hydrogen silsesquioxane (HSQ) resist layers. J Photopolym Sci Technol. 2012;25:121–4.
[106] Henschel W, Georgiev YM, Kurz H. Study of a high contrast process for hydrogen silsesquioxane as a negative tone electron beam resist. J Vac Sci Technol B. 2003;21:2018–25.
[107] Lanniel M, Lu B, Chen Y, Allen S, Buttery L, Williams P, et al. Patterning the mechanical properties of hydrogen silsesquioxane films using electron beam irradiation for application in mechano cell guidance. Thin Solids Film. 2011;519:2003–10.
[108] Leon ID, Berini P. Modeling surface plasmon-polariton gain in planar metallic structures. Opt Express. 2009;17:20191–202.
[109] Grandidier J, des Francs GC, Massenot S, Bouhelier A, Markey L, Weeber JC, et al. Gain-assisted propagation in a plasmonic waveguide at telecom wavelength. Nano Lett. 2009;9:2935–9.
[110] Nezhad M, Tetz K, Fainman Y. Gain assisted propagation of surface plasmon polaritons on planar metallic waveguides. Opt Express. 2004;12:4072–9.
[111] Pavesi L, Dal Negro L, Mazzoleni C, Franzò G, Priolo F. Optical gain in silicon nanocrystals. Nature. 2000;408:440–4.
[112] Oulton RF, Sorger VJ, Zentgraf T, Ma RM, Gladden C, Dai L, et al. Plasmon lasers at deep subwavelength scale. Nature. 2009;461:629–32.
[113] Sorger VJ, Ye Z, Oulton RF, Wang Y, Bartal G, Yin X, et al. Experimental demonstration of low-loss optical waveguiding at deep sub-wavelength scales. Nat Commun. 2011;2:331.
[114] Oulton RF, Sorger VJ, Genov DA, Pile DFP, Zhang X. A hybrid plasmonic waveguide for subwavelength confinement and long-range propagation. Nat Photon. 2008;2:496–500.
[115] Yang X, Liu Y, Oulton RF, Yin X, Zhang X. Optical forces in hybrid plasmonic waveguides. Nano Lett. 2011;11:321–8.
[116] Huang C, Zhu L. Enhanced optical forces in 2D hybrid and plasmonic waveguides. Opt Lett. 2010;35:1563–5.
[117] Povinelli ML, Loncar M, Ibanescu M, Smythe EJ, Johnson SG, Capasso F, et al. Evanescent-wave bonding between optical waveguides. Opt Lett. 2005;30:3042–4.
[118] Fong KY, Pernice WHP, Li M, Tang HX. Tunable optical coupler controlled by optical gradient forces. Opt Express. 2011;19:15098–108.
[119] Li M, Pernice WHP, Xiong C, Baehr-Jones T, Hochberg M, Tang HX. Harnessing optical forces in integrated photonic circuits. Nature. 2008;456:480–4.

[120] Li M, Pernice WHP, Tang HX. Tunable bipolar optical interactions between guided lightwaves. Nat Photon. 2009;3:464–8.
[121] Chu HS, Li EP, Bai P, Hegde R. Optical performance of single-mode hybrid dielectric-loaded plasmonic waveguide-based components. Appl Phys Lett. 2010;96:221103.
[122] Krasavin AV, Zayats AV. Silicon-based plasmonic waveguides. Opt Express. 2010;18:11791–9.
[123] Morita M, Ohmi T, Hasegawa E, Kawakami M, Ohwada M. Growth of native oxide on a silicon surface. J Appl Phys. 1990;68:1272–81.
[124] Kubota H, Kawai A. Native oxide growth on Si (100) surface in liquid environment. J Photopolym Sci Technol. 2007;20:823–4.
[125] Khodadadi M, Nozhat N. Theoretical analysis of a super-mode waveguide and design of a complementary triangular hybrid plasmonic nano-antenna. IEEE J Sel Top Quant Electron. 2021;27:4600210.
[126] Jeong CY, Kim M, Kim S. Circular hybrid plasmonic waveguide with ultra-long propagation distance. Opt Express. 2013;21:17404–12.
[127] Zhao Y, Zhu L. Coaxial hybrid plasmonic nanowire waveguides. J Opt Soc Am B. 2010;27:1260–5.
[128] Xu J, Shi N, Chen Y, Lu X, Wei H, Lu Y, et al. TM_{01} mode in a cylindrical hybrid plasmonic waveguide with large propagation length. Appl Opt. 2018;57:4043–7.
[129] Sun M, Tian J, Li L. Mode properties of a coaxial multi-layer hybrid surface plasmon waveguide. Phys Status Solidi B. 2015;252:1884–9.
[130] Bian Y, Zheng Z, Zhao X, Su Y, Liu L, Liu J, et al. Guiding of long-range hybrid plasmon polariton in a coupled nanowire array at deep-subwavelength scale. IEEE Photon Technol Lett. 2012;24:1279–81.
[131] Chen D. Cylindrical hybrid plasmonic waveguide for subwavelength confinement of light. Appl Opt. 2010;49:6868–71.
[132] Khodadadi M, Nozhat N, Moshiri SMM. Theoretical analysis of a circular hybrid plasmonic waveguide to design a hybrid plasmonic nano-antenna. Sci Rep. 2020;10:15122.
[133] Takahara J, Yamagishi S, Taki H, Morimoto A, Kobayashi T. Guiding of a one-dimensional optical beam with nanometer diameter. Opt Lett. 1997;22:475–7.
[134] Ditlbacher H, Hohenau A, Wagner D, Kreibig U, Rogers M, Hofer F, et al. Silver nanowires as surface plasmon resonators. Phys Rev Lett. 2005;95:257403.
[135] Manjavacas A, de Abajo FJG. Robust plasmon waveguides in strongly interacting nanowire arrays. Nano Lett. 2009;9:1285–9.
[136] Jamshidi A, Pauzauskie PJ, Schuck PJ, Ohta AT, Chiou PY, Chou J, et al. Dynamic manipulation and separation of individual semiconducting and metallic nanowires. Nat Photon. 2008;2:86–9.
[137] Sugimura A. Band-to-band Auger recombination effect on InGaAsP laser threshold. IEEE J Quant Electron. 1981;17:627–35.
[138] Laroche T, Girard C. Near-field optical properties of single plasmonic nanowires. Appl Phys Lett. 2006;89:233119.
[139] Wang J, Guo YX, Huang BH, Gao SP, Xia YS. A silicon-based hybrid plasmonic waveguide for nano-scale optical confinement and long range propagation. IEEE Trans Nanotechnol. 2019;18:437–44.
[140] Lu Z, Shu Y. Modified hybrid plasmonic waveguides as tunable optical tweezers. Chin Phys Lett. 2013;30:034208.
[141] Bian Y, Gong Q. Low-loss hybrid plasmonic modes guided by metal-coated dielectric wedges for subwavelength light confinement. Appl Opt. 2013;52:5733–41.
[142] Jiang Y, Shi C, Wang J. A hybrid plasmonic terahertz waveguide with ridge structure base on Bulk-Dirac-semimetal. Opt Commun. 2020;475:126239.
[143] Huong NT, Vy ND, Trinh MT, Hoang CM. Tuning SPP propagation length of hybrid plasmonic waveguide by manipulating evanescent field. Opt Commun. 2020;462:125335.
[144] Ma Y, Farrell G, Semenova Y, Wu Q. A hybrid wedge-to-wedge plasmonic waveguide with low loss propagation and ultra-deep-nanoscale mode confinement. J Lightwave Technol. 2015;33:3827–35.
[145] Bian Y, Zheng Z, Zhao X, Liu L, Su Y, Liu J, et al. Hybrid plasmon polariton guiding with tight mode confinement in a V-shaped metal/dielectric groove. J Opt. 2013;15:055011.
[146] Zhang J, Cai L, Bai W, Xu Y, Song G. Hybrid plasmonic waveguide with gain medium for lossless propagation with nanoscale confinement. Opt Lett. 2011;36:2312–4.
[147] Bian Y, Zheng Z, Yang P, Xiao J, Wang G, Liu L, et al. Silicon-slot mediated guiding of plasmonic modes: realization of subwavelength optical confinement with low propagation loss. IEEE J Sel Quant Electron. 2013;20:8100108.
[148] Bian Y, Gong Q. Bow-tie hybrid plasmonic waveguides. J Lightwave Technol. 2014;32:3902–7.
[149] Chen ZX, Wu ZJ, Ming Y, Zhang XJ, Lu YQ. Hybrid plasmonic waveguide in a metal V-groove. AIP Adv. 2014;4:017103.
[150] Bian Y, Zheng Z, Liu Y, Liu J, Zhu J, Zhou T. Hybrid wedge plasmon polariton waveguide with good fabrication-error-tolerance for ultra-deep-subwavelength mode confinement. Opt Express. 2011;19:22417–22.
[151] Ding L, Qin J, Xu K, Wang L. Long range hybrid tube-wedge plasmonic waveguide with extreme light confinement and good fabrication error tolerance. Opt Express. 2016;24:3432–40.
[152] Zhang Z, Wang J. Long-range hybrid wedge plasmonic waveguide. Sci Rep. 2014;4:6870.
[153] Bian Y, Zheng Z, Zhao X, Su Y, Liu L, Liu J, et al. Highly confined hybrid plasmonic modes guided by nanowire-embedded-metal grooves for low-loss propagation at 1550 nm. IEEE J Sel Quant Electron. 2013;19:4800106.
[154] Eldilo M, Ma Y, Che F, Maeda H, Cada M. A THz semiconductor hybrid plasmonic waveguide with fabrication-error tolerance. Japanese J Appl Phys. 2017;56:010306.
[155] He XY, Wang QJ, Yu SF. Numerical study of gain-assisted terahertz hybrid plasmonic waveguide. Plasmonics. 2012;7:571–7.
[156] Li ZQ, Wang Y, He J, Feng D, Gu E, Li W. An ultraviolet hybrid plasmonic waveguide for nanolaser applications. Opt Photon J. 2016;6:19–23.
[157] Zheng K, Zheng X, Dai Q, Song Z. Hybrid rib-slot-rib plasmonic waveguide with deep-subwavelength mode confinement and long propagation length. AIP Adv. 2016;6:085012.
[158] Tian J, Sun M. Modal properties of novel hybrid plasmonic waveguide consisting of two identical dielectric nanotubes symmetrically placed on both sides of a thin metal film. Eur Phys J D. 2016;70:4.
[159] Chen L, Zhang T, Li X, Huang W. Novel hybrid plasmonic waveguide consisting of two identical dielectric nanowires symmetrically placed on each side of a thin metal film. Opt Express. 2012;20:20535–44.
[160] Bian Y, Zheng Z, Zhao X, Liu L, Su Y, Liu J, et al. Nanoscale light guiding in a silicon-based hybrid plasmonic waveguide that incorporates an inverse metal ridge. Phys Status Solidi A. 2013;210:1424–8.

[161] Ashkin A, Dziedzic JM, Bjorkholm JE, Chu S. Observation of a single-beam gradient force optical trap for dielectric particles. Opt Lett. 1986;11:288–90.
[162] Chu S. Laser manipulation of atoms and particles. Science. 1991;253:861–6.
[163] Monica C, Capitanio M, Belcastro G, Vanzi F, Pavone FS. Optical methods to study protein-DNA interactions in vitro and in living cells at the single-molecule level. Int J Mol Sci. 2013;14:3961–92.
[164] Perkins T, Ouake SR, Smith DE, Chu S. Relaxation of a single DNA molecule observed by optical microscopy. Science. 1994;264:822–6.
[165] Carmon G, Feingold M. Rotation of single bacterial cells relative to the optical axis using optical tweezers. Opt Lett. 2011;36:40–2.
[166] Lu Q, Zou CL, Chen D, Zhou P, Wu G. Extreme light confinement and low loss in triangle hybrid plasmonic waveguide. Opt Commun. 2014;319:141–6.
[167] Amarloo H, Safavi-Naeini S. Slot plasmonic waveguide based on doped-GaAs for terahertz deep-subwavelength applications. J Opt Soc Am A. 2015;32:2189–94.
[168] Li S, Jadidi MM, Murphy TE, Kumar G. Terahertz surface plasmon polaritons on a semiconductor surface structured with periodic V-grooves. Opt Express. 2013;21:7041–9.
[169] Gargas DJ, Toimil-Molares ME, Yang PD. Imaging single ZnO vertical nanowire laser cavities using UV-laser scanning confocal microscopy. J Am Chem Soc. 2009;131:2125–7.
[170] Tarcea N, Harz M, Rosch P, Frosch T, Schmitt M, Thiele H, et al. Raman spectroscopy-A technique for biological and mineralogical in situ planetary studies. Spectrochimica Acta Part A. 2007;68:1029–35.
[171] Moshiri SMM, Khodadadi M, Nozhat N. Theoretical analysis of ultra-fast multi-wavelength switch containing Kerr nonlinear material and its application as simultaneous AND and NOR logic gates. Appl Opt. 2020;59:6030–40.
[172] Diaz FJ, Li G, de Sterke CM, Kuhlmey BT, Palomba S. Kerr effect in hybrid plasmonic waveguides. J Opt Soc Am B. 2016;33:957–62.
[173] Leuthold J, Koos C, Freude W. Nonlinear silicon photonics. Nat Photon. 2010;4:535–44.
[174] Firouzabadi MD, Nikoufard M, Tavakoli MB. An investigation on shallow-etched InP-based hybrid nanoplasmonic waveguides for nonlinear applications. J Comput Electron. 2020;19:849–53.
[175] Firouzabadi MD, Nikoufard M, Tavakoli MB. Modifying the figure of merit in hybrid plasmonic waveguide for Kerr nonlinear effect. Indian J Phys. 2020;94:713–8.
[176] Aldawsari S, West BR. Hybrid plasmonic waveguides for nonlinear applications. Proceedings of 2012 Photonics Global Conference (PGC); 2012 Dec 13–16. Singapore: IEEE; 2012.
[177] Pitilakis A, Kiezis EE. Highly nonlinear hybrid silicon-plasmonic waveguides: analysis and optimization. J Opt Soc Am B. 2013;30:1954–65.
[178] Koos C, Vorreau P, Vallaitis T, Dumon P, Bogaerts W, Beats R, et al. All-optical high-speed signal processing with silicon–organic hybrid slot waveguides. Nat Photon. 2009;3:216–9.
[179] Diaz FJ, Hatakeyama T, Rho J, Wang Y, O'Brien K, Zhang X, et al. Sensitive method for measuring third order nonlinearities in compact dielectric and hybrid plasmonic waveguides. Opt Express. 2016;24:545–54.
[180] Tu Z, Jin Q, Li X, Gao S. Mid-infrared nonlinear silicon hybrid waveguide with high figure of merit. J Opt Soc Am B. 2018;35:1772–9.
[181] Jin Q, Li X, Chen J, Gao S. Ultra-broadband nonlinearity enhancement based on a novel graphene-silicon hybrid waveguide: structure design and theoretical analysis. Sci Rep. 2017;7:12290.
[182] Tuniz A, Bickerton O, Diaz FJ, Käsebier T, Kley EB, Kroker S, et al. Modular nonlinear hybrid plasmonic circuit. Nat Commun. 2020;11:2413.
[183] Shi J, Li Y, Kang M, He X, Halas NJ, Nordlander P, et al. Efficient second harmonic generation in a hybrid plasmonic waveguide by mode interactions. Nano Lett. 2019;19:3838–45.
[184] Dai J, Zhang M, Zhou F, Wang Y, Lu L, Liu D. All-optical logic operation of polarized light signals in highly nonlinear silicon hybrid plasmonic microring resonators. Appl Opt. 2015;54:4471–7.
[185] Li G, de Sterke CM, Palomba S. Figure of merit for Kerr nonlinear plasmonic waveguides. Laser Photon Rev. 2016;10:639–46.
[186] Firouzabadi MD, Nikoufard M, Tavakoli MB. Optical Kerr nonlinear effect in InP-based hybrid plasmonic waveguides. Opt Quant Electron. 2017;49:390.
[187] Sharma T, Wang J, Cheng Z, Yu K, Gangwar P, Kumar V, et al. Low loss hybrid plasmonic waveguide with variable nonlinearity and ultralow dispersion. Plasmonics. 2022;17:2161–71.
[188] Zhang J, Cassan E, Gao D, Zhang X. Highly efficient phase-matched second harmonic generation using an asymmetric plasmonic slot waveguide configuration in hybrid polymer-silicon photonics. Opt Express. 2013;21:14876–87.
[189] Rahimi H, Nikoufard M, Firouzabadi MD. Kerr nonlinear effect in the graphene-based wedged hybrid plasmonic waveguide. Opt Quant Electron. 2024;56:811.
[190] Hatami M, Nikoufard M, Firouzabadi MD. Graphene-integrated hybrid plasmonic waveguide for Kerr nonlinear application. J Nonlinear Opt Phys Mater. 2025;34:2350092.
[191] Zhou X, Zhang T, Chen L, Hong W, Li X. A graphene-based hybrid plasmonic waveguide with ultra-deep subwavelength confinement. J Lightwave Technol. 2014;32:3597–601.
[192] Hu X, Wang J. High figure of merit graphene modulator based on long-range hybrid plasmonic slot waveguide. IEEE J Quant Electron. 2017;53:7200308.
[193] Vahed H, Ahmadi SS. Hybrid plasmonic optical modulator based on multi-layer graphene. Opt Quant Electron. 2020;52:2.
[194] He X, Ning T, Lu S, Zheng J, Li J, Li R, et al. Ultralow loss graphene-based hybrid plasmonic waveguide with deep-subwavelength confinement. Opt Express. 2018;26:10109–18.
[195] Chen M, Sheng P, Sun W, Cai J. A symmetric terahertz graphene-based hybrid plasmonic waveguide. Opt Commun. 2016;376:41–6.
[196] Ye L, Sui K, Liu Y, Zhang M, Huo LQ. Graphene-based hybrid plasmonic waveguide for highly efficient broadband mid-infrared propagation and modulation. Opt Express. 2018;26:15935–47.
[197] Gosciniak J, Tan DTH. Theoretical investigation of graphene-based photonic modulators. Sci Rep. 2013;3:1897.
[198] Wu J, Guo S, Li Z, Li X, Xue H, Wang Z. Graphene hybrid surface plasmon waveguide with low loss transmission. Plasmonics. 2020;15:1621–7.
[199] Yousefi L, Foster AC. Waveguide-fed optical hybrid plasmonic patch nano-antenna. Opt Express. 2012;20:18326–35.
[200] Sharma P, Kumar VD. Multilayer hybrid plasmonic nano patch antenna. Plasmonics. 2019;14:435–40.
[201] Saad-Bin-Alam M, Khalil MI, Rahman A, Chowdhury AM. Hybrid plasmonic waveguide fed broadband nanoantenna for nano-photonic applications. IEEE Photon Technol Lett. 2015;27:1092–5.

[202] Nikoufard M, Nourmohammadi A, Esmaeili S. Hybrid plasmonic nanoantenna with the capability of monolithic integration with laser and photodetector on InP substrate. IEEE Trans Antennas Propag. 2018;66:3–8.
[203] Khodadadi M, Nozhat N, Moshiri SMM. Analytic approach to study a hybrid plasmonic waveguide-fed and numerically design a nano-antenna based on the new director. Opt Express. 2020;28:3305–30.
[204] Nourmohammadi A, Nikoufard M. Ultra-wideband photonic hybrid plasmonic horn nanoantenna with SOI configuration. Silicon. 2020;12:193–8.
[205] Altug H, Oh S, Maier SA, Homola J. Advances and applications of nanophotonic biosensors. Nat Nanotechnol. 2022;17:5–16.
[206] Murai S, Verschuuren MA, Lozano G, Pirruccio G, Rodriguez SRK, Rivas JG. Hybrid plasmonic-photonic modes in diffractive arrays of nanoparticles coupled to light-emitting optical waveguides. Opt Express. 2013;21:4250–62.
[207] Zhang Q, Li G, Liu X, Qian F, Li Y, Sum TC, et al. A room temperature low-threshold ultraviolet plasmonic nanolaser. Nat Commun. 2014;5:4953.
[208] Khodadadi M, Moshiri SMM, Nozhat N, Khalily M. Controllable hybrid plasmonic integrated circuit. Sci Rep. 2023;13:9983.
[209] Gosciniak J, Khurgin JB. On-chip ultrafast plasmonic graphene hot electron bolometric photodetector. ACS Omega. 2020;5:14711–9.
[210] Watts MR, Haus HA, Ippen EP. Integrated mode-evolution-based polarization splitter. Opt Lett. 2005;30:967–9.
[211] Tan Q, Huang X, Zhou W, Yang K. A plasmonic based ultracompact polarization beam splitter on silicon-on-insulator waveguides. Sci Rep. 2013;3:2206.
[212] Sun X, Alam MZ, Wagner SJ, Aitchison JS, Mojahedi M. Experimental demonstration of a hybrid plasmonic transverse electric pass polarizer for a silicon-on-insulator platform. Opt Lett. 2012;37:4814–6.
[213] Guan X, Wu H, Shi Y, Wosinski L, Dai D. Ultracompact and broadband polarization beam splitter utilizing the evanescent coupling between a hybrid plasmonic waveguide and a silicon nanowire. Opt Lett. 2013;38:3005–8.
[214] Lu M, Deng C, Zheg P, Liu P, Lin D, Hu G, et al. Ultra-compact TE-mode-pass power splitter based on subwavelength gratings and hybrid plasmonic waveguides on SOI platform. Opt Commun. 2021;498:127250.
[215] Alam MZ, Aitchison JS, Mojahedi M. Compact hybrid TM-pass polarizer for silicon-on-insulator platform. Appl Opt. 2011;50:2294–8.
[216] Zhang L, Liu J, Pan C, Yang Y. An ultra-compact broadband polarizing beam splitter utilizing hybrid plasmonic waveguide. China Commun. 2023;20:49–59.
[217] Dizaj LS, Abbasian K, Nurmohammadi T. A three-core hybrid plasmonic polarization splitter designing based on the hybrid plasmonic waveguide for utilizing in optical integrated circuits. Plasmonics. 2020;15:2213–21.
[218] Chee J, Zhu S, Lo GQ. CMOS compatible polarization splitter using hybrid plasmonic waveguide. Opt Express. 2012;20:25345–55.
[219] Guan X, Wu H, Shi Y, Dai D. Extremely small polarization beam splitter based on a multimode interference coupler with a silicon hybrid plasmonic waveguide. Opt Lett. 2014;39:259–62.
[220] Hu T, Qiu H, Zhang Z, Guo X, Liu C, Rouifed MS, et al. A compact ultrabroadband polarization beam splitter utilizing a hybrid plasmonic Y-branch. IEEE Photon J. 2016;8:4802209.
[221] Dai D, Wang Z, Peters J, Bowers JE. Compact polarization beam splitter using an asymmetrical Mach–Zehnder interferometer based on silicon-on-insulator waveguides. IEEE Photon Technol Lett. 2012;24:673–5.
[222] Qiu H, Su Y, Yu P, Hu T, Yang J, Jiang X. Compact polarization splitter based on silicon grating-assisted couplers. Opt Lett. 2015;40:1885–7.
[223] Hu T, Rouifed MS, Qiu H, Guo X, Littlejohns CG, Liu C. A polarization splitter and rotator based on a partially etched grating-assisted coupler. IEEE Photon Technol Lett. 2016;28:911–4.
[224] Zhang Y, He Y, Wu J, Jiang X, Liu R, Qui C, et al. High-extinction-ratio silicon polarization beam splitter with tolerance to waveguide width and coupling length variations. Opt Express. 2016;24:6586–93.
[225] Xu Y, Xiao J. Compact and high extinction ratio polarization beam splitter using subwavelength grating couplers. Opt Lett. 2016;41:773–6.
[226] Shen B, Wang P, Polson R, Menon R. An integrated-nophotonics polarization beamsplitter with 2.4 × 2.4 μm^2 footprint. Nat Photon. 2015;9:378–82.
[227] Gao L, Hu F, Wang X, Tang L, Zhou Z. Ultracompact and silicon-on-insulator-compatible polarization splitter based on asymmetric plasmonic–dielectric coupling. Appl Phys B. 2013;113:199–203.
[228] Kim S, Qi M. Copper nanorod array assisted silicon waveguide polarization beam splitter. Opt Express. 2014;22:9508–16.
[229] Ma Y, Farrell G, Semenova Y, Chan HP, Zhang H, Wu Q. Low loss, high extinction ration and ultra-compact plasmonic polarization beam splitter. IEEE Photon Technol Lett. 2014;26:660–3.
[230] Caspers JN, Aitchison JS, Mojahedi M. Experimental demonstration of an integrated hybrid plasmonic polarization rotator. Opt Lett. 2013;38:4054–7.
[231] Abu-Elmaaty BE, Shalaby HMH. Highly efficient silicon mode converter and polarization rotator using a silicon-based hybrid plasmonic waveguide. J Opt Soc Am B. 2023;40:2789–95.
[232] Li X, Tao J, Zhao Y, Dai S, Wang W, Li J, et al. Ultra-compact, broadband polarization beam splitter based on x-cut lithium-niobate-on-insulator platform using hybrid plasmonic waveguide. Opt Commun. 2023;545:129629.
[233] Deng C, Lu M, Sun Y, Huang L, Wang D, Hu G, et al. Broadband and compact polarization beam splitter in LNOI hetero-anisotropic metamaterials. Opt Express. 2021;29:11627–34.
[234] Zhang L, Zhang L, Fu X, Yang L. Compact, broadband and low-loss polarization beam splitter on lithium-niobate-on-insulator using a silicon nanowire assisted waveguide. IEEE Photon J. 2020;12:6601906.
[235] Xu H, Dai D, Liu L, Shi Y. Proposal for an ultra-broadband polarization beam splitter using an anisotropy-engineered Mach-Zehnder interferometer on the x-cut lithium-niobate-on-insulator. Opt Express. 2020;28:10899–908.
[236] Yang G, Sergienko AV, Ndao A. Plasmonic loss-mitigating broadband adiabatic polarizing beam splitter. Opt Lett. 2022;47:629–32.
[237] Khodadadi M, Nozhat N, Moshiri SMM. Theoretical analysis of a graphene quantum well hybrid plasmonic waveguide to design an inter/intra-chip nano-antenna. Carbon. 2022;189:443–58.
[238] Xu Z, Sun X. Ultra-broadband TE-pass polarizer based on hybrid plasmonic-assisted contra-directional couplers. J Opt Soc Am B. 2020;37:251–6.
[239] Park J, Zhang S, She A, Chen WT, Lin P, Yousef KMA, et al. All-glass, large metalens at visible wavelength using deep-ultraviolet projection lithography. Nano Lett. 2019;19:8673–82.

[240] Shi Y, Kunert B, Koninck YD, Pantouvaki M, Campenhout JV, Thourhout DV. Novel adiabatic coupler for III-V nano-ridge laser grown on a Si photonics platform. Opt Express. 2019;27:37781–94.
[241] Kim S, Qi M. Mode-evolution-based polarization rotation and coupling between silicon and hybrid plasmonic waveguides. Sci Rep. 2015;5:18378.
[242] Shi P, Zhou G, Chau FS. Enhanced coupling efficiency between dielectric and hybrid plasmonic waveguides. J Opt Soc Am B. 2013;30:1426–31.
[243] Ahmadivand A. Hybrid photonic–plasmonic polarization beam splitter (HPPPBS) based on metal-silica-silicon interactions. Opt Laser Technol. 2014;58:145–50.
[244] Sorger VJ, Lanzillotti-Kimura ND, Ma RM, Zhang X. Ultra-compact silicon nanophotonic modulator with broadband response. Nanophoton. 2012;1:17–22.
[245] Chelladurai D, Doderer M, Koch U, Fedoryshyn Y, Haffner C, Leuthold J. Low-loss hybrid plasmonic coupler. Opt Express. 2019;27:11862–68.
[246] Tan H, Liu W, Zhang Y, Yin S, Dai D, Gao S, et al. High-efficiency broadband grating couplers for silicon hybrid plasmonic waveguides. Photonics. 2022;9:550.
[247] Nikoufard M, Heydari N, Pourgholi S, Khomami AR. Novel hybrid plasmonic-based directional coupler on InP substrate. Photonics Nanostruct Fundam Appl. 2016;22:9–17.
[248] Zeng D, Zhang L, Xiong Q, Ma J. Directional coupler based on an elliptic cylindrical nanowire hybrid plasmonic waveguide. Appl Opt. 2018;57:4701–6.
[249] Nia BA, Yousefi L, Shahabadi M. Integrated optical-phased array nanoantenna system using a plasmonic Rotman lens. J Lightwave Technol. 2016;34:2118–26.
[250] Ashkin A. Acceleration and trapping of particles by radiation pressure. Phys Rev Lett. 1970;24:156–9.
[251] Liu V, Povinelli M, Fan S. Resonance-enhanced optical forces between coupled photonic crystal slabs. Opt Express. 2009;17:21897–909.
[252] Khodadadi M, Moshiri SMM, Nozhat N. Theoretical analysis of a simultaneous graphene-based circular plasmonic refractive index and thickness bio-sensor. IEEE Sens J. 2020;20:9114–23.
[253] Guo C, Wang C, Ma T, Wang F. Ultra-compact and highly sensitive refractive index sensor based on a chalcogenide suspended slot hybrid plasmonic microring resonator. Optik. 2023;274:170595.
[254] Lou F, Thylen L, Wosinski L. Hybrid plasmonic microdisk resonators for optical interconnect applications. Proceedings of SPIE 8781, Integrated Optics: Physics and Simulations; 2013 May 7. Prague, Czech Republic: SPIE; 2013. p. 87810X.
[255] Butt MA. Racetrack ring resonator-based on hybrid plasmonic waveguide for refractive index sensing. Micromachines. 2024;15:610.
[256] Tang L, Hu F, Yi H, Zhou Z. Ultracompact racetrack resonators based on hybrid plasmonic waveguides. Proceedings of SPIE 8564, Nanophotonics and Micro/Nano Optics; 2012 Nov 20. Beijing, China: SPIE; 2012. p. 856417.
[257] Li Z, Jin J, Yang F, Song N, Yin Y. Coupling magnetic and plasmonic anisotropy in hybrid nanorods for mechanochromic responses. Nat Commun. 2020;11:2883.
[258] Paudel HP, Safaei A, Leuenberger MN. Nanoplasmonics in metallic nanostructures and Dirac systems. In: Barbillon G, editor. Nanoplasmonics-fundamentals and applications. Croatia: InTech; 2017. p. 49–94.
[259] Krasnok AE, Miroshnichenko AE, Belov PA, Kivshar Y. All-dielectric optical nanoantennas. Opt Express. 2012;20:20599–604.
[260] Khurgin JB. How to deal with the loss in plasmonics and metamaterials. Nat Nanotechnol. 2015;10:2–6.
[261] Pavliuk MV, Fernandes AB, Abdellah M, Fernandes DLA, Machado CO, Rocha L, et al. Nano-hybrid plasmonic photocatalyst for hydrogen production at 20% efficiency. Sci Rep. 2017;7:8670.
[262] Joushaghani A, Kruger BA, Paradis S, Alain D, Aitchison JS, Poon JKS. Sub-volt broadband hybrid plasmonic-vanadium dioxide switches. Appl Phys Lett. 2013;102:061101.
[263] Ooi KJA, Bai P, Chu HS, Ang LK. Ultracompact vanadium dioxide dual-mode plasmonic waveguide electroabsorption modulator. Nanophoton. 2013;2:13–9.
[264] Li F, Xu M, Hu X, Wu J, Wang T, Su Y. Monolithic silicon-based 16-QAM modulator using two plasmonic phase shifters. Opt Commun. 2013;286:166–70.
[265] Ansell D, Radko IP, Han Z, Rodriguez FJ, Bozhevolnyi SI, Grigorenko AN. Hybrid graphene plasmonic waveguide modulators. Nat Commun. 2015;6:8846.
[266] Bai B, Liu L. Zhou Z. Ultracompact, high extinction ratio polarization beam splitter-rotator based on hybrid plasmonic-dielectric directional coupling. Opt Lett. 2017;42:4752–5.
[267] Bai B, Deng Q, Zhou Z. Plasmonic-assisted polarization beam splitter based on bent directional coupling. IEEE Photonics Technol Lett. 2017;29:599–602.
[268] Lou F, Dai D, Wosinski L. Ultracompact polarization beam splitter based on a dielectric-hybrid plasmonic-dielectric coupler. Opt Lett. 2012;37:3372–4.
[269] Zhou D, Zheng F, Wu X, Li J, Jia Q. Ultracompact polarization beam splitter based on hybrid plasmonic waveguide. J Mod Opt. 2024;71:288–94.
[270] Chang KW, Huang CC. Ultrashort broadband polarization beam splitter based on a combined hybrid plasmonic waveguide. Sci Rep. 2016;6:19609.
[271] Sun B, Chen MY, Zhang YK, Zhou J. An ultracompact hybrid plasmonic waveguide polarization beam splitter. Appl Phys B. 2013;113:179–83.
[272] Nikufard M, Khomami AR. Hybrid plasmonic polarization splitter using three-waveguide directional coupler in InGaAsP/InP. Opt Quantum Electron. 2016;48:576.
[273] Tian J, Ma Z, Li Q, Song Y, Liu Z, Yang Q, et al. Nanowaveguides and couplers based on hybrid plasmonic modes. Appl Phys Lett. 2010;97:231121.
[274] Lou F, Wang Z, Dai D, Thylen L, Wosinski L. Experimental demonstration of ultra-compact directional couplers based on silicon hybrid plasmonic waveguides. Appl Phys Lett. 2012;100:241105.
[275] Alam MZ, Aitchison JS, Mojahedi M. Polarization-independent hybrid plasmonic coupler for a silicon on insulator platform. Opt Lett. 2012;37:3417–9.
[276] Du CH, Chiou YP. Vertical directional couplers with ultra-short coupling length based on hybrid plasmonic waveguides. J Lightwave Technol. 2014;32:2065–71.
[277] Nayak JK, Roy Chaudhuri P, Sahoo PK. Stable hybrid plasmonic directional coupler based on an embedded silver nanostructure waveguide. Appl Opt. 2021;60:7603–10.
[278] Li Q, Qiu M. Structurally-tolerant vertical directional coupling between metal-insulator-metal plasmonic waveguide and silicon dielectric waveguide. Opt Express. 2010;18:15531–43.

[279] Yu W, Tian Y, Zhang S, Tan W. Arbitrary power-splitting-ratio achieved in 1 × 2 hybrid plasmonic multimode interference device by structure symmetry broken. Optik. 2020;220:165141.
[280] Nikoufard M, Alamouti MK, Pourgholi S. Multimode interference power-splitter using InP-based deeply etched hybrid plasmonic waveguide. IEEE Trans Nanotechnol. 2017;16:477–83.
[281] Kumari S, Tripathi SM. Hybrid plasmonic SOI ring resonator for bulk and affinity bio-sensing applications. Silicon. 2022;14:11577–86.
[282] Butt MA, Kozlowski L, Pirmidowicz R. Optimized hybrid plasmonic waveguide-based ring resonator for advanced refractive index sensing. J Opt. 2024;26:075802.
[283] Ou X, Yang Y, Sun F, Zhang P, Tang B, Li B, et al. Li Z. Wide-range, ultra-compact, and high-sensitivity ring resonator biochemical sensor with CMOS-compatible hybrid plasmonic waveguide. Opt Express. 2021;29:19058–67.
[284] Adhikari R, Sbeah Z, Chauhan D, Chang SH, Dwivedi RP. A voyage from plasmonic to hybrid waveguide refractive index sensors based on wavelength interrogation technique: a review. Braz J Phys. 2022;52:564–77.
[285] Chen Y, Bi K, Wang Q, Zheng M, Liu Q, Han Y, et al. Rapid focused ion beam milling based fabrication of plasmonic nanoparticles and assemblies via “sketch and peel” strategy. ACS Nano. 2016;10:11228–36.
[286] Lin S, Hammood M, Yun H, Luan E, Jaeger NAF, Chrostowski L. Computational lithography for silicon photonics design. IEEE J Sel Top Quant Electron. 2020;26:8201408.
[287] Guo J, Li J, Liu C, Yin Y, Wang W, Ni Z, et al. High-performance silicon–graphene hybrid plasmonic waveguide photodetectors beyond 1.55 μm. Light: Sci Appl. 2020;9:29.
[288] Wu Z, Xu Y. Design of a graphene-based dual-slot hybrid plasmonic electro-absorption modulator with high-modulation efficiency and broad optical bandwidth for on-chip communication. Appl Opt. 2018;57:3260–7.
[289] Dowling L, Kennedy J, O’Shaughnessy S, Trimble D. A review of critical repeatability and reproducibility issues in powder bed fusion. Mater Des. 2020;186:108346.
[290] Barnes WL, Dereux A, Ebbesen TW. Surface plasmon subwavelength optics. Nature. 2003;424:824–30.
[291] Kumari S, Gupta S. Performance estimation of hybrid plasmonic waveguide in presence of stress. Plasmonics. 2021;16:359–70.
[292] Veronis G, Fan S. Modes of subwavelength plasmonic slot waveguides. J Lightwave Technol. 2007;25:2511–21.
[293] Maier SA, Kik PG, Atwater HA, Meltzer S, Harel E, Koel BE, et al. Local detection of electromagnetic energy transport below the diffraction limit in metal nanoparticle plasmon waveguides. Nat Mater. 2003;2:229–32.
[294] Tame MS, McEnery KR, Özdemir ŞK, Lee J, Maier SA, Kim MS. Quantum plasmonics. Nat Phys. 2013;9:329–40.
[295] Huang M. Stress effects on the performance of optical waveguides. Int J Solids Struct. 2003;40:1615–32.
[296] Krauss TF. Why do we need slow light? Nat Photon. 2008;2:448–50.